Lipid membrane characterization with second harmonic scattering: surface potentials, ionization, membrane asymmetry and hydration

THÈSE N^O 7626 (2017)

PAR

Cornelis Ulrich LÜTGEBAUCKS

ÉCOLE POLYTECHNIQUE
FÉDÉRALE DE LAUSANNE

Suisse
2017

To my parents

Acknowledgements

Lausanne, 10 January 2017   Cornelis Lütgebaucks

Abstract

Membranes, composed of a variety of lipids and other biomolecules, mediate signaling processes between cells and their aqueous environment. To fulfill this function, membranes can vary their composition leaflet-specific and thus alter their surface properties. To fully understand the impact of these processes on the molecular level, it is necessary to develop tools that can access the molecular properties of free-floating model membranes label-free. These tools are ideally surface-specific. In this thesis, we apply the nonlinear optical techniques second harmonic scattering (SHS) and vibrational sum-frequency scattering (SFS) together with electrokinetic measurements to label-free characterize the interfacial properties, hydration structure and surface potentials of liposomes in aqueous solutions.

First, we generalize the nonlinear optical theory to describe the second-order surface response from interfaces with aqueous solutions independent of the ionic strength for reflection, transmission and scattering geometries. We demonstrate that interference effects from oriented water molecules in the bulk aqueous solution alter the probing depth and the expected second-order response at low ionic strengths.

Then, we apply this theory to demonstrate that SHS patterns of liposomes and oil droplets contain all necessary information to extract the absolute surface potential of the respective particles without assuming a model for the interfacial structure. By analyzing scattering patterns that capture the orientational distribution of water around the particles, we find surface potentials of -38 mV for bare oil-droplets and -11 mV for zwitterionic liposomes in water. For anionic liposomes the surface potential varies between -150 mV and -23 mV in solutions containing different amounts of NaCl ranging from ~0 mM to 10 mM. These values are remarkably different for solutions to the Gouy-Chapman model considering a fixed surface charge density.

Next, we characterize the hydration and lipid asymmetries in binary mixed membranes using SHS and SFS. The liposomes exhibit hydration asymmetry between the inner and outer leaflet. The lipid number density between the inner and outer leaflet is the same, although geometrical packing arguments would suggest a different density. However, an asymmetric lipid distribution between the leaflets can be induced by fine tuning specific intermolecular interactions between the lipids. This is shown with dipalmitoylphosphoserine and dioleoylphosphocholine mixtures creating a membrane

Acknowledgements

structure that allows intermolecular H-bonding between the phosphate and amine groups of the lipids.

Finally, we quantify the surface properties of membranes composed of lipids containing phosphoserine and phosphocholine headgroups. Surprisingly, we find a very high degree of counterion condensation on anionic membranes in pure water: only 1 % of all lipids are ionized. This indicates a tightly packed layer of ions around the membrane that needs to be considered when modelling the interfacial structure around membranes.

Zusammenfassung

Zellmembranen sind komplexe Strukturen, die die Zellkommunikation und Signaltransduktion zwischen Zellen und ihrer wässrigen Umgebung kontrollieren, indem sie ihre molekular Zusammensetzung verändern. Diese Veränderung führt gleichzeitig zu veränderten Oberflächeneigenschaften. Um diese Prozesse auf einer molekularen Ebene beschreiben und verstehen zu können ist es nötig, Methoden zu entwickeln, die solche Eigenschaften an Modellmembranen bestimmen können. Idealerweise sollten diese Methoden oberflächenspezifisch sein. In dieser Arbeit benutzen wir Lichtstreuungsmethoden basierend auf den nichtlinearen optischen Effekten der Frequenzverdopplung und Summenfrequenzerzeugung, um die Oberflächeneigenschaften von frei schwebenden Membranen in wässrigen Lösungen, und ohne Einsatz von chemischen Zusätzen, zu bestimmen. Mit diesen Methoden sowie elektrokinetischen Messungen bestimmen wir die Wasserstruktur, deren Restrukturierung und das elektrische Oberflächenpotential von Lipidvesikeln.

Zuerst erweitern wir die theoretischen Grundlagen mit denen nichtlineare optische Prozesse der zweiten Ordnung, die an Grenzflächen mit wässrigen Lösungen stattfinden können, beschrieben werden. Wir können diese Prozesse nun unabhängig von der Ionenstärke der wässrigen Lösung korrekt darstellen. Die Ausarbeitungen sind für Messungen in Reflektion, Transmission oder durch Lichtstreuung gültig. In Lösungen mit geringer Ionenkonzentration treten Interferenzen auf, welche die Oberflächensensibilität und dadurch auch die erwartete generierte Lichtintensität stark beinflussen. Dieses Phänomen tritt auf, da nicht nur Wassermoleküle an der Trennfläche Licht generieren, sondern auch die aus der Volumenphase.

Anschließend benutzen wir diese Kenntnisse, um das Oberflächenpotential der Lipidmembranen zu bestimmen. Die Streuungsmuster von frequenzverdoppeltem Licht beinhalten alle benötigten Informationen um absolute Oberflächenpotentiale der Vesikel zu extrahieren ohne Annahmen über die Struktur der Grenzfläche zu machen. Wir bestimmen Oberflächenpotentiale von -38 mV für Öltröpfchen und -11 mV für zwitterionische Lipidvesikeln in Wasser. Für anionische Lipidvesikel in verschieden konzentrierten Salzlösungen verändert sich das Potential von -150 mV in Wasser zu -23 mV in 10 mM NaCl. Diese Werte weichen erheblich von berechneten Lösungen ab, die auf dem Gouy-Chapman Model und einer konstanten Ladungsdichte basieren.

Acknowledgements

Im nächsten Kapitel benutzen wir Zweikomponentenmembranen um mögliche asymmetrische Verteilungen der Lipide und der Wassermoleküle zu bestimmen. Die Membranen weisen eine unterschiedliche Hydration zwischen den beiden Lipidschichten der Membran auf, allerdings ist die Anzahl an Lipiden in beiden Schichten vergleichbar groß. Indem man die intermolekularen Interaktionen zwischen den Lipiden beeinflusst, ist es jedoch möglich eine asymmetrische, lipidspezifische Verteilung in den beiden Schichten der Membran hervorzurufen. Wir zeigen dies in Membranen- bestehend aus Dipalmitoylphosphoserin und Dioleoylphosphocholin- bei denen die spezifische Packungsdichte dieser beiden Lipide zu Wasserstoffbrückenbindungen zwischen den Kopfgruppen führt.

Abschließend bestimmen wir die elektrostatischen Eigenschaften von Membranen, die Phosphoserin und Phosphocholin enthalten. Überraschenderweise scheinen diese Membranen lediglich zu 1 % ionisiert zu sein, obwohl die Lösung nur sehr geringe Ionenkonzentrationen enthält. Dies lässt auf eine hohe Konzentration an Gegenionen direkt an der Grenzfläche schließen.

Stichwörter: Membranen, Lipide, Oberflächenpotenziale, Ionenkondensation, Hydration, nichtlineare Optik, Lichtstreuung, weiche Materialien, flüssig-flüssig Grenfläche, elektrische Doppelschicht,

Contents

Contents

List of Figures

List of Tables

1 Introduction

Lipid membranes, formed by self-assembly, provide a place for chemicals to react and create a protected environment. As they appear in every living organism and organelle, they are thought to be a key element for the creation of life as we know it.[1] Complex biological organisms could evolve, because the early organisms were able to shield themselves from the hostile outer environment by lipid membranes.

1.1 Lipid membranes

Membranes separate functional compartments in cells, control the transport in and out of such compartments, and regulate interactions between cells/ organelles and their environment.[1] To achieve this functionality, the membrane interface consists of many different components: Different kinds of lipids, phospholipids and glycolipids, hydrophobic sterols, various proteins, ions, and carboxy groups. As a consequence, cell membranes are not homogenous mixtures. The various components are distributed and ordered as dictated by their surroundings, functions, or external influences. In 1972, Singer and Nicolson proposed for the structure of the cell membrane a fluid mosaic model to account for the diverse composition and required component's mobility (Fig. 1.1).[2] Although this model evolved over the years, the fundamental idea of a highly dynamic and adaptive fluid that responds to environmental influences and intermolecular interactions remains.[3,4]

Modifications of the membrane composition can have severe consequences. Various diseases, among them diabetes *mellitus*, Alzheimer's disease, sickle cell anemia or Duschene muscular dystrophy, are associated with membrane dysfunctions.[5,6] In diabetes, for example, a scrambled membrane composition has been detected to lead to distorted cell shapes.[7] This altered membrane composition is also associated with the inability to incorporate certain transmembrane protein channels into the cell membrane.[8,9] These transmembrane channels are associated with sugar transport, so that ultimately cells cannot control the sugar level in the cell. This shows that lipids in the membrane are not only responsible for the overall structure and roughness, but also ensure indirectly the functionality of the cell and organelles.
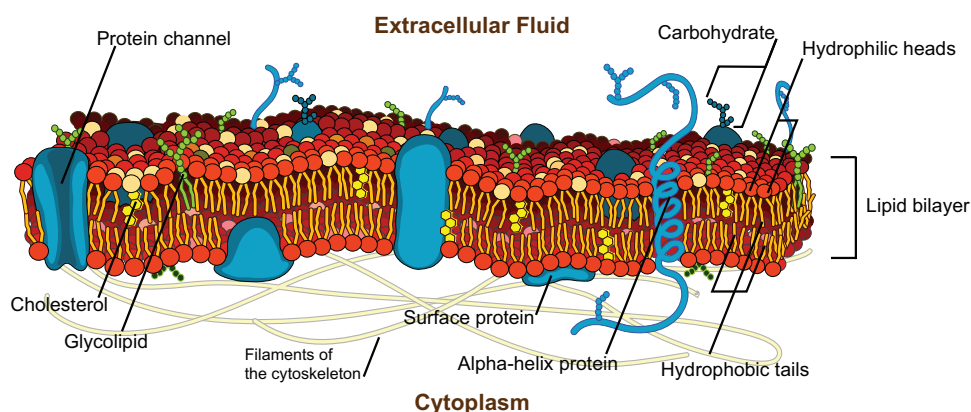
Figure 1.1: Fluid mosaic model of the plasma membrane. The model was introduced by Singer and Nicoloson in 1972 and shows a very diverse and interchangable composition of the membrane. Schematic modified from Ref. [10].

1.2 Lipids

Lipids are amphiphilic molecules, which means they are composed of both hydrophobic and hydrophilic structural components. When exposed to water the lipids spontaneously form (self- assemble into) a bilayer structure in which the hydrophobic fatty acids parts are shielded from the aqueous environment, whereas the hydrophilic part is fully exposed to and interacting with the water molecules. Lipids can be classified into three groups:[3] glycerol-based lipids, sterols, and ceramide-based lipids. Figure 1.2 shows the molecular structures of representative lipids of these three classes. For clarity, a single fatty acid chain structure is colored in red and the hydrophilic headgroups in blue. Glycerol-based lipids have two subgroups, the phospholipids and the glycosyl-glycerides. Typically, lipids have 1 or 2 hydrophobic fatty acid chains that are esterified together. In glycosyl-glycerides, these fatty acid chains are esterified to the glycerol backbone that is esterified to a sugar moiety. In phospholipids the glycerol links the fatty acid chains and is esterified via a phosphate group to a hydrophilic headgroup, which could also be a sugar moiety. Glycerophospholipids represent the majority of lipids in eukaryotic membranes. Ceramide-based lipids do not contain glycerol and are synthesized from a ceramide structure, which is an amino-alcohol bound to a fatty acid chain. Sterols are hydrophobic molecules, which are almost completely located inside the lipid bilayer and surrounded by fatty acid chains so that only the OH group may protrude into the aqueous phase.

In this thesis, we will exclusively discuss phospholipids. Phospholipids are often distinguished by their respective headgroups, which define several chemical and structural properties of the lipid, such as charge, solubility in aqueous phases, and packing in a membrane. Figure 1.3 shows typical lipid headgroup structures as used in this thesis, sorted according to their zwitterionic and anionic headgroups. The

Glycerophospholipid   Ceramide-based lipid   Sterols

DOPS   Sphingomyelin   Cholesterol
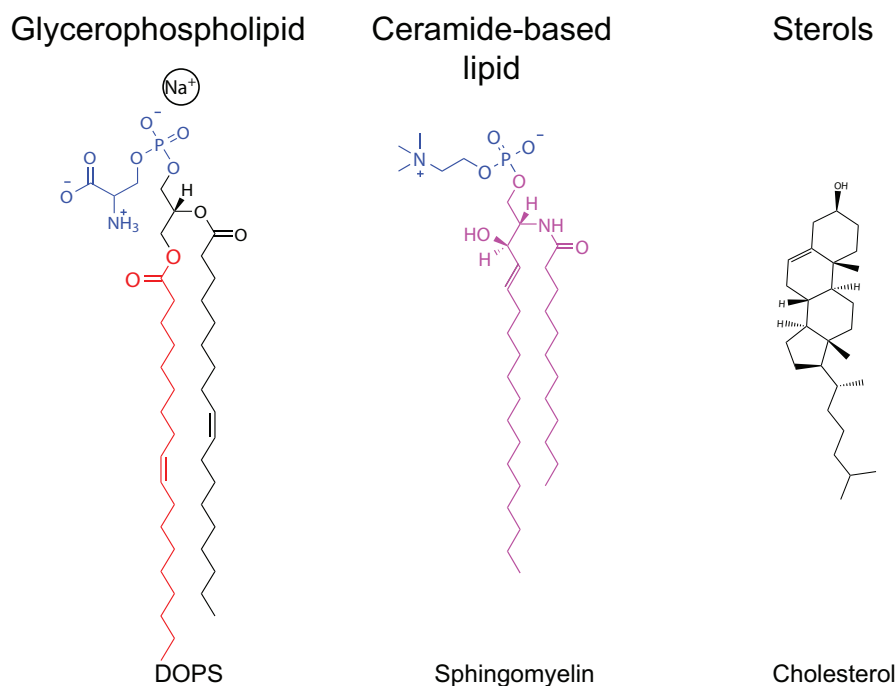
Figure 1.2: Lipid categories. Three representative lipids of the three categories: Glycerol-based lipids represent the major group of glycerophospholipids. Glycerophosphospholipids are synthesized from glycerol and have typically 1 or 2 fatty acids (single fatty acid, red) that are esterified to each other and then linked via the glycerol to the phosphate containing headgroup. Ceramide-based lipids contain a ceramide (purple), which is an esterified sphingosine and a fatty acid chain. Sterols are smaller lipids. Cholesterol is the most common one.

structure displays also the net charge when hydrated in water at pH 7. The structural properties of a lipid and the possible intermolecular interactions are, however, not solely defined by the headgroup, but also depend on the chemical composition of the fatty acids as we will see in chapter 5.

1.3 State of the art in membrane research

The importance of lipid membranes for biological functionality has generated a lot of research during the last century. Excellent reviews summarize the most important findings related to, for instance, lipid regulation of cell membranes,[11] the structure of different lipid bilayers,[12] or direct lipid-protein interactions.[13,14] The membrane composition affects intracellular signaling pathways,[15] as well as protein incorporation and their functionality.[16,17] It was also found that different material surfaces interact differently with membranes. For example, the often used implant material titania alters the dynamic movement of the membrane and also affect the position of specific lipids in the membrane leaflets.[18] More specifically, the direct interaction between lipid specific surface charges and ions, as well as a different hydration environment
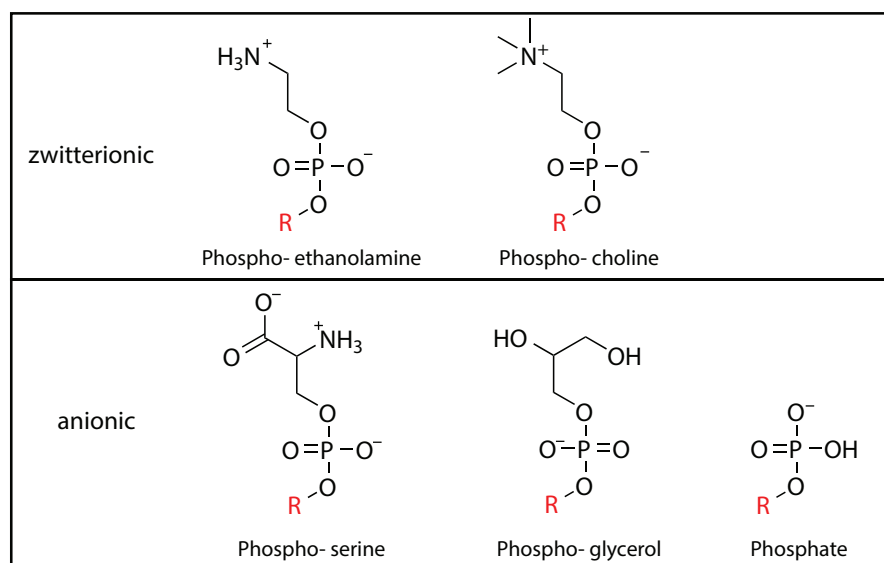
Figure 1.3: Lipid headgroup structures. Different lipid headgroups of phospholipids as used in this thesis. The structure show the charge distribution when immersed in pH neutral conditions. *R* indicates the rest of the lipid, namely the glycerol and fatty acids. The zwitterionic lipids are charge neutral, whereas the anionic lipids carry one negative charge. The different chemical structures result also in different packing geometries and different headgroup interactions.

can induce lipid membrane and transmembrane redistribution.[19] To study the relation between structure and function of a membrane, a variety of membrane model systems have been established. The choice of the system depends on the purpose of the study as we will discuss in the next section.

1.3.1 Membrane models

Figure 1.4 displays a variety of membrane model systems. Naturally occurring cell membranes of diverse organelles, bacteria, or entire eukaryotic cells are the most complex membranes (Fig. 1.4a). Maintaining the full cellular structure helps analyzing intracellular signaling pathways or specific compounds.[20] Often staining methods are used on these complex membranes to identify key components in the membrane. A downside is that such labels are artificial additives that can bias the mobility and location of the lipids. Such additives undoubtedly influence the molecular structure and distribution of the membrane/ hydration environment and thus are not useful for a molecular level study of lipid motion, orientation, hydration, and charge influences.

The other extreme as membrane model system from a structural point of view are lipid monolayers deposited on a water surface (Fig. 1.4b). Such monolayers are formed in a Langmuir trough, a device with an adjustable surface area. The advantage of such films are that one can easily access the monolayer, control the
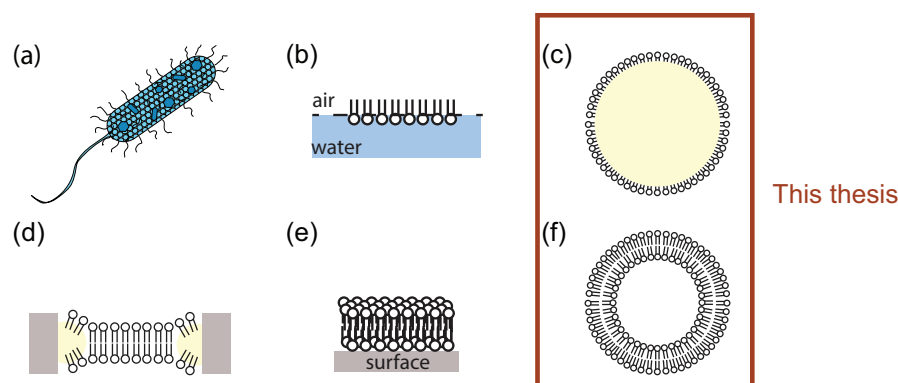
Figure 1.4: Diverse model membrane systems. The model membranes vary in complexity apparent in the number of different lipids and related impairments due to structural effects. (a) The most complex and most natural membranes exist in model organisms, i.e. bacteria or cell membranes of organelles. Synthetically assembled monolayers and bilayers can exist under different conditions and geometries. (b) Monolayers at the air/water interface are the least complex and most artificial models as they lack the bilayer structure and are in an artificial environment . These membranes enable molecular level studies. (c) Monlayers on oil droplets dispersed in water are a recently introduced model that mimics the lipid droplets in eukaryotic cells. (d) Freestanding black lipid membranes are difficult to form with gel-phase lipids, but are well hydrated and unperturbed in the center. Eventually oil may interfere with the bilayer structure. (e) Supported lipid bilayers (SLBs) are typically formed from vesicles rupturing on a support. The lipid position and dynamics are highly affected by the material surface on which they are formed. SLBs may have some defects not covering the entire surface, but are otherwise very stable systems to quantify structural parameters of a membrane.(f) Liposomes are unperturbed spherical bilayer shells that float in solution. The composition of liposomes is easily altered.

composition carefully, and have a good control over the lateral pressure and thus the packing density. Due to their simplicity, these monolayers have been used for decades to study phase transitions, packing densities, head group features and different compositions with a large variety of techniques.[21] The simplicity predestines these samples also very much for studying molecular level interactions with great detail. For example, vibrational sum-frequency generation (SFG) spectroscopy has been used to study the alkyl chain conformation[22–26], the effect of cholesterol on the alkyl chain conformation[27], the lipid head group structure and its hydration environment with molecular detail.[28,29] Although the Langmuir monolayers have many advantages, there are also a number of disadvantages. In typical setups, large sample volumes (150 ml) are required to establish an appropriate pressure dependent surface area of 20-60 cm^2.[30] As a consequence large amounts of biomolecules are needed. In addition, limitations on the available purity of biomolecules (off-the-shelf lipids, > 99 %; proteins ~ 95%) results in unavoidable concerns regarding cleanliness and reproducibility/reliability on molecular level studies. The presence of air as a contact

medium enables the easy accessibility of the monolayers to probes, but also results in an environment that is not very close to most membrane environments. At the same time unsaturated lipids and compounds (such as cholesterol) are easily oxidized.[31]

A model system that solves some of these issues, are lipid droplets (Fig. 1.4c). These are composed of nanometer sized oil droplets that are covered with a lipid monolayer and dispersed in an aqueous solution.[32] The surface to volume ratio is $\sim 10^3$ larger as that of a Langmuir trough, the sample volume is small ($\sim 50\,\mu l$), and as the monolayers are fully immersed in water, no oxidation takes place. In addition, lipid monolayers on oil-droplets occur in nature as trigylceride-lipid droplet. Using such a biomimetic assembly under their natural aqueous conditions, enables one also to obtain detailed information about their metabolic features.[33]

Many other membrane model systems contain a bilayer structure that enables the possibility to consider intermolecular interactions between the leaflets. The most widely used models are freestanding lipid bilayers, known as black lipid membranes (BLMs, d), planar supported lipid bilayers (SLBs, e), and liposomes (f). Freestanding lipid bilayers have been used for several decades and are used in conjunction with electrical resistance, and impedance measurements, as well as various forms of fluorescence microscopy.[34–36] Using those methods, lipid-protein interactions, membrane poration with ion channels,[37] and particle-membrane incorporation were studied.[38] As BLMs are just ~ 5 nm thin membranes sandwiched between two aqueous phases, they are fragile and difficult to access for molecular probes.

In this respect, SLBs deposited on various solid substrates are more ideal candidates to extract structural parameters of molecules. For instance, atomic force microscopy and neutron reflectometry have been used to map the thickness of a lipid bilayer with a nanometer resolution.[39,40] Electrostatic force microscopy was used to determine the dielectric constant of dipalmitoylphosphatidylcholine membranes on silica. The authors of this study report a dielectric constant of the bilayer of $\epsilon \sim 3$, and a polar headgroup dielectric constant of approximately $\epsilon_{polar} \sim 30$.[41] Conboy and co-workers used vibrational SFG to label-free characterize transmembrane kinetics in SLBs. They studied lipid flipflop of zwitterionic[42–44] membranes and membranes containing zwitterionic and anionic lipids in the gel-phase.[45] They found a lipid fliflop rate of $2.5 \times 10^5 s^{-1}$ at 5 °C using dimyristoylphosphocholine SLBs, which is remarkably faster than the ones found by Nakano *et al.* using liquid-phase liposomes and small-angle neutron scattering.[46,47] The origin of this discrepancy is still under discussion. SLBs have also been used to determine nanoparticle kinetics and absorption properties depending on their surface functionalization.[48] One drawback of SLBs is that, as the bilayer is formed on a supporting substrate, the substrate may affect the lipid positioning, interactions and hydration within the bilayer.[49] Although this feature of redistribution may be advantageous and result in an intrinsically asymmet-

ric distribution in the bilayer,[50] it alters the membrane structure compared to what could be found in an aqueous environment. Another issue with SLBs is the possibility of forming incomplete bilayers or bilayers with defects,[51] which may dramatically influence the redistribution of lipids.

Small unilamellar vesicles or liposomes (Fig. 1.4f) combine the advantages of various systems discussed so far: they have a very high surface to volume ratio, they are bilayer systems that are freely suspended in an aqueous phase, and they occur in eukaryotic cells. Furthermore, liposomes can be easily prepared and their stability can be easily checked.[52] For these reasons, we will mainly use liposomes in this thesis. Lipid droplets are also used, as a means to compare mono- to bilayers of comparable size and shape. We will obtain molecular level information about the hydration and intermolecular interactions, and use these findings to compute the surface potential and the degree of lipid ionization. Characterizing these parameters helps to further understand the molecular mechanism of lipid-lipid interactions, stability control and the role of the aqueous environment in synthetic membranes. These parameters are not only important for a fundamental understanding but can be useful in practical applications; for instance, constructing lipid drug delivery systems that have a better targeting mechanism when used in an organism.[53]

1.3.2 Hydration of membranes and electrostatic interactions

Membrane hydration is a critical factor for membrane stability.[54] It is, however, not often studied as this aspect of membrane structure is difficult to access. X-ray scattering and nuclear magnetic resonance (NMR) spectroscopy have been used on multilamellar bilayers composed of either dioleoylphosphatidylcholine (DOPC) or dioleoylphosphatidylserine (DOPS) and a varying hydration.[55] It was found that probing fully hydrated membranes, there are 11 water molecules strongly associated with the DOPS headgroup, whereas a second hydration shell contains 10 water molecules before an isotropic water distribution is established. Around DOPC headgroups less molecules are affected before an isotropic distribution is considered: 6 water molecules are tightly bound in the first shell, and 6 more in a second intermediate shell before the molecules are isotropically distributed.[55]

While the aqueous environment is the driving force to create a membrane in the first place, lipid membrane stability also critically depends on electrostatic intramembrane interactions.[3] Electrostatic interactions between lipids in membranes, ions and water molecules in the adjacent aqueous phase affect packing, thickness and molecular mobility of the lipids. These interactions are also connected to the control of transmembrane transport via the local accumulation of charged species to create certain catalytic sites at the cell interface.[56] Hence, the hydration and electrostatic properties of membranes are not separable. The electrostatic properties of

membranes have been studied extensively using only theoretical approaches[57–59], but experimentally there are only a few applicable techniques and most of them require planar bilayers. Using frequency dependent conductivity measurements, Schwan *et. al.* determined the capacitance of phospholipid membranes to be around 12 $\mu F/cm^2$.[60] Atomic force microscopy and certain derivatives of this method, i.e. electrostatic force microscopy,[41,61] can be applied to obtain information about the dipole potential of lipids in supported lipid bilayers.[62] Recently Klausen *et al.* proposed a sophisticated surface conductivity microscopy technique to measure charge densities of surfaces in high ionic strength solutions,[63] but also this technique requires planar interfaces. Fluorescent binding assays that can be used to characterize the surface charge density were shown to determine the surface charge density on thin films.[64] In order to access the electrostatic properties of BLMs, one uses typically capacitance or inner field compensation methods.[65] For non-planar, non-supported membranes, however, these techniques are not applicable and we will not go into more detail, here. For liposomes, electrokinetic measurements are the only possibility (as we will describe in chapter 2). With electrokinetic measurements, different electric properties can be obtained, such as the ζ-potential and an electrokinetic charge density.[66,67] The ζ-potential determination has been the most common experimental method to qualitatively characterize electrostatic properties. To these properties belong the point-of-zero charge for a material, or the surface charge, which is only extrapolated from the measurement in conjunction with mean field models of the interfacial structure. These properties relate to e.g. dispersion stabilities, but the measurements do not provide direct molecular level interfacial information (see section 2.2.4). In order to obtain values for the surface potential and charge distribution, one needs to apply several assumptions about the interfacial structure and electrostatic interactions. Recently, Poyton *et al.* applied electrokinetic measurements on SLBs with fluorescent labeling to highlight the challenges with the assumptions of this method.[68] As we will see in chapters 4 and 6, the choice of the assumptions may result in very different solutions.

One possibility to access the molecular level structure of liposome membranes directly is to use the nonlinear optical techniques, second harmonic scattering (SHS) and vibrational sum-frequency scattering (SFS). These techniques combine light scattering techniques with the nonlinear optical phenomena of second harmonic generation (SHG) and vibrational sum-frequency generation (SFG). Some background information about those methods is provided in the next section, in which we put a particular focus on SHG as this is the main method of choice for this thesis. Note,though, that when we mention SFG, we refer typically to vibrational SFG unless stated otherwise.

1.4 Second harmonic and sum-frequency generation

1.4.1 Nonlinear processes

SHG was discovered in 1961,[69] and has been used in various imaging and scattering experiments since then, see for instance Refs. [45, 70–76]. Over the last decades SHG and SFG attracted attention for membrane research because of their intrinsic surface sensitivity. The surface sensitivity originates from the selection rules of the underlying second-order optical processes.[77–79] When electromagnetic fields interact with a medium, they can induce a molecular dipole $\mathbf{p}$ in molecule i. This dipole can be expressed as[80,81]

$$\mathbf{p}_i = \alpha^{(1)} \cdot \mathbf{E} + \frac{1}{2}\beta^{(2)} : \mathbf{EE} + \frac{1}{6}\beta^{(3)}\mathbf{EEE} + \dots$$

Here, α is the polarizability, $\beta^{(2)}$ the second-order polarizability (or first-order hyperpolarizability), and $\beta^{(3)}$ the third-order polarizability. Each term can describe a charge oscillation in the molecule depending on the strengths of the interacting fields. The polarization $\mathbf{P}$ of the medium is a sum of the induced molecular dipoles per unit volume. As we will see in detail in chapter 3, the second harmonic (SH) light originates from the the second-order polarization $\mathbf{P}^{(2)}$ that is proportional to the second-order induced molecular dipoles according to

$$\mathbf{P}^{(2)} = \epsilon_0 \chi^{(2)} : \mathbf{EE} = N\langle \mathbf{p}^{(2)} \rangle$$

$\langle \mathbf{p}^{(2)} \rangle$ represents the orientational average of the second-order induced dipoles. $\chi^{(2)}$ is the second-order susceptibility, which describes the local second-order optical response of the medium. In the electric dipole approximation,[82] both SHG and SFG are forbidden in centrosymmetric media based on symmetry requirements, which results in surface-sensitivity.

Figure 1.5 shows different geometries of SHG and SFG measurements. The most common geometries for SHG and SFG experiments are planar reflection experiments (panel a and panel b). More recently SHG and SFG were performed in a scattering geometry (panels c and d) to obtain molecular level information of nanoscopic objects in solution. For SFS typically two incoming light beams of different frequencies are focused into a particle dispersion in an liquid[83] or solid[24] phase. For SHG experiments, mostly a single illuminating beam is used (panels b and d).

The optical interactions for SHG (SFG) can be either resonant or nonresonant. For a resonant interaction the photon energy of either the incident or the sum-frequency coincides with the energy difference between two molecular states. A nonresonant interaction occurs, when the photon energy of all beams is different from the energy level differences of the molecule. Resonant excitation results in chem-
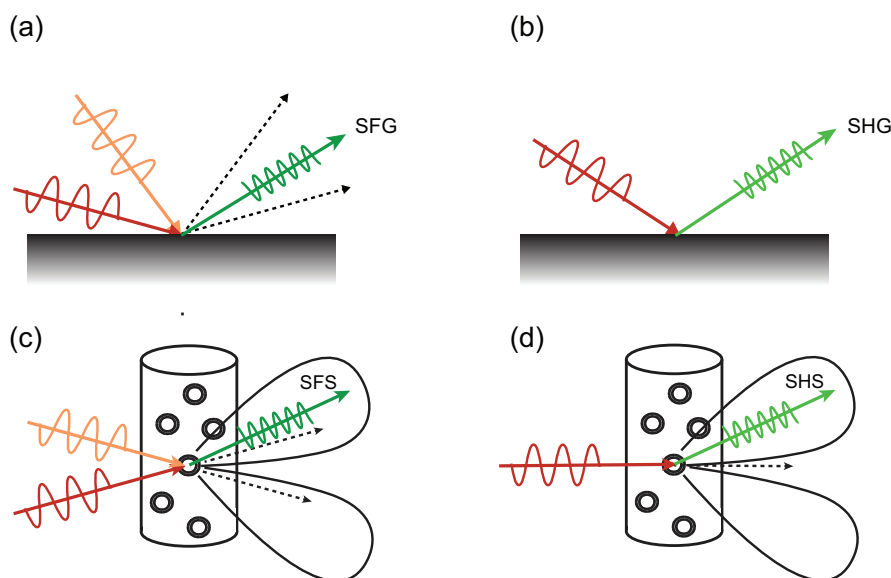
Figure 1.5: Illustration of various beam geometries for SHG and SFG. The nonlinear techniques sum frequency generation and second harmonic generation can be used in different measurement geometries: (a) sum-frequency planar reflection geometry, (b) collinear second harmonic reflection geometry, (c) sum-frequency scattering, (d) second harmonic scattering

ical sensitivity.[84–90] Figure 1.6 illustrates the resonant and nonresonant processes. In order to use the chemical specificity of SFG, one needs to fine tune the frequency of one of the beams to the infrared so that the photon energy is resonant with the eigenfrequency of the respective vibrational mode of the desired molecular group. This first-order infrared polarization is upconverted by a second nonresonant photon with a frequency in the visible range to a virtual state (indicated by the dashed line in Fig. 1.6a)). This second-order polarization, which is essentially a charge oscillation, will emit a photon at the sum-frequency of the infrared and visible photon returning the system to the ground state.

In resonant SHG, the sum of the two incoming photon energies is resonant with an electronic transition in a molecule as illustrated in Fig. 1.6b. By probing molecules at interfaces that have electronic states close to resonance with the SH frequency, one can obtain an enhanced SH intensity from the interface. For example, Doughty *et al.* used the resonant transition of Daunomycin to probe the binding kinetics of this anti-cancer drug to DNA that was tethered to particles.[91] In nonresonant SHG neither the incoming photons nor the second harmonic photon are at resonance with any molecular transition. Nonresonant femtosecond SHS is a form of coherent elastic light scattering. The response of each molecule is identical and the SH intensity scales quadratically with the number density. Using the harmonic oscillator model under nonresonant conditions, it can be shown that the second-order susceptibility

takes the form[92]

$$\chi^{(2)} = \frac{e^3}{\epsilon_0 m^2 \omega_0^4 d^4}$$

with e the fundamental charge, ϵ_0 the permittivity of free space, m the mass of the oscillating electron, ω_0 the frequency of the electromagnetic field, and d the lattice distance between atoms. That means, the second-order polarization scales with the electron density (e/d^3) in the sample, which is not very specific to a particular molecule. The molecular selectivity might come, however, from the fact that only non-centrosymmetric molecules can generate an SHG photon (e.g. water but not Na^+) and the number density difference. Thus, in aqueous solutions, one probes primarily interfacial water molecules as even at the interface the density of water greatly outnumbers the density of solutes or surface groups.[93–95] This is an essential feature that enables one to probe interfacial hydration as demonstrated repeatedly at planar interfaces.[96]
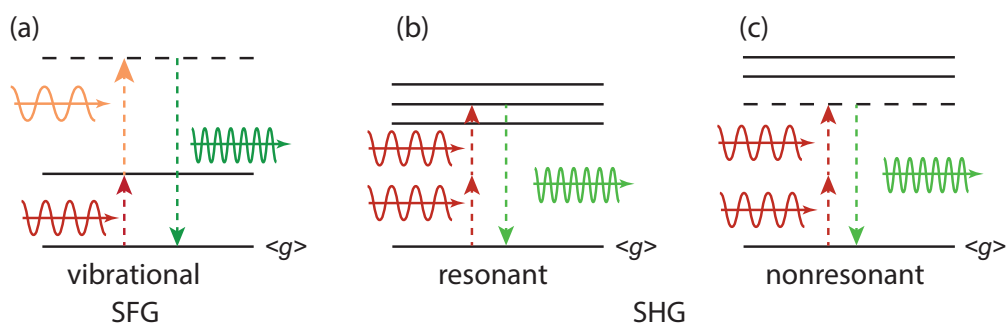
Figure 1.6: Schematic of energy conversion in vibrational SFG and SHG processes. (a) In a vibrational SFG process the infrared photon is resonant with the transition energy of a vibrational mode. The visible photon lifts the energy level to a virtual state. Upon relaxation back to the ground state (<g>) this leads to an emission of a photon at the combined frequency of the two incoming photons. (b) In resonant SHG the sum of the energy of two incoming photons with the same frequency are resonant with an electronic transition leading to the instantaneous emission of a new photon with the SH frequency. (c) In nonresonant SHG two photons with the same frequency excite the molecule to a virtual state leading to the emission of a photon of twice the frequency of the incoming ones.

1.5 Conceptual illustration of SHS from a sphere

Wang *et al.* provided the first proof of second harmonic scattering from dielectric particles in 1996.[97] We illustrate here briefly the underlying concept of SHS from a sphere following Ref. [98], before going into more detail of subsequent experimental studies with a particular emphasis on membrane related findings using SHS. A detailed mathematical description of SFS and SHS from spherical scatterers can be found, for
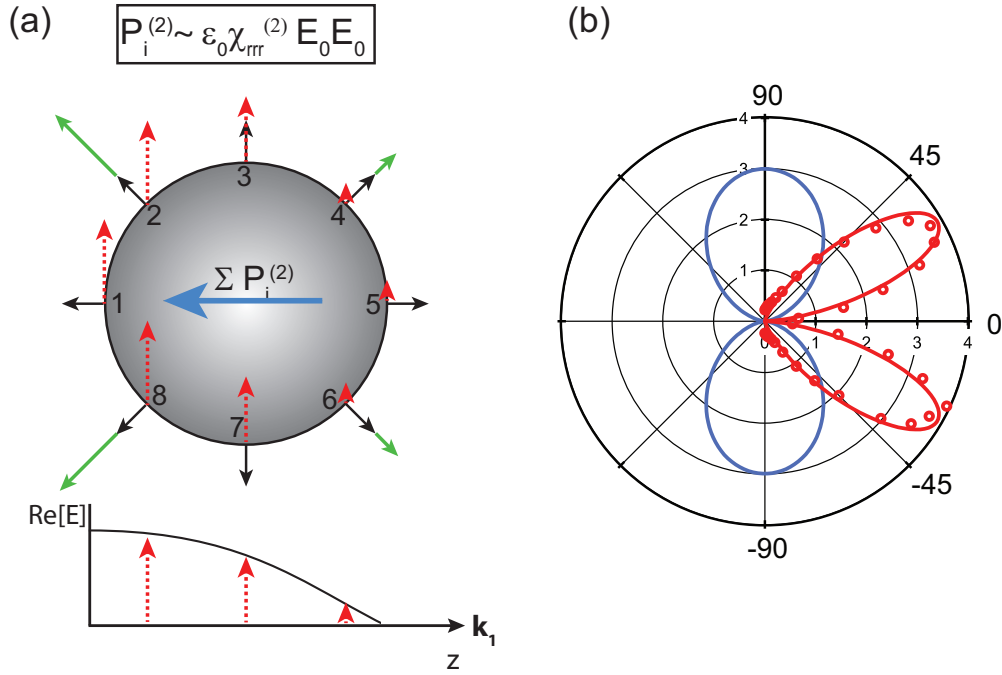
Figure 1.7: Second harmonic scattering from a sphere. (a) Schematic of the effect of relative size on nonlinear light scattering. A single beam impinges (z-direction) on a particle that has a surface susceptibility $\chi^{(2)}_{rrr} \neq 0$ indicated by black radial directed arrows. While propagating through the particle the phase of the incoming beam changes at different positions of the particle leading to different magnitudes of induced local polarizations (green arrows). The effective particle polarization is the sum of all induced polarization components resulting in a net longitudinal dipole along beam propagation.(b) Blue: simulated radiation pattern of the longitudinal dipole as drawn in (a). Red: Typical SHS pattern as observed in the far-field of 500 nm polystyrene beads solution in water with fit considering geometrical interfernce effects.

example, in Refs. [99–102] and is given in chapter 3.

If the size of the particle is much smaller than the wavelength of the fundamental beam (in our case R<10 nm), the system is effectively centrosymmetric and the selection rules of SHG/SFG predict that the resulting induced dipoles will add up to a vanishing net second-order dipole. When the dimension of the particle becomes larger, however, the second-order induced molecular dipoles at the particle surface will experience different phases and therefore lead to a non-vanishing net second-order dipole. This can be understood in a simplified situation considering a spherical particle with a single susceptibility element that is illuminated with a single beam similar to Fig. 1.5d. Figure 1.7a shows such a sphere highlighting only eight different surface positions. The incoming field is represented as a plane wave with $E = E_0 e^{i\mathbf{k}\cdot\mathbf{r}}$. The eight black arrows indicate a non-zero surface susceptibility element in the radial direction, which has the same magnitude independent of the position at the surface. This susceptibility represents the local surface response. When the

fundamental light travels through the particle, the magnitude of the interacting E-field (red arrows) changes because of a phase change. This results in different magnitudes of the induced surface polarization components (green arrows) on different points of the surface. To determine the resulting total second-order response of the particle the surface polarization components need to be summed up over the entire surface. The polarizations without a z-component (1,3,5,7) do not contribute to the net signal, but the others (2,4,6,8) do. Due to the optical phase difference, the sum of the dipoles will be a net polarization of the particle along the z-direction (arrow in blue (panel a) and simulated pattern in blue (panel b) in Fig. 1.7). The characteristic SHS pattern, however, is more complex. For describing the SHS patterns in the far field, the geometry of the scatterer and the interaction of the optical fields need to be considered.[102] We will see in chapter 3 that this relationship can be expressed by an effective susceptibility $\mathbf{\Gamma}^{(2)}\left(\boldsymbol{\chi}^{(2)},\theta,R\right)$, with θ being the scattering angle, and R the particle radius. Figure1.7b shows a typical SHS pattern (in red) of a colloidal suspension of polystyrene particles (d= 500 nm) in water as observed in the far-field.

1.6 State of the art in nonlinear optical scattering of membranes

In the first SHS study in 1996, the scattering originated from polystyrene beads covered by malachite green (MG), which was needed to amplify the surface SH intensity. In 1998 and 2001, the Eisenthal group reported the generation of SH light from polystyrene particles and anionic liposomes, respectively. In both studies, carried out label-free, the SH response originated from oriented water molecules at the surface.[103,104] In this liposome study, Liu *et al.* proposed a method to obtain the surface potential of membranes using fixed single angle SHS experiments in combination with the Gouy-Chapman theory.[104] We will refer to this study more in detail in chapter 3. In 2003, the first angle-resolved SFS experiments were reported using solid silica particles that were covered with alkane chains.[24] It required several years to report the first label-free SFS of surfactant vesicles in water.[105] The two surfactants, sodiumdodecylsulfate and dodecyltrimethylammonium bromide distribute themselves asymmetrically when forming the leaflets. The first label-free and angle-resolved SH study was reported by Schürer *et al.* in 2010 in which the surface of polystyrene beads in water was probed.[106]

Since the first demonstration of nonresonant SHS from liposomes in water, several studies followed, characterizing lipid membrane and membrane transport using mostly resonant SHS. The Eisenthal group, for instance, studied the molecular transport through anionic membranes.[104,107] In particular, the diffusion of MG through the membrane was studied comparing DOPG vesicles in the liquid phase

with DPPG vesicles in the gel-phase.[108] The rigidity of the membrane was found to inhibit diffusion of MG. Further experiments showed that mixing cholesterol with DOPG in equal parts slowed the diffusion by a factor of six.[109] Moreover, the transport rate of MG molecules depends on the concentration of electrolytes in solution.[110] Liu *et al.* studied the efficiency of the transport rate of MG with the help of three different antibiotic ionophores, valinomycin, cyanide-*m*-chlorophenylhydrazone (CCCP), and gramicidin A, in real-time.[111] CCCP was ineffective in transporting ions through anionic membranes, whereas valinomycin and gramicidin transport kinetics were balanced by the concentration gradient of cations across the bilayer. Recently, Rao *et al.* determined the binding constants of HIV related TAT proteins to zwitterionic and anionic liposomes with nonresonant SHS.[112] They found binding constants of 7.5 ± 2 μM and 29 ± 4 μM for the zwitterionic and anionic liposomes, respectively.

A full systematic characterization of the intermolecular lipid interactions in free-floating unbiased lipid membranes and their effect on the hydration structure is still not available. We aim to close this gap by using polarization- and angle-resolved label-free SHS and electrophoretic measurements on liposomes that allow for the characterization of different lipid membranes, their electrostatic interactions and the resulting effect on the water structure.

1.7 This thesis

In this thesis, we apply nonresonant SHS to study membrane hydration and intermolecular interactions. This work is meant to be a milestone on the way to extend the use of SHS towards probing biological interfaces and to describe kinetics of proteins label-free. We access the orientational distribution of water around membranes with SHS and use this to determine the surface potential, ionization of membranes, and lipid distributions. The thesis is structured as follows:

- Chapter 2 contains the description and characterization of the optical setup, the methodology and applied assumptions, a description of complementary used techniques and of the sample preparation.

- In chapter 3, we extend the nonlinear optical theory so that we are able to describe SHG and SFG experiments from any kind of interface (planar and curved) in dilute salt concentrations based on the Rayleigh-Gans-Debye approximation.

- In chapter 4, we apply this theory to fully describe scattering patterns from lipid bilayers of different lipid compositions under conditions of varying ionic strength. We extract the potential for zwitterionic liposomes and quantify the change in the potential of anionic lipid membranes in different ionic strength. The results are compared to the Gouy-Chapman and the constant-capacitor model.

- In chapter 5, we quantify the hydration and lipid distribution of membranes composed of various binary mixtures of phospholipids. We also propose a mechanism based on H-bonding between neighboring headgroups to explain the observed lipid-specific leaflet asymmetry.

- In Chapter 6, we discuss the degree of ionization of anionic lipid membranes as a function of their composition and describe the impact of counterion condensation.

- Chapter 7 contains a summary of the findings and provides an outlook of future applications using SHS.

Various publications are the backbone of this thesis. A detailed list is given at the end of the thesis.

2 Experimental Details & Methodology

This chapter deals with the experimental details and methodologies applied throughout the thesis. It contains three sections. In the first section, we discuss the optical setup and choice of optics as well as the applied assumptions. In the second section, we describe the complementary techniques and relevant algorithms and normalization schemes. In the last section, we describe the sample preparation and characterization.

2.1 SHS: Characterization & Assumptions
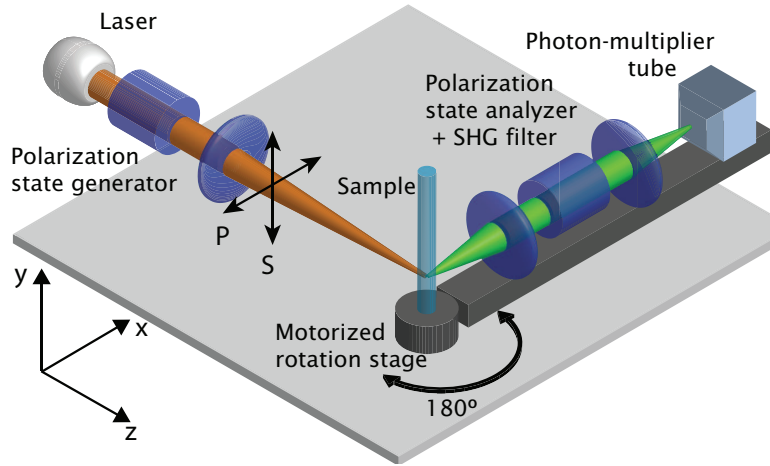
Figure 2.1: Schematic of the high efficiency angle-resolved SHS setup. The polarization can be chosen for the incoming and scattered light. Samples are contained in a cylindrical glass cuvette. Scattering patterns can be recorded over 180°.

2.1.1 SHS setup

The second harmonic scattering setup was built as a high efficiency setup for low contrast samples such as soft matter samples in aqueous dispersions. The inital setup was reported in Ref. [113], and has been altered subsequently to improve the scattering efficiency. Figure 2.1 shows a sketch of the core of the scattering setup. The horizontally polarized fundamental beam was generated by a mode-locked Yb:KGW laser (Pharos-SP system, Light Conversion) that produces 1030 nm ±5 nm femtosecond pulses with an adjustable repetition rate. In this work, the repetition rate was set to 200kHz. The polarization state of the fundamental beam was controlled by a Glan-Taylor polarizer (GT10-B, Thorlabs) and a zero-order half wave plate (WPH05M-1030) to be either horizontal (P, along x-axis in Fig. 2.1) or vertical (S, along y-axis in Fig. 2.1). Prior to focusing the fundamental beam, a long pass filter (FEL0750, Thorlabs) filtered out other frequencies. The fundamental laser beam was focused into a cylindrical glass sample cell (4.2 mm inner diameter, high precision cylindrical glass cuvettes, LS instruments) by a plano-convex lens (f = 7.5 cm). The beam waist was $2w_0 \sim 36$ μm; the corresponding Rayleigh length was ~ 0.94 mm. The scattered SH light was collected and collimated with a plano-convex lens (f = 5 cm), and polarization analyzed using another Glan Taylor polarizer (GT10-A, Thorlabs). The collimated light was then filtered (ET525/50, Chroma) and focused into a gated photomultiplier tube (PMT, H7421-40, Hamamatsu). The gate width of the PMT was 10 ns. The detected signal was subsequently amplified by a GHz wide band amplifier (HFAC-26dB, Becker

& Hickl) and finally read out by a two channel photon counter (SR400, Stanford research systems). The angular acceptance of light was determined by an aperture positioned just behind the collecting lens. Scattering patterns could be obtained over a range of $\Delta\theta = 180°$ using a custom-designed sample holder (Quantangle10, Quantum Northwest). The here described setup is shot-noise limited.

2.1.2 Characterization of the fundamental laser beam
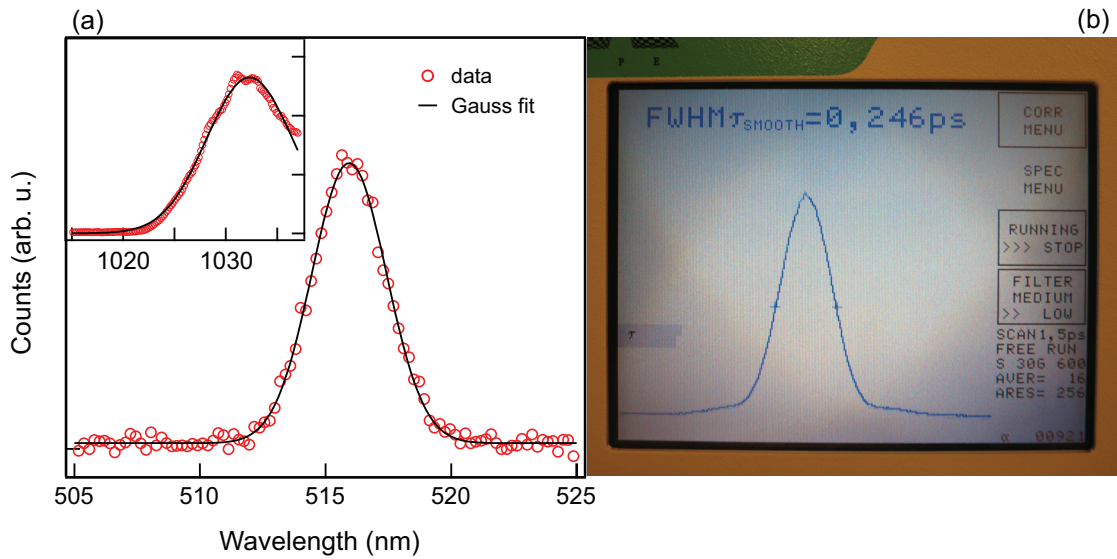
Figure 2.2: Temporal and spectral laser beam characterization. (a) SH spectrum of the fundamental laser beam after transmission through a BBO crystal. The inset shows the spectrum of the fundamental beam. The spectral resolution is 0.2 nm. The solid lines are fits with a Gaussian function. (b) Temporal profile of a laser pulse as measured with an autocorrelator.

In order to confirm the proper functioning of the setup, we characterized the laser system prior to doing experiments. Figure 2.2a shows the spectrum of the laser pulses after frequency doubling with a β-barium borate (BBO) crystal recorded with an USB spectrometer (USB4000, Ocean Optics). The red circles represent the measured data points, whereas the solid line is a fit with a Gaussian function. The spectrum shows a single peak centered at 516 nm wavelength, which indicates a fundamental wavelength of 1032 nm. The inset shows the spectrum of the fundamental beam. It peaks at 1032.3 nm with a FWHM of 9.8 nm, which corresponds in the frequency domain to 2.76×10^{12} Hz. We cannot obtain the full spectrum of the fundamental beam, because the detection range of this USB spectrometer is between 345-1037 nm.

To determine the temporal profile of a pulse, we measured the fs-pules with an autocorrelator (PulseChek, A.P.E). Figure 2.2b shows a photo from the measurement. The pulse duration (FWHM) from the autocorrelator is 246 fs corresponding to an

actual duration of 174 fs ($246/\sqrt{2}$). To rate the pulse quality, we also determined the time-bandwidth-product. For Gaussian shaped pulses generated from mode-locked lasers the minimum value is ~0.44.[114] The time-bandwidth-product of this laser setup is 174 fs × 2.76 × 10^{12} Hz = 0.48 implying a good quality of beam.
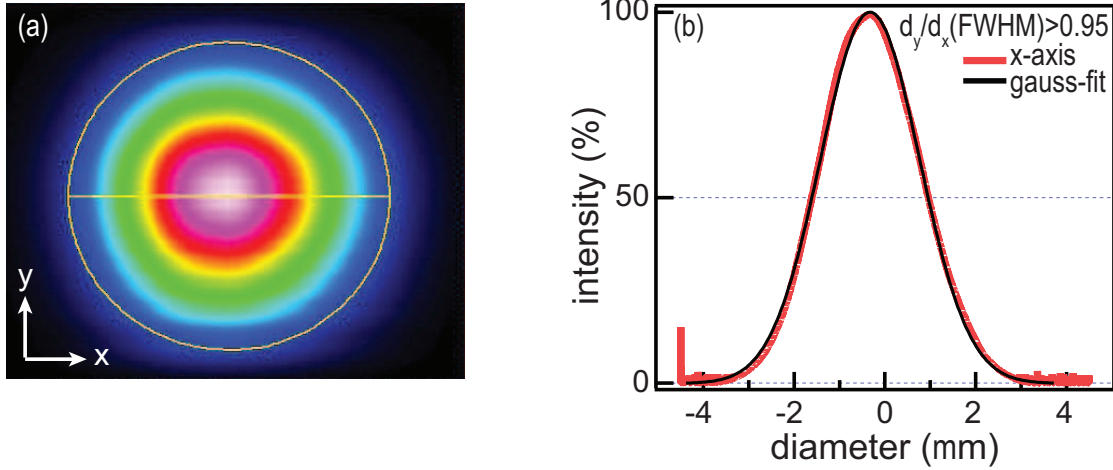
Figure 2.3: Beam profile of the fundamental laser beam. (a) 2D schematic of the fundamental beam profile. The yellow circle indicates the intensity decay to 1/e. The line through the center of the beam indicates the direction of the intensity cross section as plotted in (b). (b) Cross section of the 2D-intensity profile in (a) (red) with a Gaussian fit (black).

In the next step, we quantified the degree of ellipticity of the fundamental beam. A large discrepancy from a spherical Gaussian beam would lead to distorted asymmetric scattering patterns. Figure 2.3a shows a 2D representation of the collimated fundamental beam measured at 200kHz repetition rate and 15 mW average power. The yellow circle indicates the intensity drop to $1/e^2$ (13.5 % of the total intensity). The yellow center line is the x-axis along which we extracted the cross section of the beam, displayed in Fig. 2.3b. The recorded intensity cross section (red line) has a Gaussian shape (black line) as expected. The recorded FWHM is 2.55 mm. The cross section along the y-axis is almost the same. The ratio to determine the ellipticity is $d_{y\text{-axis}}$/ $d_{x\text{-axis}}$ > 0.95. These values are in agreement with the manufacture's specifications. Using the focusing lens of the SH scattering setup does not significantly alter the beam shape which confirms a good quality of the optical elements.

2.1.3 Validation of elastic SHG

For the generation of SH light, high photon densities are required. Depending on the pulse energy and the repetition rate of the illuminating light pulses, also other nonlinear optical effects that affect the water ordering or sample heating can occur. Hence, to guarantee solely an elastic SH repsonse, it is crucial to characterize the influence of the irradiation power on the detected intensity. The second-order response
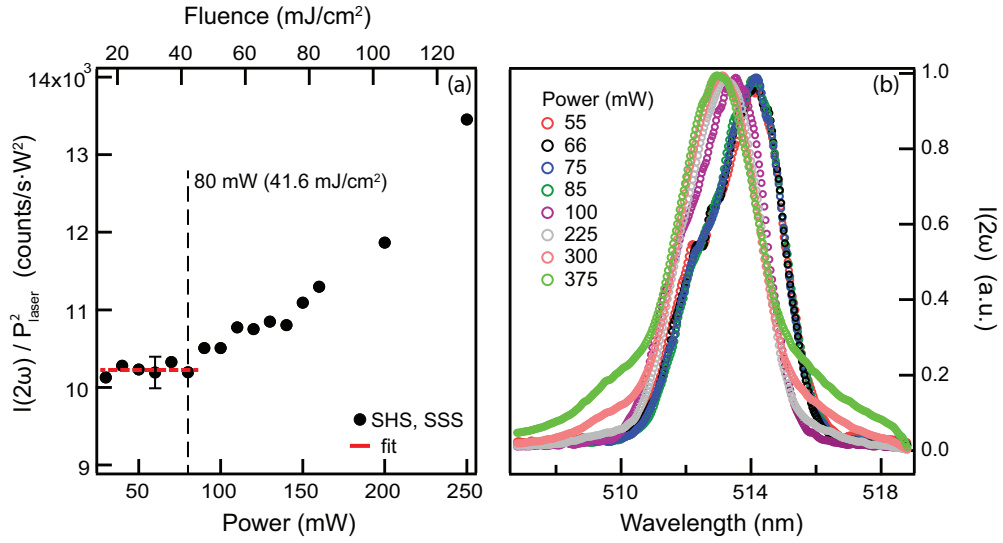
Figure 2.4: Elastic SHS of water. (a) SH intensity measured at 90° and divided by the square of the incident average power as a function of incident average power (bottom axis) and fluence (top axis). The red lines highlights the range in which there is a quadratic dependence of the SH intensity on the incident average power. (b) Normalized spectra of water at different incident powers at 90°. Courtesy of Y. Chen and C. Macias.

depends quadratically on the power of the irradiating beam. Figure 2.4a shows the power normalized SH response at a scattering angle $\theta = 90°$ in the SSS polarization combination as a function of power for a water sample. The letter assignment indicating the polarization combination is ordered according to the frequency. The first letter represents the polarization state of the detected SH light, whereas the following two letters describe the incoming beam polarization state. Up to 80 mW the SH intensity scales quadratically with the power as it is supposed to be for elastic SHG (red dashed line).[92] At higher power, the intensity deviates from this behavior indicating additional processes. This also becomes apparent in the blue shift and broadening of the water spectra (Fig. 2.4b). To avoid any additional effects, we used 60 mW incident power for all sample measurements.

2.1.4 Polarization sensitivity of the setup

In order to obtain reliable polarization-resolved measurements, we quantified the detection sensitivity of the setup for horizontally (P) and vertically (S) polarized light. According to the manufacturer, the detection sensitivity of the PMT varies between P and S polarization by maximum 5 % using a beam with 500 nm wavelength and normal incidence.[115] However, the optical components in the setup may affect this polarization sensitivity. To quantify the polarization sensitivity of the setup, we measured the two-photon fluorescence of 40 µM Trypan blue in water. The emission of
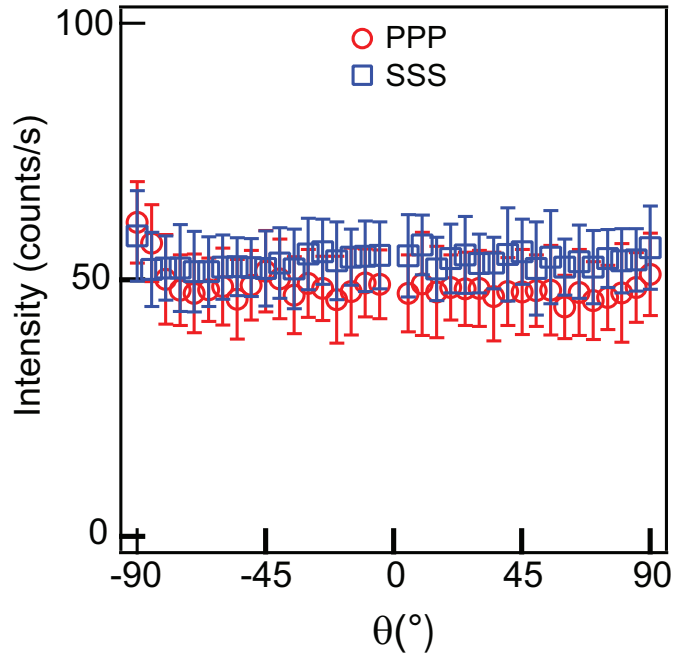
Figure 2.5: Polarization sensitivity of the setup. Scattering of isotropic two-photon fluorescent light from trypan blue in the PPP and SSS polarization combinations. 0° represents the forward propagation direction of the fundamental laser beam.

two-photon fluorescence is isotropic. Hence, for a polarization insensitive setup, we would expect an emission at even magnitude for all scattering angles and independent of the light polarization. Figure 2.5 shows the isotropic response obtained in the PPP and SSS polarization combination and confirms that this is indeed the case. The difference between the two polarization is slightly bigger than the prediction of the manufacturer but still within the standard deviation of 20 measurements (< 8%).

2.1.5 Characterization of the setup alignment

Liquids are typically considered to be isotropic (see next section for details), which means there should not be a coherent SH signal. However, there is an incoherent background signal that originates from tiny fluctuations in the orientation of the molecules. This scattering phenomenon is usually referred to as Hyper-Rayleigh scattering(HRS).[116] We use this HRS signal to determine the proper configuration and alignment of the setup. Figure 2.6 displays the raw scattering pattern of water in the PPP and PSS polarization combination, recorded with an angle of acceptance of 3.4° from -90 to 90° in steps of 5°. The scattering patterns are symmetric around 0°. The peak in intensity at 0° originates from SH light that is produced in the optical components of the detection arm and is usually excluded from further analysis. The scattering pattern recorded in the PPP polarization combination should have
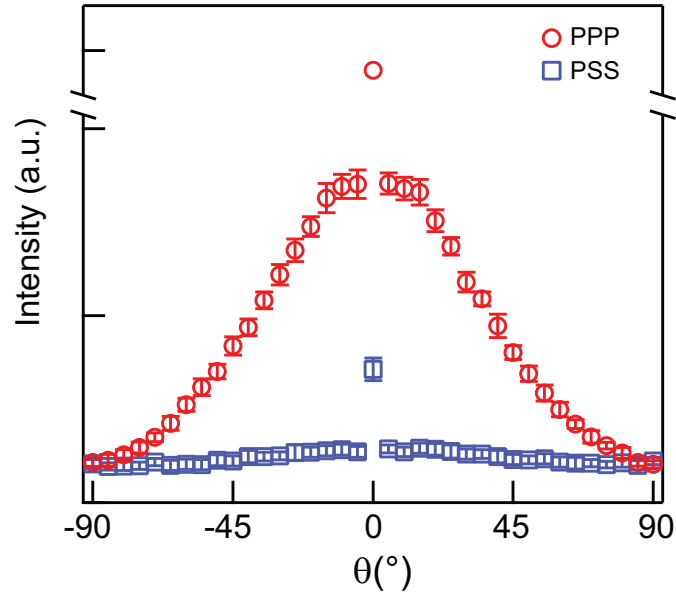
Figure 2.6: Scattering patterns of water in the PPP and PSS polarization combinations. 0° corresponds to the forward propagation direction of the fundamental beam. The patterns were recorded in steps of 5° with an angle of acceptance of 3.4°. Error bars represent the standard deviation from 20 measurements per angle.

a minimum at ±90°,[117] which is indeed the case. The pattern obtained in the PSS polarization combination follows the theoretical prediction as well. Schürer *et al.* were the first to publish nonresonant angle-resolved scattering patterns of water in the PPP and PSS polarization combinations.[118] The displayed pattern agree with the literature. The matching intensities obtained in PPP and PSS at ±90°, also obey the theoretical predictions,[117] and further validate the proper polarization sensitivity of the setup. We recorded the water pattern in the PPP polarization combination before every sample measurement to validate the alignment.

2.1.6 Normalization of the surface second harmonic (SH) data

As there is a background signal from the liquid, we need to correct the recorded SH intensity to obtain the surface related SH response of the samples. To do this, we first correct for the incoherent response of the bulk in the respective polarization combination. Second, we correct for angular differences of the focal volume and different measurement conditions by dividing the surface SH intensity by the SH intensity (HRS) of bulk water measured in the SSS polarization combination. This allows us to compare different data sets and to set an absolute scale. The normalization

can be summarized to

$$S_{Pii}(\theta) = \frac{I_{Pii}(\theta) - I_{s,Pii}(\theta)}{I_{W,SSS}(\theta)} \tag{2.1}$$

in which $I_{s,Pii}(\theta)$ is the HRS intensity of the solution without particles in the same polarization combination. $I_{W,SSS}(\theta)$ is the HRS intensity of uncorrelated isotropic bulk water measured in the SSS polarization combination, following the relationship by Bersohn *et al.*.[117] i represents a placeholder for the polarization direction (P or S, compare Fig. 2.1) The intensity of the scattered light in the SSS polarization combination is supposed to be constant over all scattering angles. Figure 2.7 shows a typical pattern for water in the SSS polarization combination and the standard deviation from 20 measurements. The solid line is a linear fit. Deviations from the fitting curve originate from different sample volumes at different angles. The displayed pattern is also in agreement with Ref. [118].
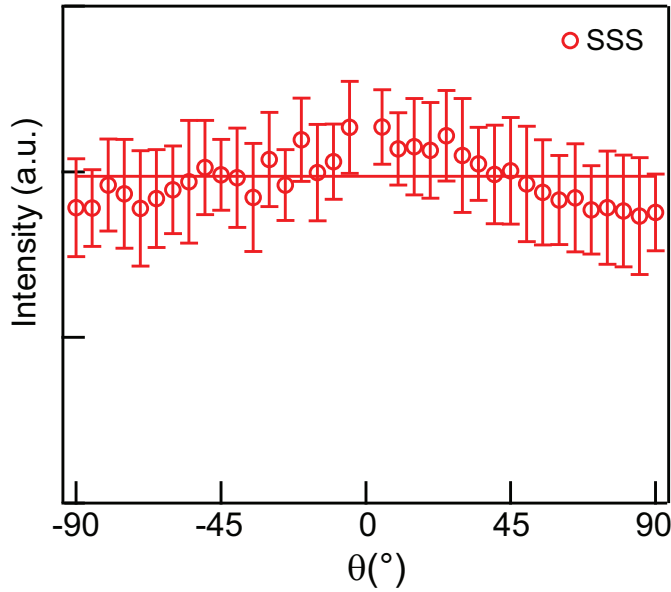
Figure 2.7: Isotropic scattering pattern of water in the SSS polarization combination. 0° is the forward direction of the fundamental beam, the data is not shown here. The pattern was recorded in steps of 5° with an angle of acceptance of 3.4°. Error bars represent the standard deviation of 20 measurements per angle.

2.1.7 General assumptions for nonlinear optical processes

For the theoretical description of the nonlinear optical experiments, we describe the propagation of light in the form of a plane wave. All theoretical calculations in this thesis are based on the Rayleigh-Gans-Debye (RGD) approximation.[99–101,119] The RGD theory assumes that light is neither reflected nor absorbed when crossing a particle.

Within this theory, the scattering response at each point of a particle can be considered isolated without interference from the rest of the particle. It is true when

$$|1 - m| \ll 1$$
$$\frac{2\pi n_s}{\lambda} R |1 - m| \ll 1$$

(2.2)

with m being the ratio between the refractive indices (n_p/n_s) and R the particle size. A negligible dispersion due to small differences in the refractive index may physically not be feasible. However, we can use the RGD theory and correct for the difference between the refractive indices of the particle (n_p) and the solvent medium (n_{H_2O}) using a linear correction term. This correction term accounts for the change of the electromagnetic field when it crosses the interface (Table I in Ref. [99]).

We also assume the absence of multiple scattering in the sample solution. Multiple scattering and other perturbing effects, such as the overlap of the hydration shells surrounding the probed particles, may bias the SH intensity and alter the otherwise linear dependence of the intensity on the scatterer concentration. Schneider *et*
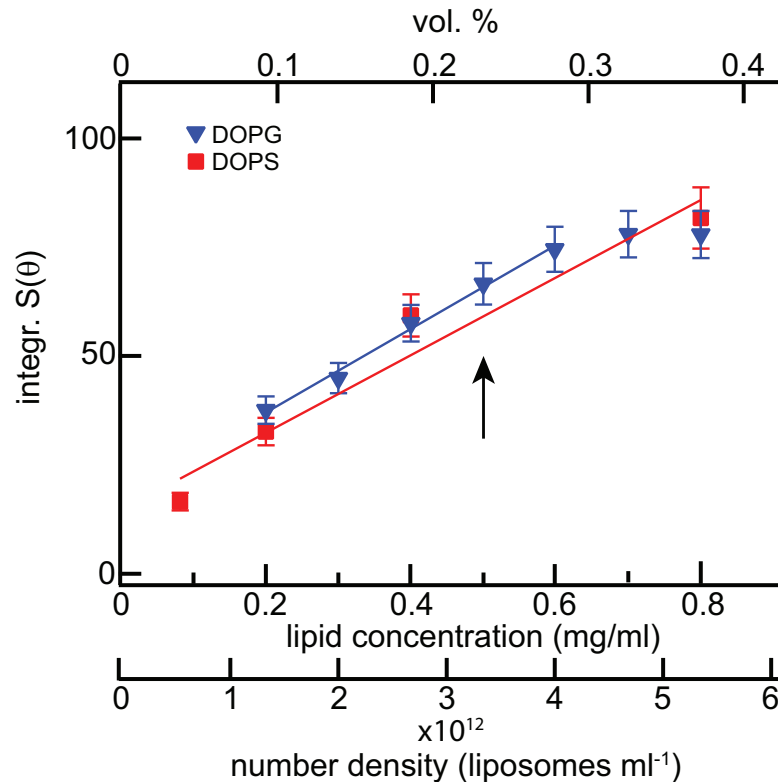
Figure 2.8: Multiple scattering effects in SH experiments. The integrated SH intensity of 100 nm anionic liposomes as a function of lipid concentration in water. Solid lines are linear fits to the data. The arrow indicates the used sample concentration.

al. showed that the size of the particle, the length of the illuminating path, and the change in the refractive index have a critical impact on the linear behavior of the SH intensity in their measurements of polystyrene beads.[120] Liposomes are filled with water and therefore we expect the refractive index to be almost constant.

To verify this assumption and to determine the linear range of lipid concentration in which multiple scattering can be excluded, we measured the SH intensity as a function of the sample concentration. Figure 2.8 shows the SH intensity $S(\theta)$ from anionic liposomes integrated from -90° to 90° as a function of scatterer density expressed in different quantities, lipid weight, volume % and number density. The liposomes had a diameter of 100 nm and were composed of either dioleoylphosphatidylserine (DOPS) or dioleolylphosphatidyl-1'-*rac*-glycerol (DOPG) in water. The error bar represent the angle-integrated standard deviation of 20 measurements per angle. The scattered intensity increases linearly with the number density of the scatterers as expected. Within the tested concentration range, the scattered intensity seems to level off at a critical number density $\sim 4.7 \times 10^{12}$ liposomes/ml (0.7 mg/ml). This may indicate the onset of multiple scattering. At this number density the inter-liposome distance from membrane to membrane is ~500 nm for both samples, which is at the same length scale as the second harmonic wavelength. To avoid possible biases, we used 0.5 mg/ml lipid concentration (as indicated with the arrow).

In addition to these assumptions, we use four common assumptions that are required to treat the recorded data and to develop the mathematical equations. These assumptions are used for the entire thesis and are valid for planar as well as for curved interfaces. They are related to the optical properties of the isotropic materials using nonresonant illumination. If additional assumptions and models are required, these are explicitly stated where they will be used. The four assumptions are:

1. We consider liquids generally as spatially isotropic.[92]

2. We consider that the particle interface is isotropic in the interfacial plane (i.e. the tangential coordinates are degenerate).[92]

3. The sample consists of a lossless and dispersion-free nonlinear medium, which means that no energy is transferred from the optical pulses to the material. This leads to the degeneracy of three of the four tensor elements of $\chi_s^{(2)}\left(\mathbf{\Gamma}^{(2)}\right)$, and $\chi^{(3)'}\left(\mathbf{\Gamma}^{(3)'}\right)$, so that only the pair $\left(\chi_1^{(2)}, \chi_2^{(2)}\right)$ and $\chi_2^{(3)'}$ are non-zero. We verified this assumption by (1) measuring the energy transfer from the beams to the medium (see Fig. 2.4), and (2) by confirming that the polarization combinations PSS, and SPS (or SSP), generate the same responses within the experimental uncertainty (Fig. 2.9).

4. The orientational distribution of water molecules at the interface is broad.[121] Further details are given in chapter 4 and in Ref.[122].
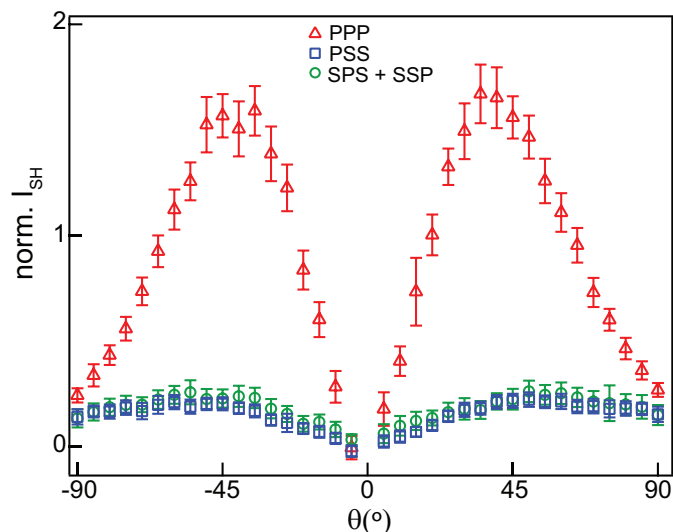
Figure 2.9: Scattering patterns of polystyrene beads Scattering patterns of 200 nm polystyrene beads in 3 polarization combinations PPP, PSS, SPS and SSP. The same magnitudes indicate that the assumption of the degeneracy of the susceptibility elements is correct. Error Bars represent the standard deviation of 20 measurements.

2.2 Complementary experimental techniques & Methodology

We also used linear light scattering and electrophoretic measurements to characterize the size and electrostatic environment of liposomes and droplets.

2.2.1 Dynamic light scattering (DLS)

To determine the average hydrodynamic particle size of a dispersion, we used autocorrelation spectroscopy (Zetasizer Nano ZS, Malvern). In this measurement, the linearly scattered light from the particles is analyzed with respect to the Brownian (random) motion[123] of the particle in solution. The light source is most commonly a 633 nm continuous wave laser. Scattered light can be detected in forward and backward direction. Auto-correlating the scattering signal over time is used to calculate the motion of the illuminated particle which, in turn, can be linked to the size of the particle. The bigger the particle, the slower the movement and hence the correlation coefficient remains constant as a function of time. Figure 2.10 shows the typical slope of a correlogram for two differently sized scatterers, 500 nm silica particles and 60 nm DPPS liposomes in water demonstrating the difference in the correlation coefficient.
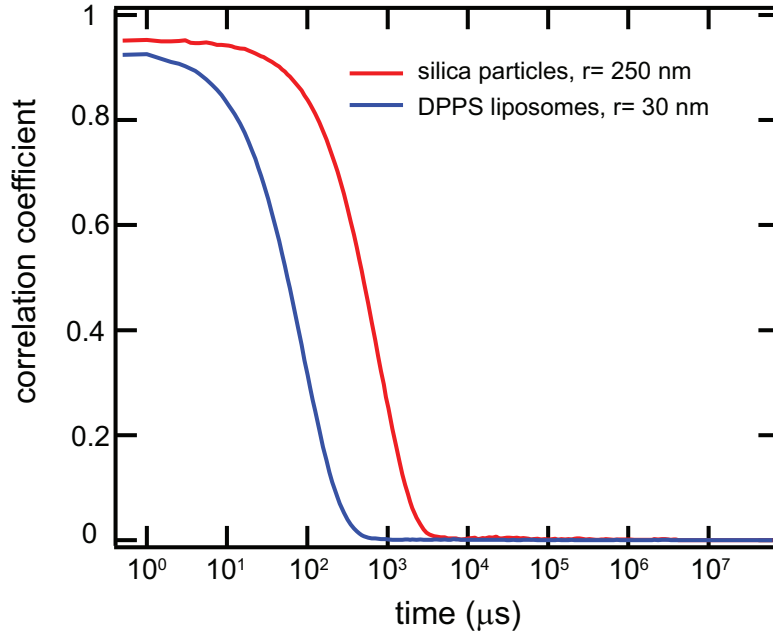
Figure 2.10: Autocorrelation-function for two differently sized particles. The cumulant fit curve from sample solutions containing DPPS liposomes (r= 30 nm,blue) and silica particles (r=250 nm, red)

The autocorrelation function $G(\tau)$ of the intensity is

$$G(\tau) = < I(t) \times I(t+\tau) > \tag{2.3}$$

in which τ is the time difference of the correlator. Assuming that the particles are in Brownian motion, the correlation function $G(\tau)$ can be expressed as

$$G(\tau) = A[1 + Bg(\tau)^2]. \tag{2.4}$$

A represents the baseline of the correlation function and B is the intercept of the correlation function g. For monodisperse solutions this function is an exponential decay according to

$$g(\tau) = e^{-2\Gamma\tau} \tag{2.5}$$

with $\Gamma = Dq^2$. D is the translational diffusion coefficient, q the wave vector depending on the scattering angle (θ), wavelength (λ) and refractive index of the medium (n): $q = (4\pi n/\lambda_0)\sin(\theta/2)$. The translational diffusion coefficient relates to the radius of the particle by the Stokes-Einstein equation[124] assuming a spherical particle so that

$$R_{\text{hydrodynamic}} = \frac{k_B T}{6\pi\eta D}, \tag{2.6}$$

in which k_B is the Boltzmann constant, T the temperature, and η the viscosity of the solution. Note that the assumption of Brownian motion also limits the particle sizes that can be analyzed with DLS measurements. If there is no random movement in the particles, i.e. because of sedimentation, the particles cannot be analyzed.

To describe the intensity-autocorrelation function applying eq. (2.4), two different fitting approaches can be used: the cumulant fit or the non-negative least square method. These approaches consider different sample properties and dispersion qualities. The cumulant fit uses a single exponential to obtain a mean radius and the standard deviation of the distribution, which is expressed in the polydispersity index, $PDI = (\sigma(r)/r)^2$. It is the best fit for describing monomodal modes. Figure 2.11 displays the correlation function with a cumulant fit and the derived size distribution for DOPS liposomes extruded through polycarbonate membranes with 100 nm pore sizes. We used the cumulant fit for all samples.
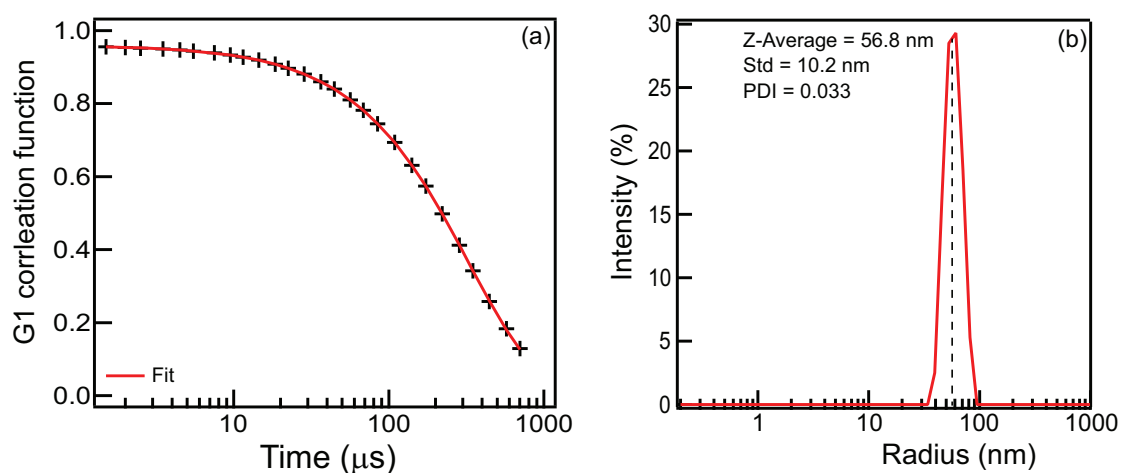
Figure 2.11: Size extraction from DLS measurements. (a) The size is determined by fitting the beginning of the correlation data with a cumulant fit considering a monodisperse solution, here for DOPS liposomes in water extruded through 100 nm pores. Deviations from this fit become apparent in the width of the displayed distribution and are expressed in the PDI. (b) The extracted typical size distribution showing a very low PDI calculated from the fit in panel (a).

2.2.2 Calculation of the scattering efficiency A

In order to get a comparable value for the SHS or SFS intensity from different samples and to quantify for instance hydration effects, we normalized the intensity by the number of droplets (N_d) or liposomes (N_{lip}). For a monodisperse solution of droplets or liposomes that are smaller than ~200 nm in radius, the total scattered signal (S)

from a solution with N_p particles that each scatter an intensity $I(\theta)$ scales with[102]

$$S(\theta) = I(\theta) N_p \propto A(\theta) N_p R^6. \tag{2.7}$$

The factor $A(\theta)$ is the scattering efficiency and contains all the information about the surface response per droplet / liposome, independent of its size. Thus, if we want to compare the water response as a function of surface effects for a droplet or liposome we have to compute the following

$$A(\theta) = \frac{S(\theta)}{N_p R^6} = I_{\text{norm}}(\theta, R). \tag{2.8}$$

We use eq. (2.8) in chapter 5 and 6. When using such a correction, it is convenient to convert the particle distribution as displayed in Fig. 2.11b to a single size value correcting for the already low polydispersity. Correcting for the distribution it is convenient to replace the average radius R (Z-average) with an effective radius R_{eff}. This procedure results in a more appropriate representation of the scattering efficiency A, because it allows for a systematic error estimate of the size measurements. The conversion procedure to determine R_{Eff} is described in the next section.

2.2.3 Calculation of an effective radius

All particles contribute in the same way to the overall intensity of any light scattering experiment in dilute conditions. Thus, we can use the DLS data to compute an effective radius that can be used in the analysis of SHS and SFS experiments with polydisperse samples. DLS uses the temporal autocorrelation of scattered light to measure an intensity-weighted particle size distribution histogram. The output of such a measurement is a (normalized) distribution D(R), which we use here to correct the SHS and SFS signal for variations in the droplet / liposome size distribution. In other words, we want to replace the total DLS intensity from a polydisperse distribution $\sum_i I(R_i)$ by an intensity $I_{\text{norm}}(\theta, R_{\text{eff}})$ from a 'monodisperse' solution. The obtained effective radius can then be used to normalize the SH intensity according to Eq. 2.8. Explicitly, from Eq. 2.8, we have

$$A(\theta) = \frac{\sum_i I_i(\theta)}{N_p R^6} = \frac{S(\theta)}{N_p R_{\text{eff}}^6} = I_{\text{norm}}(\theta) \tag{2.9}$$

In the RGD limit, which is applicable here[79], the intensity of scattered light in a DLS measurement also scales with R^6, so that

$$D(R) = \frac{P(R) R^6}{\int P(R) R^6 dR} \tag{2.10}$$

The particle size distribution P(R) is a normalized probability distribution, such that $\int P(R)\,dR = 1$. We can calculate the particle size distribution from the DLS intensity-weighted distribution by

$$P(R) = \frac{D(R)}{R^6} / \int \frac{D(R)}{R^6}\,dR \tag{2.11}$$

Using the particle size distribution, we can calculate the effective radius for the liposomes using

$$R_{\text{eff,lip}} = \left[\frac{\int P(R)\,R^6 dR}{\int \frac{1}{2}P(R)\left(R^2 + (R-d)^2\right)dR} \right]^{1/4} \tag{2.12}$$

in which the denominator takes into account that the altered radius also affects the number of lipids per liposome (i.e. size and number density are related). For droplets, we have the following expression

$$R_{\text{eff,oil}} = \left[\frac{\int P(R)\,R^6 dR}{\int P(R)\,R^3 dR} \right]^{1/3} \tag{2.13}$$

in which the denominator is now representing a sphere rather than a hollow shell.

2.2.4 Electrophoretic measurements and the ζ-potential

Any material that gets in contact with an aqueous solution will acquire charges. For colloidal solutions, this phenomenon can be crucial for the stability of the dispersion. According to the Derjaguin-Landau-Verwey-Overbeek (DLVO) theory,[67,125] the stability depends on the trade-off between the short ranged attractive van-der-Waals-forces and the electrostatic repulsion generated by surface charges. Dispersions can be stabilized by two different means: Electrostatic stabilization or steric hindrance. Steric hindrance can be obtained by modifying the surface chemistry with bulky molecules, e.g. by polymer brushes. In this case, the distance between the particles remains larger than the effective range of the van-der- Waals force. Electrostatic hindrance originates from the surface charges of particles that result in repulsion of particles carrying surface charges of the same polarity. The acquisition of surface charges and thus the level of electrostatic interactions are highly dependent on the composition of the solution, i.e. pH, ionic strength, temperature and pressure. A convenient parameter to describe the stability of such solutions is the ζ-potential, which is as sensitive to the composition of the solution as are the surface charges themselves.[67]

The ζ-potential is an electrokinetic potential representing not the material's bare surface charge but the ion atmosphere around a particle. Figure 2.12 sketches

the interfacial ion distribution around a charged particle in an aqueous solution. The charges at the surface of the particles determine the distribution of ions in solution around these particles: Counterions are attracted whereas coions are repulsed from the interface. These interactions create an ion distribution that becomes more dilute with distance from the interface. This typical ion distribution is known as the electric double layer (EDL).[66] Close to the interface, there is a build-up of counterions resulting in a very high density which becomes particularly evident at moderate and high salt concentrations (> 10mM). This region is labeled Stern layer in Fig. 2.12. With increasing distance the ion distribution becomes more homogeneous and the counterion concentration follows an exponential decay into the bulk. This region represents the diffuse layer.

Depending on the surface charge and ion concentration, a particle will move in the solution when an external electric field exerts a force on the particle. The direction and velocity of the particle's movement depends on the sign and magnitude of the surface charges. While moving, the tightly bound ions at the particle interface will move with the particle, whereas shear forces prevail at a certain distance away from the interface. At this distance the diffusely attached ions will not be dragged along with the particle and remain behind. The distance at which the friction becomes bigger than the electrostatic interaction between ion and surface is the slipping plane, also known as the surface of hydrodynamic shear. The ζ-potential is defined as the potential at this plane. It is,though, not feasible to determine the position of the slipping plane exactly. However, over the last decades it became popular to align the slipping plane with the Stern layer distance, which enables one to quantify the ion distribution, capacitance of the Stern layer, and the diffuse layer charges.

The ζ-potential can be calculated by determining the electrophoretic mobility using Laser Doppler anemometry. Here the velocity of particles in solution are measured when accelerated by an externally applied electric dc-field. When an equilibrium between the accelerating forces and the viscous forces that oppose this movement is created, the velocity will be constant. The velocity of the samples is then determined analyzing the phase difference between the sample beam and a reference beam for a known electric field strength. The ratio between the velocity and the electric field strength is the electrophoretic mobility

$$\mu_{el} = \frac{v}{E_{ext}} \tag{2.14}$$

From the electrophoretic mobility the ζ-potential can be calculated using the Henry equation

$$\mu_{el} = \frac{2\epsilon\zeta f(\kappa a)}{3\eta}, \tag{2.15}$$
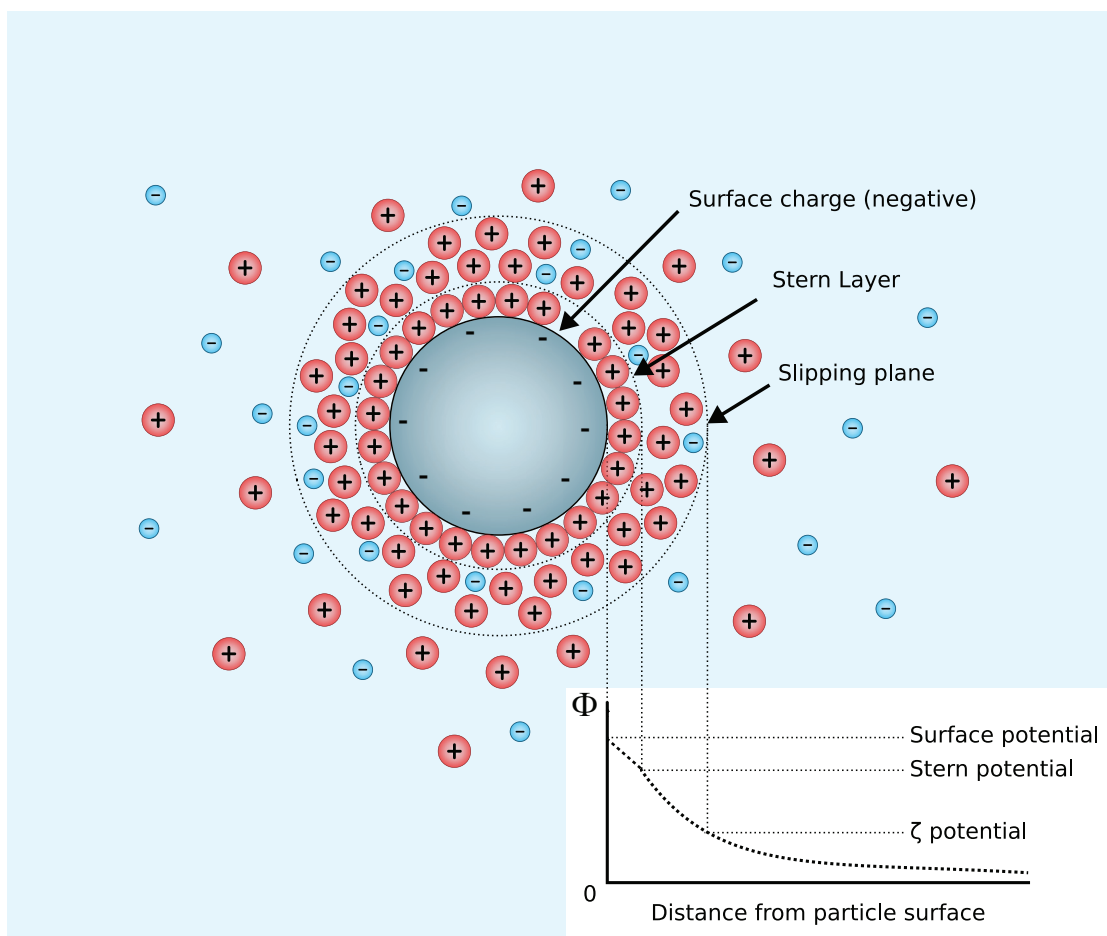
Figure 2.12: Ion distribution around a particle. Sketch of the ion distribution and density around a charged particle immersed in an aqueous solution. Graphic adapted from Ref. [126].

in which ϵ, ζ, η and $f(\kappa a)$ are the dielectric constant, the ζ-potential, the viscosity of the medium, and Henry's function. a is the radius of the particle. κ is the Debye parameter (in SI units and c in mol/l)[127]

$$\kappa = \sqrt{\frac{2000e^2 N_{Av} z^2 c}{\epsilon_0 \epsilon_r k_B T}}$$

The solution to $f(\kappa\alpha)$ is nonlinear. Therefore, $f(\kappa a)$ is usually approximated by the Smoluchowski or the Huckel solution. In the Smoluchowski approximation $f(\kappa a)$ the maximum value is 1.5, whereas in the Huckel approximation the minimum value is 1. Most samples are in between these margins without a simple solution. The Smoluchowski approximation is suitable for particle sizes ~100 nm and Debye lengths (κ^{-1}) that are at teh order and shorter than the particle radius. This is typically the case for aqueous solutions with moderate ionic strength (> 100 μM). We always used

the Smoluchowski approximation.

2.3 Sample preparation & Characterization

2.3.1 Lipids

The used lipids in this thesis vary in the headgroup structure, the length and saturation of the fatty acid tails, and the overall molecular dimensions. The headgroup structure enables the molecules to create intermolecular interactions via hydrogen-bonding and determines the lipid charge. Headgroup and structure of the fatty acid chains together define the occupied hydrated volume in the membrane. The used lipids vary in their length and saturation level. We use saturated and unsaturated lipids that affect the lipid packing, thickness and fluidity of the membranes. The studied lipids are listed in Fig. 2.13 and ordered according to their chain saturation, charge and hydrocarbon chain length. The abbreviations in Fig. 2.13 refer to: 1,2-dioleoyl-*sn*-glycero-3-phosphoethanolamine (DPPE), 1,2- dipalmitoyl-*sn*-glycero-3 phospho-choline (DPPC), 1,2- dipalmitoyl-*sn*-glycero-3-phosphate (DPPA), 1,2- dipalmitoyl-*sn*-glycero-3 phospho-L-serine (DPPS), 1,2-dioleoyl-*sn*-glycero-3-phosphocholine (DOPC) 1,2-dioleoyl-*sn*-glycero-3-phospho-L-serine (sodium salt) (DOPS) and 1,2-dioleoyl-*sn*-glycero-3-phospho-(1'-*rac*-glycerol) (sodium salt) (DOPG). For the sum-frequency studies in chapter 5, we also used deuterated DOPC and DPPS. Only the fatty acid chain in these two molecules (highlighted in blue) were substituted with deuterated carbons (CD_2 and CD_3). Thus, an artificial contrast for SFS measurements could be generated whereas the headgroup structures remained hydrogenated.

2.3.2 Liposome formation

Small unilamellar vesicles were prepared by extrusion according to Ref. [128, 129]. To create multilamellar vesicles, typically 3 mg lipid powder was dissolved in chloroform in a round-bottom glass tube. For liposomes composed of several lipids at a specific ratio, the respective lipids were weighted and diluted in chloroform. Then, volumes of each stock were mixed together using a glass syringe (Hamilton). Subsequently, the chloroform was evaporated with a gentle N_2 gas stream under constant rotation of the tube. The glass tube was placed in a desiccator and the lipid film was further dried in vacuum (<100 mbar, created by an oil-free diaphragm pump) for at least 1.5 hours. Finally, the lipid film was re-suspended in 1ml H_2O or D_2O (99.8 %, Armar, > 2MΩ cm), respectively, and vortexed. To create unilamellar vesicles, the multilamellar vesicle solutions were extruded with a Miniextruder (AvantiPolarLipids, Al) using a polycarbonate membrane (Merck Millipore) with a pore diameter of typically 100 nm at room temperature (or above their respective lipid transition temperature). To obtain differently sized liposomes, extrusion was done with polycarbonate membranes having pore sizes of 30 nm, 50 nm, or 200 nm, respectively. The solution was pressed
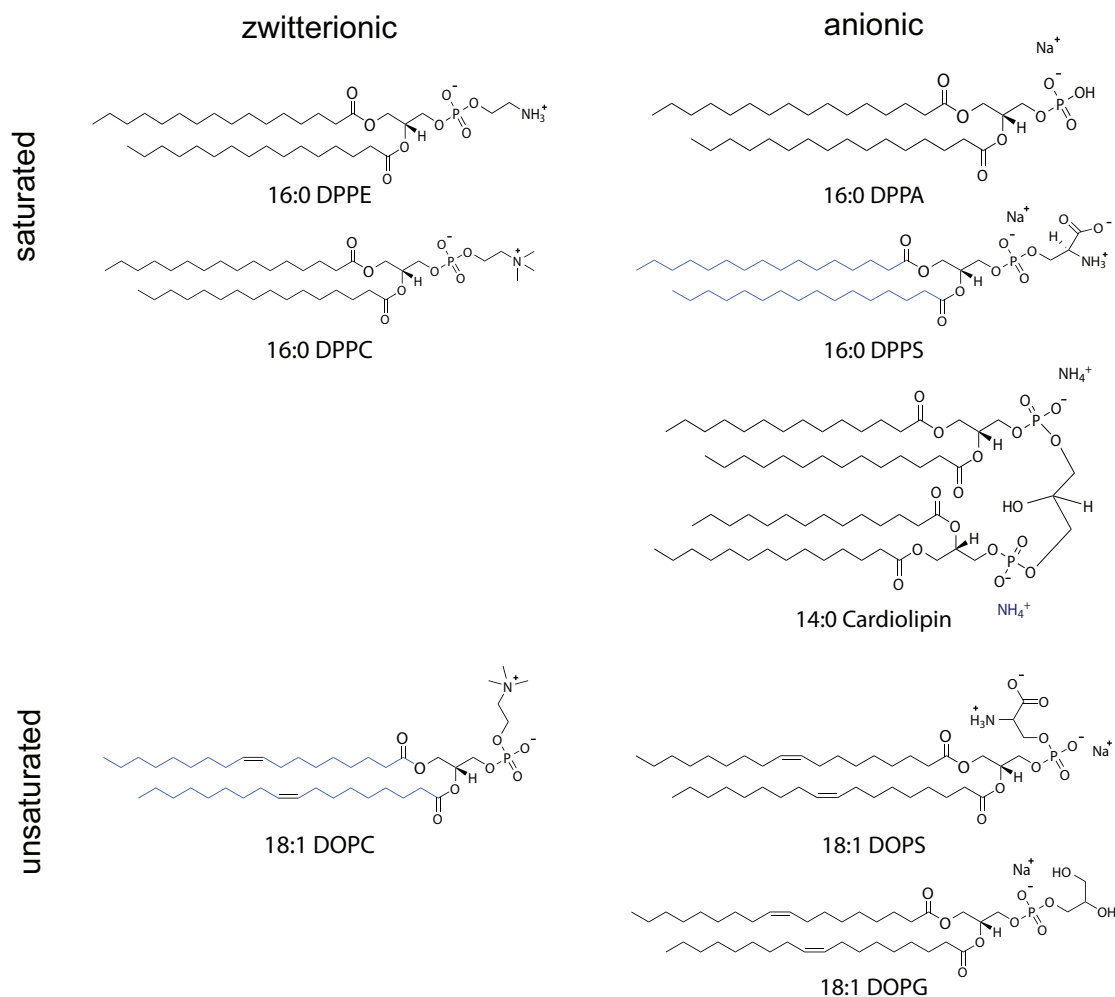
Figure 2.13: Molecular structures of used phospholipids. For the formation of liposomes and lipid droplets, we used diverse zwitterionic and anionic lipids that vary in their headgroup structure, their length (14-18 C atoms) and their rotational freedom of the hydrocarbon chains. The presence of a C-C double bond (unsaturated) limits the tilt angle of the hydrocarbon chains and leads to a less dense packing. For chapter 5 we also used deuterated versions of DOPC and DPPS. In this case the hydrocarbon chains highlighted in blue were substituted with deuterated carbon chains leaving the headgroup unmodified.

51 times through the membrane to obtain unilamellar vesicles. The temperature of the solution was always kept above the transition temperature of the lipids during this process. Unilamellar vesicles were stored in closed containers up to 2 weeks at 4 °C under an N_2-gas atmosphere. The liposome stock solutions were diluted with respective amounts of water or electrolyte containing solutions prior to the measurements. The size and ζ-potential distribution of the liposomes were measured with DLS and electrophoretic measurements at 24 °C (Malvern ZS nanosizer). To determine the size distribution of the vesicles, three subsequent measurements, each 11

runs, were averaged. To determine the ζ-potential of the vesicles three subsequent measurements, each 75 runs at automated voltage, were averaged. The final lipid concentration was determined using a calorimetric phosphorus assay, a by now well established quantification method of phospholipid content (see Ref. [130]). A detailed protocol can be found in Ref. [131]. The concentration of the lipids in the sample was 0.5 mg lipids/ ml (*w/w*) for DLS, ζ-potential measurements, and SHS experiments.

2.3.3 Determination of total phosphorus content

The lipid concentration of the liposome stocks may be different from the theoretically calculated concentration because of various experimental influences:

1. The weighted quantity may vary because of systematic errors. It is also rather likely to lose lipids during the handling when transfering liquids to different vials.

2. The relatively rapid evaporation of chloroform in ambient conditions can bias the stock concentration as well.

3. During the extrusion process part of the lipids may get stuck in the polycarbonate filter membrane depending on pore size and lipid chemistry.

Hence, to verify the lipid concentration of the final liposome solution, we indirectly quantified the phosphate content of the samples with a colorimetric assay. All used lipids were phospholipids so that the amount of phosphate is directly proportional to the number of lipid molecules. The combination of phosphate ions with ammonium molybdate results in a phospho-molybdate complex that fluoresces blue. In order to create phosphate ions, the lipids need to be digested so that all organic content vanishes. The complex formation happens under acidic conditions and in the presence of ascorbic acid to prevent oxidization of the formed complex. Analyzing the light absorbance at a specific wavelength, here 800 nm, with a UV-VIS spectrometer from standards and sample solutions, the respective amount of phosphate can be determined. A detailed protocol including all necessary steps can be found in Ref. [131].

2.3.4 pH stability of aqueous solutions over time

As stated in the previous section, we stored the liposome solution for several days in screw-cap vials. Over this duration, the pH of the solution may change due to CO_2 absorption. Such pH change may lead to a difference in the ionization of the lipids and the surface chemistry, which could have severe impacts on the drawn conclusions. To quantify the degree of pH change, we measured the pH as a function of time of nanopure water with 10 μM NaCl in closed screw-cap vials (~ 20ml volume)

and in contact with a N_2 atmosphere over the duration of 7 consecutive days with a commercial pH meter (HI5255, Hanna Inst.). Typical liposome stock solutions as used in this work have at least 10 μM ionic strength. Figure 2.14 shows the recorded data for the aqueous samples. Data points are averages of 3 measurements of a single vial with the error bar representing the standard deviation. In open vials the pH value drops to pH~ 5.8 (*not shown*). In closed vials the pH remains almost constant over 1 week, and biasing effects can be neglected. We will see further evidence for stable pH values in chapter 6.
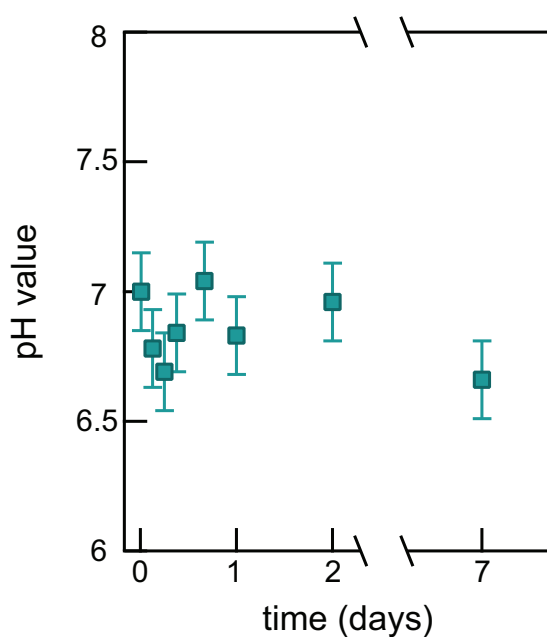
Figure 2.14: The pH stability of aqueous solutions over time. pH was measured in 10 μM NaCl solutions that were stored in closed screw-cap vials in contact with an N_2 atmosphere. Courtesy of H. Okur.

3 | Modulation of second harmonic and sum-frequency generation from aqueous interfaces by interference

The interfacial region of aqueous systems, also known as the electrical double layer, can be characterized on the molecular level with second harmonic and sum frequency generation (SHG/SFG). SHG and SFG are surface specific methods for centrosymmetric isotropic liquids. In this chapter, we model the SHG/SFG intensity in reflection, transmission and scattering geometry taking into account the spatial variation of all optical and electric fields. We show that, in the presence of a surface electrostatic field, interference effects that originate from differently oriented water molecules on a length scale over which the potential decays, can strongly modify the probing depth as well as the expected intensity at ionic strengths $< 10^{-3}$ M. For reflection experiments this interference phenomenon leads to a significant reduction of the SHG/ SFG intensity. In transmission mode experiments from aqueous interfaces this phenomenon is present, but barely affects the measurement. For SHG/ SFG scattering experiments this same interference leads to a change in intensity and to different scattering patterns, which can be independently described.

3.1 Introduction

Ions modify the structure and dynamics of water. In contact with an interfacial region, ions change the physical, chemical, electrostatic and biochemical properties of a material.[84,132–134] Quantifying the molecular properties of the electrical double layer (EDL), which consist of the interface itself as well as the diffuse EDL (DDL), is important for many processes in biology and chemistry. Many methods exist for this purpose: employing electrokinetic mobility,[127,135] scattered or reflected, visible or X-ray photons and neutrons,[136,137] vibrational spectroscopy,[84,96,134] photoelectron spectroscopy[138] and nonlinear optical methods, such as second harmonic and sum-frequency generation (SHG/SFG).[86,139–143] What all of these methods have in common, and what considerably complicates the interpretation of data and the formulation of a consistent molecular level picture of the EDL, is that the interfacial region and its thickness can be chosen in different ways.[90,95,144–146] The interfacial thickness typically depends on the sensitivity, the background, and penetration depth of the method. SHG and SFG are background free methods and thus the probing depth depends on the requirement of spatial non-centrosymmetry of the material: Typically, the definition of the interface is the region where centrosymmetry is broken, provided that it is located between isotropic media.[85] SHG and SFG are thus ideal methods for probing molecular level details of the aqueous interface, which one normally considers to be only a few molecular dimensions thick (see Refs. [84, 86, 96, 134, 141] for excellent reviews). However, when there is an (electrolyte dependent) electrostatic field in the interfacial region, water molecules in the EDL reorient (even if they are isotropically distributed in absence of an electrostatic field). The reorientation results in a small amount of centrosymmetry breaking, leading to an additional contribution to the nonlinear optical response.[95,146,147] Consequently, the probed, interfacial thickness changes in the experiment. At the same time, the optical beams vary in phase as they propagate in the aqueous phase, which may result in interference effects with the spatially varying electrostatic field. Does this influence the probing depth and does it depend on electrolyte concentration? Can we still assume that we probe only the first few molecular diameters at the interface? Interpretating SHG and SFG data, we need to take these factors into account.

In this chapter, we consider these questions, following the trend set by various previous studies.[84,90,103,141,146,148,149] We take into account the ionic strength range from 10^{-7} to 10 M and derive a theoretical expression for the SHG/SFG response. We calculate the SHG and SFG response from an aqueous planar interface in reflection and transmission geometry and an aqueous colloidal interface in scattering geometry. Based on our findings, it turns out that the probing depth into the bulk solution varies with ionic strength and that, in certain experimental conditions, the probing depth can be as deep as 1 μm. Within this 1 μm thick region, interference effects

between photons, which are generated at different distances away from the Gibbs dividing surface of the interface, alter the expected intensity considerably. For reflection mode experiments this may result in a significantly lower intensity at low ionic strengths than what one would expect. Furthermore, the interference effect at low ionic strengths effectively reduces the probing depth to a distance that is –in the limit of an infinite Debye length- similar to the probed, interfacial region in the absence of an electrostatic field. For transmission experiments this effect has barely an influence. For nonresonant angle-resolved scattering[106,113,150] experiments, the contribution from the diffuse EDL increases the intensity and modifies the angle- specific scattering leading to different scattering patterns, which give us the opportunity to separate the surface signal from that of the DDL.

In the first part of this chapter, we describe reflection and transmission mode experiments considering a theoretical background in the most general way (applicable to sum-frequency generation) to which we add the expected changes when interference occurs. We then describe the result related to the probing depth and make a comparison to previous reflection mode studies in the literature. In the second part of this chapter, we describe the theoretical background (using the Rayleigh-Gans-Debye approximation) for second harmonic and sum-frequency scattering (SHS/SFS), adapt the formalism to incorporate scattering form the DDL, and examine the probing depth. Finally, we compare reflection, transmission and scattering experiments.

3.2 Results & Discussion

3.2.1 SHG/ SFG in reflection mode

Theoretical background. In the electric-dipole approximation,[151] in an SFG process two optical fields

$$\mathbf{E}_1(\omega_1) = E_1(\omega_1, k_1)\boldsymbol{u}_1 = E_1(\omega_1)e^{-i(\omega_1 t - k_1 r)}\boldsymbol{u}_1 \text{ and}$$

$$\mathbf{E}_2(\omega_2) = E_2(\omega_2, k_2)\boldsymbol{u}_2 = E_2(\omega_2)e^{-i(\omega_2 t - k_2 r)}\boldsymbol{u}_2$$

with wave vectors and frequencies $\mathbf{k}_1, \omega_1$ and $\mathbf{k}_2, \omega_2$ interact with an interface that is characterized by a surface second-order susceptibility $\chi_s^{(2)}(\omega_0 = \omega_1 + \omega_2)$. For SHG $\omega_1 = \omega_2$ and $\mathbf{k}_1 = \mathbf{k}_2$. The second-order nonlinear optical polarization $\mathbf{P}^{(2)}(\omega_0)$ that results from the interaction of the beams with surface is

$$\mathbf{P}^{(2)}(\omega_0) = \epsilon_0 \boldsymbol{\chi}_s^{(2)} : \mathbf{E}_1(\omega_1)\mathbf{E}_2(\omega_2). \tag{3.1}$$

$\chi_s^{(2)}$ is the surface susceptibility, a macroscopic property of the material. The magnitude of the surface susceptibility depends on the molecular hyperpolarizability $\boldsymbol{\beta}^{(2)}$ of the interfacial molecules and their respective degree of ordering in the interfacial

region. In a label-free nonresonant SHG experiments, the $\boldsymbol{\beta}^{(2)}$ of water molecules are responsible for the signal, because of their strong dipole moment. The degree of molecular orientation at the surface is contained in the susceptibility value. The molecular orientation can be transformed to a surface response by transforming $\boldsymbol{\beta}^{(2)}$ to $\boldsymbol{\chi}_s^{(2)}$ using a rotation around the molecular symmetry axis, an angular tilt (ϕ) and a rotation around the interface normal(ψ).[101] However, assuming interfacial isotropy, the rotations become redundant so that only the molecular tilt perpendicular to the interface determines the respective $\boldsymbol{\chi}_s^{(2)}$ elements. For the following derivation and implementation of interference effects as well as to highlight the overall signal sensitivity, we do not require the mathematical describtion of this transformation nor a molecular level picture. Hence, we skip this description here, but, for completeness, we give the required expressions in the Appendix (8.1) according to Ref. [122].

The ordering of interfacial molecules can also be affected by surface charges and ions in solution that generate an electrostatic field in addition to the optical fields. We have to consider this E-field by implementing an additional interaction term in the nonlinear polarization.[92,93,100,103,152,153] For a reflection mode experiment with the interface placed at $z = 0$ (Fig. 3.1a), we thus have $\mathbf{E}(\omega = 0, z) = \mathbf{E}_{dc}(z) = -\nabla\Phi(z)$ and the nonlinear polarization becomes

$$\mathbf{P}_{NL}(\omega_0) = \mathbf{P}^{(2)}(\omega_0) + \mathbf{P}^{(3)}(\omega_0) + \dots, \text{ with}$$

$$\mathbf{P}^{(3)}(\omega_0) = \int_0^{+\infty} \mathbf{P}^{(3)}(\omega_0, z) \mathrm{d}z \text{ and} \tag{3.2}$$

$$\mathbf{P}^{(3)}(\omega_0, z) = \epsilon_0 \boldsymbol{\chi}^{(3)'} : \mathbf{E}_1(\omega_1)\mathbf{E}_2(\omega_2)\mathbf{E}_{dc}(z).$$

Here, $\boldsymbol{\chi}^{(3)'}$ is an effective third-order susceptibility tensor. $\boldsymbol{\chi}^{(3)'}$ represents all processes that lead to emission at ω_0 and that require an interaction with $\mathrm{E}_{dc}(z)$. In label-free experiments, this includes E_{dc}-oriented water molecules at the interface and in the bulk solution $\left(\boldsymbol{\beta}^{(2)}\right)$ as well as a pure third-order interaction that is mediated by the isotropic third-order susceptibility of bulk water $\boldsymbol{\chi}_b^{(3)}$ (originating from the molecular third-order polarizability $\boldsymbol{\beta}^{(3)}$). $\mathbf{P}^{(3)}(\omega_0, z)$ is a function of z because the electrostatic field changes in the direction perpendicular to the interface. The total $\mathbf{P}^{(3)}(\omega_0)$ polarization is obtained by an integration over z.[95] Assuming isotropy in the x and y directions the amplitude of $\mathbf{P}^{(3)}(\omega_0)$ becomes

$$\mathrm{P}^{(3)}(\omega_0) = \epsilon_0 \int_0^{+\infty} \chi^{(3)'} E_1(\omega_1, k_1) E_2(\omega_2, k_2) E_{dc}(z) \mathrm{d}z \tag{3.3}$$

Integrating, one obtains

$$
\begin{aligned}
P^{(3)}(\omega_0) &\propto \chi^{(3)'} E_1(\omega_1, k_1) E_2(\omega_2, k_2) \int_0^{+\infty} E_{dc}(z) dz \\
&= \epsilon_0 \chi^{(3)'} E_1(\omega_1, k_1) E_2(\omega_2, k_2) \Phi_0,
\end{aligned}
\tag{3.4}
$$

in which Φ_0 represents the surface potential. The surface potential of an object in solution with the surface at R is: $\Phi_0 = -\int_\infty^R E_{dc}(r) dr$, where r indicates the distance away from the interface and E_{dc} is the total electrostatic field that emerges from all possible sources of charges in solution.[154]

Interference and the DDL at planar interfaces. Provided one knows the relationship between Φ_0, the ionic strength (c) and the surface charge, Eq. (3.4) allows to estimate the surface potential Φ_0 by the Eisenthal $\chi^{(3)}$-method, utilizing a reflection mode SHG experiment as sketched in Fig. 3.1a,[95,103,141] with $\omega_1 = \omega_2$ and $\mathbf{k}_1 = \mathbf{k}_2$. Eq. (3.4) assumes that the optical fields are independent of z, meaning that the phases of the incoming and returning fields do not change in the region where E_{dc} is nonzero. We can validate this assumption by comparing the z-dependent decay of the electrostatic potential $\Phi(z)$ to the phase change of the generated SHG/ SFG field originating from different z-planes. For a planar surface with an electrostatic potential that decays as $e^{-\kappa z}$, in which κ^{-1} is the Debye length, the potential has decayed to 2 % of its maximum value at $z = 4\kappa^{-1}$ (Fig. 3.1b). The wave vector mismatch for SHG/ SFG photons generated at different probing depth is[155]

$$
\Delta k_z = |\mathbf{k}_{1z} + \mathbf{k}_{2z} - \mathbf{k}_{0z}| = k_{1z} + k_{2z} + k_{0z} \text{ with } k_{iz} = \frac{\omega_i}{c}\sqrt{n(\omega_i)^2 - \sin(\theta_i)^2}, \tag{3.5}
$$

in which $n(\omega_i)$ is the refractive index of the media and θ_i is the angle between the incoming $\mathbf{k}_i$-vector and the surface normal in air for each beam i (sketched in Fig. 3.1a). In an experiment performed at the air/water interface with $\theta_{1,2} = 45°, \lambda_1 = \lambda_2 = 800$ nm, the phase of the generated SHG beam changes by π at a distance $z = 88$ nm ($\pi \Delta k_z^{-1} = 88$ nm, the black line in Fig. 3.1b). Thus, at ionic strengths for which E_{dc} is insufficiently screened so that it is still present beyond $\pi \Delta k_z^{-1}$, we can expect that Eq. (3.4) becomes invalid. To take this fact into account, we have to incorporate a z-dependence in the optical beams of Eq. (3.3) at certain ionic strengths. From Fig. 3.1b, we can estimate that this will be the case if $c \leq 10^{-3}$ M assuming a monovalent electrolyte. Correcting for the z-dependence, we need to change (3.3) accordingly into

$$
P^{(3)}(\omega_0) = \epsilon_0 \int_0^{+\infty} \chi^{(3)'} E_1(\omega_1, k_1) E_2(\omega_2, k_2) E_{dc}(z) e^{i\Delta k_z z} dz, \tag{3.6}
$$
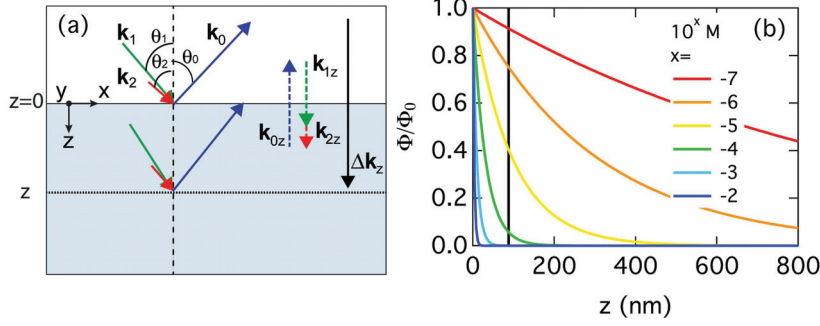
Figure 3.1: (a) Illustration of an SFG reflection experiment at the air/ water interface. Arrows $\mathbf{k}_1$, $\mathbf{k}_2$, and $\mathbf{k}_0$ refer to the visible, IR, and sum-frequency beams that can interact at various z-planes. The dashed arrows refer to their projection along the z-axis, and the relevant phase difference. Δk_z is also illustrated. For collinear SHG $\mathbf{k}_1 = \mathbf{k}_2$ and $\omega_1 = \omega_2$. (b) Exponentially decaying electrostatic potentials of the form $\Phi(z) = \Phi_0 e^{-\kappa z}$ for ionic strenghts of (red) 10^{-7}, (orange) 10^{-6}, (yellow) 10^{-5}, (green) 10^{-4}, (cyan) 10^{-3}, (blue) 10^{-2} M. The black line indicates the distance $z = 88$ nm at which, in the current geometry, $\Delta k_z z = \pi$.

which is identical to

$$P^{(3)}(\omega_0) = \epsilon_0 \chi^{(3)'} E_1(\omega_1) E_2(\omega_2) \int_0^{+\infty} \left(-\frac{\mathrm{d}}{\mathrm{d}z}\Phi(z) \right) e^{i\Delta k_z z}\mathrm{d}z \qquad (3.7)$$

using $E_{\mathrm{dc}}(z) = -\frac{\mathrm{d}}{\mathrm{d}z}\Phi(z)$. Integration by parts of the integral in Eq. (3.7) returns the following expression

$$P^{(3)}(\omega_0) = \epsilon_0 \chi^{(3)'} E_1(\omega_1) E_2(\omega_2) \left(\Phi_0 + i\Delta k_z \int_0^{+\infty} \Phi(z) e^{i\Delta k_z z}\mathrm{d}z \right). \qquad (3.8)$$

To evaluate the expression in Eq. (3.8), we need an analytical expression for $\Phi(z)$ in the second term. We can use for $\Phi(z)$ the DDL equation $\Phi(z) = \Phi_0 e^{-\kappa z}$ without loss of generality because this part in eq. (3.8) only contributes to the expression several nanometers away from the interface. This also means that the integral in Eq. (3.8) does not contribute to the polarization at ionic strengths $> 10^{-2}$ M. Thus, above this ionic strength, the result will not depend on the functional form chosen to describe $\Phi(z)$. Note that, as the integral in Eq. (3.8) does not contribute to the outcome of the expression beyond several nanometers, an explicit incorporation of a Stern layer would not result in very different intensities. Substituting the diffuse double layer equation and integrating, we obtain

$$\begin{aligned} P^{(3)}(\omega_0) &= \epsilon_0 \chi^{(3)'} E_1(\omega_1) E_2(\omega_2) \Phi_0 \frac{\kappa}{\kappa - i\Delta k_z} \\ &= \epsilon_0 \chi^{(3)'} E_1(\omega_1) E_2(\omega_2) \Phi_0 f_3(\kappa, \Delta k_z). \end{aligned} \qquad (3.9)$$

Finally, the emitted intensity is

$$I(\omega_0) \propto \left| P^{(2)}(\omega_0) + P^{(3)}(\omega_0) \right|^2 \tag{3.10a}$$

$$I(\omega_0) \propto I_1(\omega_1) I_2(\omega_2) \left| \chi_s^{(2)} + \chi^{(3)'} \Phi_0 \frac{\kappa}{\kappa - i\Delta k_z} \right|^2. \tag{3.10b}$$

One still needs to insert the appropriate tensor elements for $\chi_s^{(2)}$ and $\chi^{(3)'}$, and the respective Fresnel coefficients that depend on the used polarization combination, the materials, and the optical geometry in order to utilize Eq. (3.10b).[156] Also, note that we considered in this derivation $\chi_s^{(2)}$ to be constant, which means that we do not take any chemical surface changes into account.
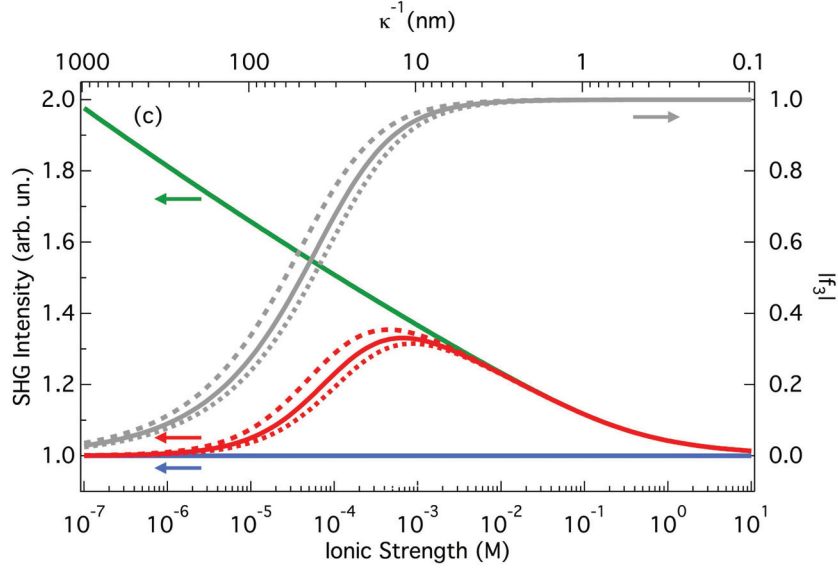
Figure 3.2: Calculated SHG intensity (left axis) as a function of ionic strength considering (blue line) only $\chi_s^{(2)}$, using Eqs. (3.1) and (3.10a), (green line) $\chi_s^{(2)}$ and $\chi^{(3)'}$ contribution, using Eqs. (3.4) and (3.10a), and (red line) both effects together with the interference term $\left| f_3(\kappa, \Delta k_z) \right|$ using Eq. (3.10b). The magnitude of the correction factor $\left| f_3(\kappa, \Delta k_z) \right|$ (grey line) is also shown as a function of ionic strength (right axis). We used the following parameters: $\left| \chi_2^{(2)} \right| = 1$, $\left| \chi^{(3)'} \right| = -1$, $\theta_1 = \theta_2 = 45°$, $\lambda_1 = \lambda_2 = 800$ nm, $n_{air} = 1$, $n_{H_2O}(800 \text{ nm}) = 1.33$, and $n_{H_2O}(400 \text{ nm}) = 1.34$. The dotted (dashed) line correspond to curves calculated for $\theta_1 = \theta_2 = 10°$ ($\theta_1 = \theta_2 = 80°$). The $\left| \chi_2^{(2)} \right| = 1$, $\left| \chi^{(3)'} \right| = -1$ values also take into account the Fresnel factors. $\left| \chi_2^{(2)} \right|$ and $\left| \chi^{(3)'} \right|$ were taken from published data of air-water interfaces.[93,157–159]

Figure 3.2 shows the magnitude of the correction term $f_3(\kappa, \Delta k_z) = \frac{\kappa}{\kappa - i\Delta k_z}$ for a collinear ($k_1 = k_2$) SHG reflection experiment (right axis) using $\lambda_1 = \lambda_2 = 800$ nm, $\theta_{1,2} = \theta_0 = 45°$, $\left| \chi_s^{(2)} \right| = 1$, and $\left| \chi^{(3)'} \right| = -1$, which are values close to derived numbers from published experiments.[93,157–159] Since Φ_0 typically depends on the ionic strength, we use for illustration purposes only[67] $\Phi_0 = \frac{2k_B T}{e} \sinh^{-1}\left(\sigma / \sqrt{8000 k_B T N_{Av} c \epsilon_0 \epsilon_r} \right)$ for a 1:1 elec-

trolyte with a surface charge density σ= -0.05 Cm^{-2}. For $c > 10^{-3}$ M, $\kappa^{-1} \gg \Delta k_z^{-1}$ and $f_3(\kappa, \Delta k_z)$ approaches the value 1, in agreement with Eq. (3.4).[95] Figure 3.2 also displays the calculated emitted SHG intensity (left axis) considering three relevant functions:

1. the potential independent $\chi_s^{(2)}$ intensity according to Eqs. (3.1) and (3.10a) (blue line),

2. the intensity originating from both the $\chi_s^{(2)}$ and $\chi^{(3)'}$ contribution according to Eqs. (3.1) and (3.10a) (green line), and

3. the intensity originating from both the $\chi_s^{(2)}$ and $\chi^{(3)'}$ contribution excited with optical fields that vary along the z-direction (Eq. (3.10b).

For the calculation of the SH intensity, we approximated $\chi_s^{(2)}$ from Refs. [93, 157–159], which deal with nonresonant SHG from air/water interfaces. The $\chi_s^{(2)}$ contribution (blue line) to the total intensity, which neglects possible electrostatic field induced reorientation of interfacial water molecules, does not depend on the ionic strength as it does not depend on Φ_0. The combined z-independent $\chi_s^{(2)}$ and $\chi^{(3)'}$ contribution (green line) strongly depends on the ionic strength and keeps increasing as the ionic strength is lowered. When we consider the z-dependence of all fields (Eq. 9b, red line), the intensity does not increase below $\sim 10^{-3}$ M, but drops back to the level of the $\chi_s^{(2)}$-only contribution.

      Probing depth. We can explain the trend of the red line in Fig. 3.2 considering the following effects: At ionic strengths $> 10^{-1}$ M, $\chi_s^{(2)}$ is mainly responsible for the SHG signal as $4\kappa^{-1}$ involves only a few layers of water molecules, and the effect of reorientation by an electrostatic field is generally smaller than other effects.[160] Decreasing the ionic strength from 10^{-1} to 10^{-3} M, the electrostatic field affects more water molecules by penetrating deeper into the bulk (up to a distance of $4\kappa^{-1} \simeq 36$ nm, involving ~ 120 layers of water molecules). This increase in probing depth increases the SHG signal (by $\sim 35\%$ for the case of susceptibility elements with equal magnitudes plotted in Fig. 3.2.[146] Between 10^{-3} and 10^{-4} M, $4\kappa^{-1} \simeq \pi\Delta k_z^{-1}$. Below 10^{-4} M, $4\kappa^{-1} \gg \pi\Delta k_z^{-1}$. SHG photons are generated at different z-planes within the $4\kappa^{-1}$ region, that may extend up to ~ 4000 nm at 10^{-7} M, involving 13000 'layers' of water molecules. The interferences of the reflected SHG photons generated at the different planes is, however, destructive and reduces the SHG intensity even though the probing depth is increased. Once $\kappa^{-1} \gg \Delta k_z^{-1}$ (or $\kappa \ll \Delta k_z$), there is complete destructive interference and there remains only the $\chi_s^{(2)}$ contribution to the intensity. Thus, although the probing depth may be very deep, the destructive nature of the interference brings back the interfacial specificity. We will see that this is a purely geometrical effect when we consider transmission experiments and scattering experiments from a particle.

Comparison to existing literature. The above mentioned analysis has significant consequences for the interfacial description. Many SFG studies that aimed at probing the EDL as a function of ionic strength or pH (see e.g. the overviews of Refs. [161–164]) generally employ only the framework of Eqs. (3.4) and (3.10a). These studies often report that adding an electrolyte (or changing the pH) causes a big increase in the intensity compared to an electrolyte-free condition. The authors interpret the different response to originate from a large free energy for ionic absorption. However, Fig. 3.2 shows that, if one relies on an interpretation that is based on Eqs. (3.4) and (3.10a), the expected ion induced change will be much larger than the change obtained by Eq. (3.10b). Actually, the green curve in Fig. 3.2 highlights the fact that increasing the ionic strength from 10^{-7} to 10^1 M results in a decrease in the intensity by a factor of 2. According to the red curve, however, the intensities at 10^{-7} and 10^1 M are approximately identical (although for different reasons). This effectively implies that, when we correct for interference, ions are not nearly as strongly surface specific as expected. The described behavior can very well explain the SHG intensity change observed by the Geiger lab[165] at the fused silica/water interface as a function of electrolyte concentration (NaCl). This study reports an electrolyte dependent intensity that closely resembles the red line in Fig. 3.2. Rather than requiring ion adsorption or surface modification at very low ionic strengths, the SH intensity reports on the interference between photons generated in the bulk of the diffuse EDL and the surface structure. Also, the dependence of the SFG intensity on ionic strength measured at the fused silica/water interface reported by the Hore lab[146] deviates strongly from the behavior expected on the basis of Eq. (3.4). Instead of a sharply increasing intensity with low ionic strength, the data levels off at ionic strengths < 0.7 mM and shows similarities to the data in Fig. 3.2. Although the interpretation here is similar to the interpretation of Ref. [146] for c > 10^{-3} M, it is different for c < 10^{-3} M: The probing depth is not limited by the coherence length. Rather, in the case of a decaying electrostatic field, $\chi^{(3)'}$ is z-dependent and will continue contributing over distances beyond the coherence length. The z-dependence effectively increases the $\chi^{(3)'}$ contribution and would modifiy the presented solution in Ref. [146] with one that does not require a concentration dependence of the bulk $\beta^{(3)}$ or $\beta^{(2)}$ term and a smaller adjustment in the $\chi_s^{(2)}$ contribution. It is also worth noting that a correction in the charge density may have been needed as we took this value from the literature and did not measure it.

Another set of studies in Refs. [144, 166, 167] reports on an increase in the resonant SFG intensity as a function of increasing pH on the octadecyltrichlorosilane (OTS)/water interface[144,167] and the PDMS/water interface.[166] The authors[144] concluded that hydroxide ions have unusually high surface affinities for hydrophobic interfaces because they observed an increase in intensity. Based on this interpretation,

they calculated a free energy of absorption of 45 kJ/mol (18 kT). Changing the pH from 7 to 14[166] or 11,[144] the SFG intensity peaks at pH 10/11, i.e. at an ionic strength of $10^{-4}/10^{-3}$ M. This peak corresponds to the trend plotted in Fig. 3.2. It is therefore probably more meaningful to explain the strong pH dependence as mainly originating from interference, instead of by the adsorption of OH⁻ ions. In favor for the here presented interference interpetation are two other arguments: First, many experimental and theoretical studies have considered the possible surface propensity of hydroxide ions; the majority of these studies did not find a large surface affinity of OH⁻ ions (reviewed in Ref. [168]). Second, Tian *et al.*[144] report in the same work a similar trend also for NaCl (although this is limited only to ionic strengths up to ~ 30 μM, which would correspond to a pH of ~9.5).

The underlying concept and idea to the here presented derivations were present in an internal report of the laboratory already in 2009.[169] Some of the ideas that led to the exact analytical expressions as stated in here appeared in part since then.[170,171] However, these concepts were mainly dismissed in literature and unfortunately not considered in the interpretation of most of the data. The full description, as given in here,[155] was recently applied to verify the phase relationships of only the aqueous phase with the orientation of the α-quartz surfaces using reflection SHG.[172]

3.2.2 SHG/ SFG in transmission mode

Next, we consider briefly the case for a transmission mode geometry. The treatment for SHG and SFG in transmission geometry follows closely the one in reflection geometry, and Eqs. (3.1)- (3.10b) are still valid. The fundamental difference is in the expression for Δk_z. In transmission geometry and away from resonances

$$\Delta k_z = |\boldsymbol{k}_1 z + \boldsymbol{k}_2 z - \boldsymbol{k}_0 z| = k_{1z} + k_{2z} - k_{0z}, \tag{3.11}$$

which returns bigger values for Δk_z^{-1} compared to the reflection geometry in Eq. (3.5). Using for the transmission geometry the same incident parameters as for the reflection geometry - namely, a collinear illumination ($\boldsymbol{k}_1 = \boldsymbol{k}_2$) with $\lambda_1 = \lambda_2 = 800$ nm, $\theta_{1,2} = 45°$, $n_{H_2O}(800$ nm)=1.33, and n_{H_2O} (400 nm)=1.34 - we obtain $\Delta k_z^{-1} \cong 5.4$ μm. Hence, using transmission geometry and a 1:1 electrolyte we would theoretically need an ionic strength $c < 1.7 \times 10^{-12}$ M in order to have $4\kappa^{-1} > \pi \Delta k_z^{-1}$. This means that in the whole experimentally accesible range $\left| f_3(\kappa, \Delta k_z) \right|$ tends to be unity. In other words, Eq. (3.4) provides a good description of SHG/ SFG in transmission geometry at any ionic strengths. For a direct comparison, Fig. 3.3 shows both $\left| f_3(\kappa, \Delta k_z) \right|$ contributions as calculated in transmission geometry (left axis) as well as in reflection geometry (right axis,same as Fig. 3.2) as a function of the ionic strength. The two sketches below the graph indicate the main difference between the two geometries and the resulting Δk_z depending on the point of observation (compare Eqs. (3.11) and (3.5)). Note, though,

that we are not aware of anyone ever conducting transmission experiments.
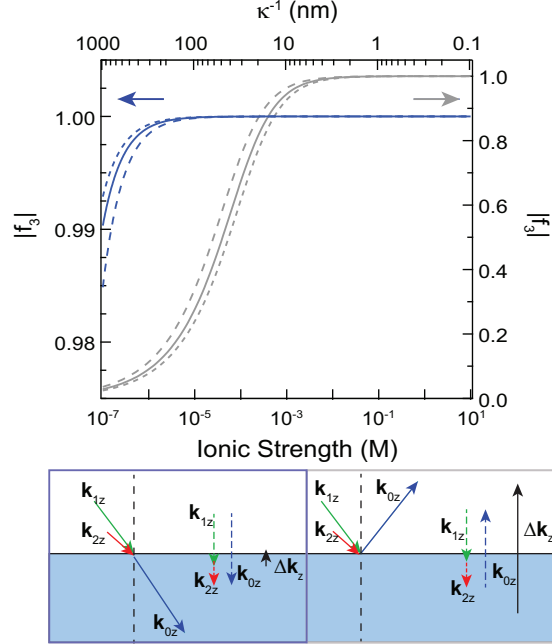
Figure 3.3: $\left|f_3(\kappa, \Delta k_z)\right|$ in transmission geometry (blue continuous curve, left axis) and reflection geometry (gray continuous curve, right axis), as a function of ionic strength. We used the following input values: $\theta_1 = \theta_2 = 45°$, $\lambda_1 = \lambda_2 = 800$ nm, $n_{air} = 1$, $n_{H_2O}(800\,\text{nm}) = 1.33$, and $n_{H_2O}(400\,\text{nm}) = 1.34$. The dotted (dashed) line corresponds to curves calculated for $\theta_1 = \theta_2 = 10°$ ($\theta_1 = \theta_2 = 80°$). The sketches highlight the different coherence length for transmission and reflection geometry and the therefore affected impact of the f_3 contribution.

3.2.3 SHG/ SFG in scattering mode

Theoretical background. The previous considerations are equally important for the analysis of the EDL of particles, droplets, vesicles and other colloids in aqueous solution. We start with developing the formalism to describe SFS and SHS. We anticipate that a different geometry will lead to expressions that differ from the ones derived for transmission and reflection geometry (Eqs. (3.9) and (3.10b)). Figure 3.4 shows the top view of a SF scattering experiment. Here θ is the scattering angle, which is the angle between the wave vector of the scattered (detected) light, $\mathbf{k}_0$, and the sum of the incoming wavevectors $\mathbf{k}_1$ and $\mathbf{k}_2$. Figure 3.4a also displays the definition of the opening angles α and β for the two incoming beams.

The scattering wave vector q is defined as $\mathbf{q} \equiv \mathbf{k}_0 - (\mathbf{k}_1 + \mathbf{k}_2)$. For collinear SHS, $\mathbf{k}_1 = \mathbf{k}_2$ and $\omega_1 = \omega_2$. As shown previously,[101,152] in absence of surface charges, the
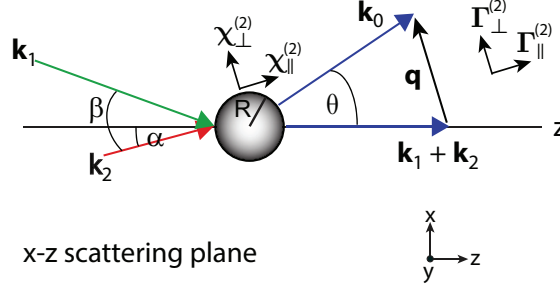
Figure 3.4: Sketch of the SFS/SHS scattering geometry, top view. P polarized light oscillates in the x-z (scattering) plane, whereas S polarized light oscillates in the y direction.

scattered SH intensity is given by

$$I(\omega_0) = 2n(\omega_0)\sqrt{\frac{\epsilon_0}{\mu_0}}|\mathbf{E}(\omega_0)|^2 \tag{3.12}$$

in which $n(\omega_0), \epsilon_0, \mu_0$ are the refractive index, vacuum permittivity and permeability, respectively. The amplitude of the scattered SF/SH field $E_{ijk}(\omega_0)$ from a sphere can be expressed as[100]

$$E_{\text{ppp}}(\omega_0) = \frac{ick_0^2}{2\pi|\hat{r}||\hat{I}|}\frac{e^{ik_0r_0}}{r_0}E_1(\omega_1)E_2(\omega_2)$$

$$\left[\cos\left(\frac{\theta}{2}\right)\cos\left(\frac{\theta}{2}-\alpha\right)\cos\left(\frac{\theta}{2}-\alpha+\beta\right)\Gamma_1^{(2)}\right.$$

$$\left.+\cos\left(\theta-\alpha+\beta\right)E_{ssp}+\cos\left(\theta-\alpha\right)E_{sps}+\cos\left(\beta\right)E_{pss}\right]$$

$$E_{\text{ssp}}(\omega_0) = \frac{ick_0^2}{2\pi|\hat{r}||\hat{I}|}\frac{e^{ik_0r_0}}{r_0}E_1(\omega_1)E_2(\omega_2)\cos\left(\frac{\theta}{2}-\alpha\right)\Gamma_2^{(2)} \tag{3.13}$$

$$E_{\text{sps}}(\omega_0) = \frac{ick_0^2}{2\pi|\hat{r}||\hat{I}|}\frac{e^{ik_0r_0}}{r_0}E_1(\omega_1)E_2(\omega_2)\cos\left(\frac{\theta}{2}-\alpha+\beta\right)\Gamma_3^{(2)}$$

$$E_{\text{pss}}(\omega_0) = \frac{ick_0^2}{2\pi|\hat{r}||\hat{I}|}\frac{e^{ik_0r_0}}{r_0}E_1(\omega_1)E_2(\omega_2)\cos\left(\frac{\theta}{2}\right)\Gamma_4^{(2)}$$

in which i, j, k refer to the polarization state (S or P, see 2.1.1 for a definition) of the SF, visible and IR beams, respectively. The product $|\hat{r}||\hat{I}|$ is a unit vector product of a distance and current and is needed to preserve the (S.I.)-units of Eq. (3.13). c is the speed of light. $\mathbf{\Gamma}^{(2)}$ is the effective particle surface second-order susceptibility, which is defined as $\Gamma_{ijk}^{(2)} = \sum_{abc}\int^\Omega T_{ia}T_{jb}T_{kc}\chi_{s,abc}^{(2)}e^{i\mathbf{q}\cdot\mathbf{r}}d\Omega$. Here, $\mathbf{r}$ is a point on the particle surface and the integration is performed over the entire surface Ω of the particle. $\mathbf{\Gamma}^{(2)}$ thus captures the combined symmetry of the spherical scatterer and interacting

electromagnetic fields. The defintion of $\Gamma_i^{(2)}$, with i=1-4 is

$$\Gamma_1^{(2)} = \Gamma_{\perp\perp\perp}^{(2)} - \Gamma_{\|\|\perp}^{(2)} - \Gamma_{\|\perp\|}^{(2)} - \Gamma_{\perp\|\|}^{(2)},$$
$$\Gamma_2^{(2)} = \Gamma_{\|\|\perp}^{(2)},$$
$$\Gamma_3^{(2)} = \Gamma_{\|\perp\|}^{(2)}, \text{ and}$$
$$\Gamma_4^{(2)} = \Gamma_{\perp\|\|}^{(2)}.$$

The index $\perp$ ($\|$) refers to the direction perpendicular (parallel) to $\mathbf{q}$. For non-chiral surfaces, the effective susceptibility $\mathbf{\Gamma}^{(2)}$ is related to the surface susceptibility $\chi_s^{(2)}$ by the following transformation

$$
\begin{pmatrix} \Gamma_1^{(2)} \\ \Gamma_2^{(2)} \\ \Gamma_3^{(2)} \\ \Gamma_4^{(2)} \end{pmatrix} =
\begin{pmatrix} 2F_1 - 5F_2 & 0 & 0 & 0 \\ F_2 & 2F_1 & 0 & 0 \\ F_2 & 0 & 2F_1 & 0 \\ F_2 & 0 & 0 & 2F_1 \end{pmatrix}
\begin{pmatrix} \chi_{s,1}^{(2)} \\ \chi_{s,2}^{(2)} \\ \chi_{s,3}^{(2)} \\ \chi_{s,4}^{(2)} \end{pmatrix}
\tag{3.14}
$$

with[24,101,173]

$$F_1(qR) = 2\pi R^2 i \left(\frac{\sin(qR)}{(qR)^2} - \frac{\cos(qR)}{qR} \right), \text{ and}$$
$$F_2(qR) = 4\pi R^2 i \left(3\frac{\sin(qR)}{(qR)^4} - 3\frac{\cos(qR)}{(qR)^3} - \frac{\sin(qR)}{(qR)^2} \right).$$

Also $q = |\mathbf{q}|$, and R is the radius of the spherical particle, and $\chi_{s,1}^{(2)} = \chi_{\perp\perp\perp}^{(2)} - \chi_{\|\|\perp}^{(2)} - \chi_{\|\perp\|}^{(2)} - \chi_{\perp\|\|}^{(2)}, \chi_{s,2}^{(2)} = \chi_{\|\|\perp}^{(2)}, \chi_{s,3}^{(2)} = \chi_{\|\perp\|}^{(2)}$, and $\chi_{s,4}^{(2)} = \chi_{\perp\|\|}^{(2)}$, in which $\perp$ ($\|$) refers to the direction perpendicular (parallel) to the particle surface.

In the presence of an electrostatic field one needs to modifiy these expressions,[100] similarly to what we did in the previous sections for planar interfaces. This is done by replacing $\mathbf{\Gamma}^{(2)}$ with $\mathbf{\Gamma}^{(2)} + \mathbf{\Gamma}^{(3)'}$ with $\mathbf{\Gamma}^{(3)'}$, the third-order effective particle susceptibility, defined as[100]

$$\Gamma_n^{(3)'} = \sum_{abc} \int_\Omega \int_R^{+\infty} T_{ia} T_{jb} T_{kc} \chi_n^{(3)'} E_{dc}(r) e^{i\mathbf{q}\cdot\mathbf{r}} dr d\Omega$$
$$= \int_R^{+\infty} E_{dc}(r) \Gamma_n^{(3)}(r) dr
\tag{3.15}$$

in which $\Gamma_n^{(3)}(r) = 2F_1(qr)\chi_n^{(3)'}, (n = 2,3,4)$ with $\chi_n^{(3)'}$ being defined as in the case of planar interfaces. This simplification is possible, because $E_{dc}(r)$ always points along the radial direction and the integral over the angular range $\mathbf{\Omega}$ is identical to that for

$\mathbf{\Gamma}^{(2)}$. Eq. 3.15 reduces to the same linear combination as reported in Eq. 3.14. However, because of symmetry properties $\chi_1^{(3)'} = \chi_{\perp\perp\perp,\perp}^{(3)'} - \chi_{\parallel\parallel\perp,\perp}^{(3)'} - \chi_{\parallel\perp,\parallel,\perp}^{(3)'} - \chi_{\perp\parallel\parallel,\perp}^{(3)'} = 0$, and thus $\Gamma_1^{(3)'} = 0$. With $E_{dc}(r) = -\frac{d}{dr}\Phi(r)$, Eq. 3.15 becomes

$$\Gamma_n^{(3)'} = -\int_R^{+\infty} \frac{d\Phi(r)}{dr}\Gamma_n^{(3)}(r)dr \tag{3.16}$$

For ionic strengths $> 10^{-3}$ M, similar to the case of planar interfaces (3.1b), $E_{dc}(r)$ decays much faster than the period over which $\Gamma_n^{(3)}(r)$ varies, and thus, $\Gamma_n^{(3)}$ can be considered constant and equal to $\Gamma_n^{(3)}(R)$. Eq. 3.16 results then in

$$\Gamma_n^{(3)'} = \Phi_0\Gamma_n^{(3)}(R) = 2F_1(qR)\Phi_0\chi_n^{(3)'} \tag{3.17}$$

with Φ_0 the surface potential, in agreement with Ref. [100].

Interference and the diffuse EDL around particles. For ionic strengths $< 10^{-3}$ M, we can think of the particle as being surrounded by a soft shell of weakly oriented water (the diffuse EDL, DDL) with a thickness $4\kappa^{-1}$. Over this distance, we must consider $\Gamma_n^{(3)}(r)$ as being dependent of r. Then Eq. 3.16 reads as

$$\begin{aligned}\Gamma_n^{(3)'} &= -\int_R^{+\infty} \frac{d\Phi(r)}{dr}\Gamma_n^{(3)}(r)dr \\ &= 2F_1(qR)\Phi_0\chi_n^{(3)'} + 2\chi_n^{(3)'}\int_R^{+\infty} \frac{dF_1(qr)}{dr}\Phi(r)dr.\end{aligned} \tag{3.18}$$

The second term now represents the contribution that originates from the DDL. As with Eq. 3.8, the second part of Eq. 3.18 only contributes to the expression several nanometers away from the interface. Therefore implementing here a Stern layer would also not result in different scattering values. In addition, it is insensitive to a change in the interfacial (Stern) dielectric constant (as suggested by **??**) Thus, we can use the mean-field expression for the DDL[127] $\Phi(r) = \Phi_0\frac{R}{r}e^{-\kappa(r-R)}$, with $\Phi_0 = \Phi(R)$, and obtain

$$\begin{aligned}\Gamma_n^{(3)'} &= 2\Phi_0\chi_n^{(3)'}\left(F_1(qR) + F_3(\kappa R, qR)\right), \\ \text{with } F_3(\kappa R, qR) &= 2\pi R^2 i\frac{qR\cos(qR) + \kappa R\sin(qR)}{(qR)^2 + (\kappa R)^2},\end{aligned} \tag{3.19}$$

which depends on the particle radius R, the Debye length κ^{-1}, and the scattering wave vector modulus q.

In the case of high ionic strength, we have

$$\kappa^{-1} \to 0 \text{ and } F_3(\kappa R, qR) \to 0, \text{ in agreement with Eq. 3.17.}^{[100]}$$

For low ionic strength, we have

$$\kappa \to 0, \text{ and } F_3(\kappa R, qR) \to 2\pi R^2 i \frac{\cos(qR)}{qR}.$$
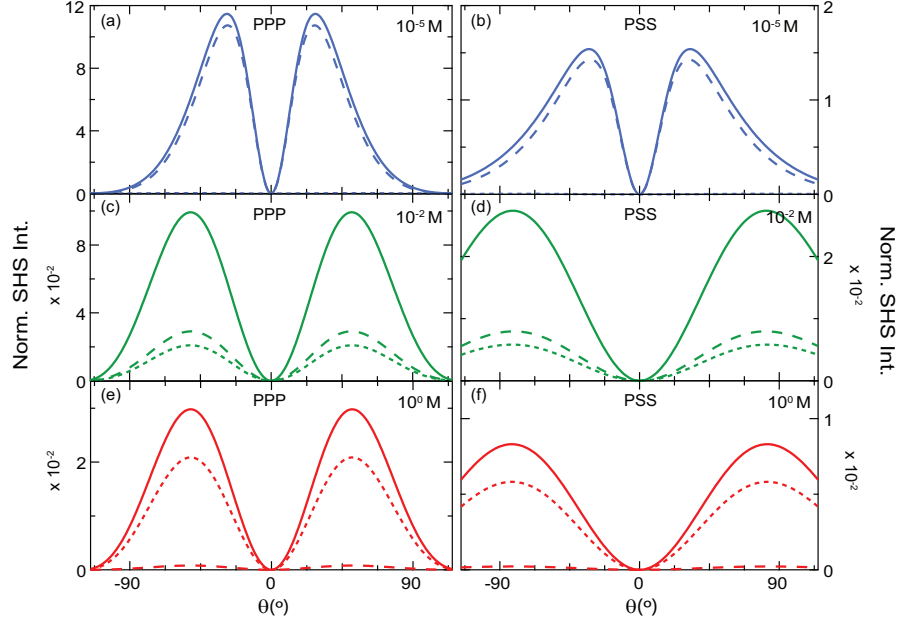
Figure 3.5: (a-f) Scattering patterns: (a, c, e) PPP and (b, d, f) PSS polarization combinations, calculated for a particle with R= 50 nm; (a, b) ionic strength of 10^{-5} M and $\Phi_0 = -286$ mV; (c, d) ionic strength of 10^{-2} M and $\Phi_0 = -109$ mV; (e, f) ionic strength of 1 M and $\Phi_0 = -21$ mV. Continuous lines are calculated assuming $\chi_{s,1}^{(2)} = 0$, $\chi_{s,2}^{(2)} = \chi_{s,3}^{(2)} = \chi_{s,4}^{(2)}$, $\chi_2^{(3)'} = \chi_3^{(3)'} = \chi_4^{(3)'}$, and $\chi_{s,2}^{(2)}/\chi_2^{(3)'} = -0.11$. The intensities originating from a pure surface response, $\chi^{(3)'} = 0$, and pure bulk response, $\chi_s^{(2)} = 0$, are displayed as dotted and dashed lines, respectively. The pure surface response (dotted lines) is the same for the same polarization combination independently from the ionic strength and surface potential.

This change in the F_3 term becomes apparent in the shape of the scattering pattern and is solely available in scattering experiments, but not in the reflection and transmission mode experiments from planar interfaces. Hence, such a specific behavior offers an opportunity to gain experimentally access to the EDL. To demonstrate the effect of the $F_3(\kappa R, qR)$ term on SHS for different ionic strengths, we calculated SHS patterns for a spherical particle (R=50 nm) in an aqueous solution containing either 10^{-5}, 10^{-2}, or 1 M of a 1:1 electrolyte as shown in Fig. 3.5. For illustration purposes only, we calculated Φ_0 using[67,127]

$$\sigma = \sqrt{(8000 k_B T N_{Av} c \epsilon_0 \epsilon_r} \left[\sinh \frac{e\Phi_0}{2k_B T} + \frac{1}{eR} \sqrt{\frac{2k_B T \epsilon_0 \epsilon_r}{1000c}} \tanh \frac{e\Phi_0}{4k_B T} \right]$$

and assuming a surface charge density σ_0= -0.05 Cm^{-2}(the same as used for Fig. 3.2). The solid lines show the resulting intensity scattering patterns (using the above equations and $\mathbf{\Gamma}^{(3)'}$ from Eq. 3.19, while the dotted and dashed lines represent the surface response ($\boldsymbol{\chi}^{(3)'} = 0$) and the bulk response ($\boldsymbol{\chi}_s^{(2)} = 0$), respectively. The computed patterns for the individual contributions do not add up, because we plot the intensities of the pure bulk and pure surface contribution omitting the cross product. The DDL contribution dominates for 10^{-5} M (Fig. 3.5, b). The intensity is much reduced for an ionic strength of 10^{-2} M (Fig. 3.5c, d), and almost completely absent at 1 M (Fig. 3.5e, f). There is thus a significant contribution from the DDL to the SHS pattern for ionic strength < 10^{-3} M. In a scattering experiment, the $F_3(\kappa R, qR)$ contribution perturbs the $\boldsymbol{\chi}^{(3)'}$ contribution, adds constructively to the $\boldsymbol{\chi}^{(2)}$ contribution, and thus significantly alters the shape of the scattering pattern. Specifically, the peak shape of scattered light is severely distorted towards forward scattering angles and the shape change varies distinctively in different polarization combinations. This characteristic peak shape and polarization dependence should therefore be visible in particle/-droplet dispersions at low ionic strength. We will test the developed theory and the impact of the contributions using angle- and polarization-resolved SHS experiments in the next chapter.

3.2.4 Comparison between reflection, transmission, and scattering experiments

Comparing differences between scattering and reflection/ transmission experiments, we can make the following observations:

1. For a proper description, scattering and reflection/transmission experiments require completely different sets of equations that reflect the different optical processes occuring in the different systems. These equations are solutions to the Maxwell equations that depend on the geometry and topology of the light-matter interaction process. Just like in linear scattering and reflection/transmission experiments where the former is, e.g. described by Rayleigh-scattering or Mie-scattering, and the latter is described by the Fresnel factors, each process needs to be described with the physical expressions that report the right type of light-matter interactions. Therefore, it is not meaningful to describe nonlinear optical scattering processes in intensity versus ionic strength series by Eq. 3.4 (or Eq. 3.10b).

2. There is a distinct difference in ionic strength dependence. To illustrate this, we compare the concentration dependence by examining $\left| f_3(\kappa, \Delta k_z) \right|$ in reflection geometry (Fig. 3.3) and $\left| F_3(\kappa R, qR) \right| / (4\pi R^2)$ for a particle with R= 50 nm in scattering geometry (Fig. 3.6). Note that there is no polarization dependence

yet. While $\left|f_3(\kappa, \Delta k_z)\right|$ is small for $c < 10^{-3}$ M, and increases with higher ionic strengths, $\left|F_3(\kappa R, qR)\right|/(4\pi R^2)$ is large for $c < 10^{-3}$ M and vanishes at higher ionic strengths. In the range of ionic strength from 10^{-7} M to 10^{-3} M, the reflected intensity increases with increasing ionic strength, wheras the scattering intensity decreases. A more important difference, however, originates from the dependence on the scattering angle. Figure 3.6 shows $\left|F_3(\kappa R, qR)\right|/(4\pi R^2)$ for scattering angles of 10°, 45°, and 80°. The magnitude of $\left|F_3(\kappa R, qR)\right|/(4\pi R^2)$ starting at low ionic strength either continuously decreases with increasing ionic strength (10°), or remains relatively steady and then decreases (45°), or increases to a maximum and then decreases (80°). This behavior translates directly into an intensity dependence that would qualitatively follow reported trends detected at different angles.

3. Different polarization combinations result in different scattering pattern shapes. This offers an opportunity for a more extensive characterization of the EDL than what is possible at planar interfaces.

4. As shown in the simulation in Fig. 3.5 the angle- and polarization-resolved data represent a way to determine surface properties in a very accurate manner. As pointed out already elsewhere,[119] measuring SHS in the forward direction is not the optimal way of gathering SHS light that exclusively originates from the surface.
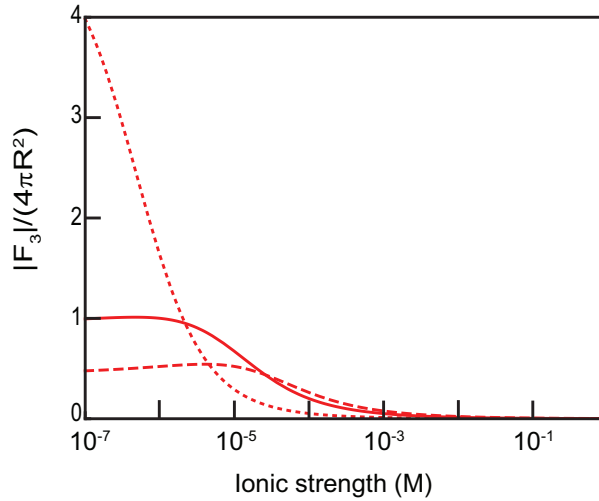
Figure 3.6: $\left|F_3(\kappa R, qR)\right|/(4\pi R^2)$ for a scattering geometry calculated as a function of ionic strength c. We used the following parameters: $\theta = 45°$, $\lambda_1 = \lambda_2 = 1028$ nm, $n_{air} = 1$, $n_{H_2O}(1028 \text{ nm}) = 1.33$, and $n_{H_2O}(514 \text{ nm}) = 1.33$, and $R = 50$ nm. The continous, dotted, and dashed lines correspond to curves calculated at scattering angles $\theta = 45°$, 10°, and 80°, respectively.

A commonly employed procedure to examine the surface of particles in solution is to record the SHG intensity in the forward direction. The choice of the detection angle and the polarization combination are not important parameters for reflection/transmission mode experiments. For this reason, it was most likely considered to be not relevant for the measurements and description of particle interfaces.[103,139,150,174,175] In these cited experiments, the SHG intensity trend typically shows a continously decreasing slope with ionic strength that is then described by Eq. 3.4 using the Gouy-Chapman model (or variations thereof). Although one can derive values for a surface potential and the charge density in this way, the description of the data uses the solution for a different, unrelated problem. Hence, the solutions are physically not meaningful.
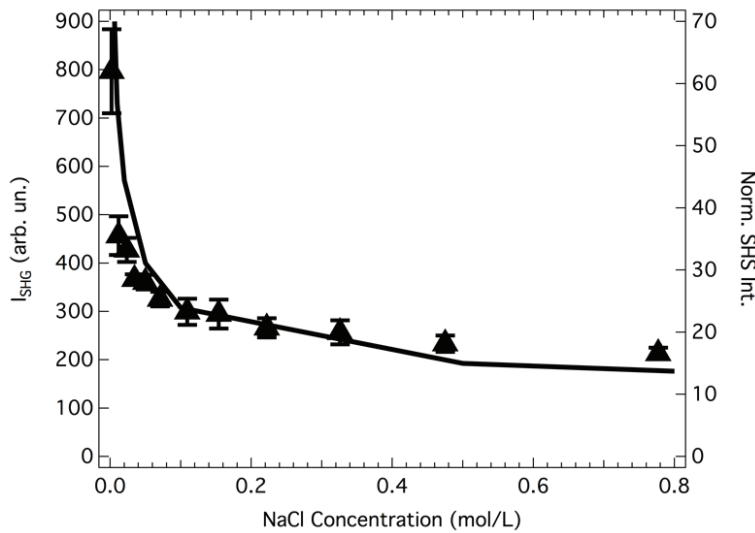
Figure 3.7: Data (triangles) reprinted with permission from Fig. 6 of Ref. [174]: SH intensity as a function of NaCl concentration. For a better visibility, the solid line connects calculated solutions using the Eqs. 3.12, 3.13 and 3.19. As parameters for the calculation, we used $R = 500\text{nm}, \lambda = 800\text{nm}, n_{\text{air}} = 1, n_{\text{H}_2\text{O}} = 1.33, n_{\text{SiO}_2} = 1.43$, and assuming a collection angle of 40° in forward direction.

We can also show via another argumentation that the obtained surface potential values are rather ambiguous. The computation values for $\left|F_3(\kappa R, qR)\right|/(4\pi R^2)$ in

Fig. 3.6 are approximately proportional to the square root of the intensity ($\sqrt{I}$). The slope of the curves shows that the same particle dispersion can result in a different $\sqrt{I}$ versus c curve simply by selecting a different scattering angle (in the case of Fig. 3.6, $\theta = 10°$, 45°, and 80°). If the angle of acceptance for the detected SHS light or the central scattering angle had been different, a fit with Eq. 3.4 would have returned a different result for the surface potential (from the same particles).

To further illustrate the strength of our model, we have calculated the expected intensity versus concentration behavior for one of the data sets of particles in solution from literature (Fig. 6 of Ref. [174]). Figure 3.7 shows this dataset of silica particles together with a theoretical evaluation using Eqs. 3.12, 3.13 and 3.19. Assuming that the data in Ref. [174] has been obtained in the PPP polarization combination, there is a good agreement between the experimental data and the calculated trend using our model. This supports the conclusion that at low ionic strength the electric field penetrates deep into the bulk water.

3.3 Conclusions

In summary, we have theoretically described SFG/ SHG responses in reflection, transmission and scattering mode explicitly considering the effects of low and high ionic strength on the emitted light. If an electrostatic field is present in the interfacial region, it will contribute to the intensity. For low ionic strengths ($< 10^{-3}$ M) the DDL can lead to significant distortions to the emitted light (compared to the case of higher ionic strengths) because of an interference between SHG/ SFG photons that are generated at different positions within the DDL. For reflection and scattering mode experiments in typical experimental conditions, this interference can give rise to a probing depth up to ~1 μm instead of being restricted to a region smaller than 1 nm. The described effect significantly modifies the interpretation of ion dependent SHG/ SFG data. SHG and SFG scattering measurements report on the same phenomenon as their planar geometry counterparts, but contain a broader range of parameters that can be varied (scattering angle, particle size, polarization state of the light). In scattering experiments, the DDL takes the shape of a soft shell that not only produces a change in the scattered intensity but also significantly distorts the angle-resolved scattering patterns. The presented description is only relevant as the main aqueous phase is probed, i.e. for vibrational SFG experiments that center on the O-H stretch or bending mode (as reviewed in Ref. [121]), resonant SHG experiments that focus on the charge transfer to solvent mode as long as the water is also resonantly excited (e.g. Ref. [176]), and nonresonant SHG measurements that probe the response of all noncentrosymmetric molecules in the sample(e.g. Refs. [139, 177–179]). Given the interest and relevance of the electrostatic properties of interfaces and the need to characterize their properties,[67] our results are of great value for determining the structure and

properties of the EDL at aqueous interfaces. For SHS and SFS, the resulting scattering patterns are very sensitive to the shape of the additional form factor $F_3(\kappa R, qR)$. This opens up future avenues for determining the surface potential without assumptions about the structure and properties of the EDL, as we will see in the next chapter.

4 Optical label-free and model-free probe of the surface potential of nanoscale and microscopic objects in aqueous solution

The electrostatic environment of aqueous systems is an essential ingredient for the function of any living system. To understand the electrostatic properties and their molecular foundation in soft, living, and three-dimensional systems, we developed a table-top model-free method to determine the surface potential of nano- and microscopic objects in aqueous solutions. Angle-resolved nonresonant second harmonic scattering measurements (AR-SHS) contain enough information to determine the surface potential unambiguously, without making assumptions on the structure of the interfacial region. The scattered second harmonic (SH) light that is emitted from both the spherical particle interface and the diffuse double layer can be detected in two different polarization states that have independent scattering patterns. The angular shape and intensity are determined by the surface potential and the second-order surface susceptibility. Calibrating the response with the SH intensity of bulk water, a single, unique surface potential value can be extracted.

First, we demonstrate the validity of the previously described equations and contributions using hexanol stabilized droplets and binary mixed liposomes of dioleoylphosphatidylcholine (DOPC) and dioleoylphosphatidylserine (DOPS) in three different electrolyte solutions. Following this, we apply the method to 150 nm bare oil droplets in water and to ~100 nm zwitterionic or anionic liposomes at various ionic strengths to extract the surface potential.

4.1 Introduction

The electrostatic potential of interfaces drives diverse processes such as self-assembly,[180,181] transport,[182,183] chemical reactions,[184,185] electrochemical processes,[186,187] and many other phenomena in biology and chemistry. The surface potential affects the stability of nanoparticles, nanoemulsions, micelles,[58,188] and their electrochemical reactivity. The surface potential participates also in membrane / liposome fusion. What all of these systems and processes have in common, is, that they are composed of nanoscopic or micron-sized structures in aqueous solution. It is the aim here to provide a label- and interface model-free, optical method to determine the surface potential of such particles in aqueous solution. It is generally a complex task to obtain a (surface) potential from a planar macroscopic electrode, because it typically involves measuring an electric current and/or charge distribution that one needs to attribute to a variety of different sources.[67] For a solution of small particles, such measurements are not possible and the situation is even more complex. Traditionally, for particle dispersions, one employs electrokinetic mobility measurements[66,135] that result in a ζ-potential. This quantity is commonly interpreted as the electrostatic potential at the 'slipping plane' of the diffuse double layer (DDL). The position of this hypothetical plane varies with electrolyte concentration and one thinks of it as a plane that is positioned up to a few nanometers away from the actual interfacial plane.[66,127,135] To estimate a value for the surface potential Φ_0 from the ζ-potential, the interfacial structure is described by a simplified mean field model, such as the (planar) Gouy-Chapman (GC) or the constant capacitor (CC) model.[127] The GC model relates Φ_0 to the surface charge density (σ_0) maintaining the electrolyte concentration as variable parameter. In this model, the interface appears as a uniformly charged surface surrounded by a continuous dielectric medium. The model considers ions as point charges that screen the electrostatic field from the interface, but it neglects hydration, changes in the water structure and the specific surface chemistry.

Spectroscopic measurements offer a way to access the surface potential more directly. Brown *et al.* recently proposed X-ray photoelectron spectroscopy measurements as a way to determine the surface potential of silica nanoparticles in highly concentrated solutions.[189] It is yet unclear, though, how applicable the method is in general, as all measurements to date have been performed at synchrotron facilities that have a superior brilliance over table-top sources.[a] Nonresonant SHS is an optical process that can probe the net orientational order of water molecules along the surface normal (Ref. [152] and references therein). This method is thus sensitive to the orientational directionality of water molecules in the interfacial region defined as the region from the surface plane to the position where the field has decayed to zero.[155] Angle-resolved (AR) nonresonant SHS[106] is applicable to a wide variety of

---

[a]Private communication with Dr. M. Brown.

hard[118,174,175,190,191] and soft particles systems[104,178,192], and can be used in very dilute solutions and small sample volumes. In absence of chemical effects, the measured intensity depends quadratically on the surface potential.[100] In practice, one, who aims to extract the surface potential from a nonresonant SHS experiment, applies the following "Eisenthal-$\chi^{(3)}$" method:[103] The SH intensity scattered by particles in solutions is measured at a fixed scattering angle as a function of the ionic strength (c) of the solution in any (unspecified) polarization combination and subsequently fit with $\sqrt{I_{SH}} = \chi^2 + \chi^3 \Phi_0$. This now widely applied procedure[103,104,150,174,175] is very similar to the method applied to planar interfaces[93–95,141,161,193] using the same expressions (compare Eq. (3.4) in the previous chapter). However, by relying on a single equation to extract three parameters from an arbitrarily normalized data set, and neglecting the impact of ionic strength entirely, a unique solution for Φ_0 cannot be obtained as we have seen in the last chapter. In addition, the use of the GC model involuntary restricts the surface structure to the highly idealized composition as describe above and throws all molecular level information away, even though they are present in the data.[101,155]

In this chapter, we confirm experimentally the impact of the various contributions to the scattering patterns that were displayed in chapter 3. We then show that it is possible to obtain a unique solution for the surface potential of nanoscopic and microscopic particles in aqueous solution, without the need to invoke a model for the structure of the interfacial region. We utilize the entire angular scattering pattern in multiple polarization combinations and describe it with the nonlinear RGD theory. In doing so, we can express the necessary parameters to describe angle-resolved nonresonant SH measurements (AR-SHS) in absolute units by calibrating the measured intensity against the nonresonant SH response of water. The surface potential and one non-vanishing surface susceptibility tensor element are the only two independent parameters. The fit of the experimental data collected in two different polarization combinations results in unique values for the parameters because the two parameters are fitted with two independent equations. We apply this method to three different systems in aqueous solution: Nanoscopic oil droplets, zwitterionic liposomes, and anionic liposomes as a function of the solution's ionic strength. Finally, we compare the derived values with commonly applied models, such as the Gouy-Chapman model and the constant capacitor model.

4.2 Materials & Methods

4.2.1 Chemicals

Sulfuric acid (95-97 %, ISO, Merck), ammonium hydroxide (30 %, Sigma-Aldrich), hydrogen peroxide (30 %, Reactolab SA), chloroform (Emsure, ACS, ISO, Merck) and sodium chloride (NaCl, >99 %, Sigma-Aldrich), phosphorus standard solution (0.6

M, Sigma-Aldrich), L-ascorbic acid (ACS, $\geq$ 99 %, Sigma-Aldrich), ammonium molyb-date (VI, ACS, 81-83 %, Sigma-Aldrich), sodium hydroxide (99.99 %, Sigma-Aldrich), hexanol (>99.5 %, Sigma-Aldrich) and hexadecane (>99.8 %, Fluka) were used as received. 1,2-dioleoyl-*sn*-glycero-3-phosphocholine (DOPC) and 1,2-dioleoyl-*sn*-glycero-3-phospho-L-serine (sodium salt) (DOPS), were purchased in powder form (>99 %) from Avanti Polar Lipids (Alabama, USA) and stored at -20 °C until further use.

4.2.2 Cleaning procedures

Glassware was cleaned with a 1:3 H_2O_2:H_2SO_4 solution and rinsed with ultrapure water (Milli Q, Millipore, Inc., electrical resistance of 18.2 MΩ cm). The glassware for the phosphate assay required a two-step cleaning procedure: First a cleaning with a 3:1:1 H_2O:H_2SO_4:H_2O_2 solution at 100 °C was done, which was followed by a cleaning with a 3:1:1 H_2O:NH_4OH_4:H_2O_2 solution at 80 °C, each for 10 minutes. After and in between the cleaning steps the glassware was thoroughly rinsed with ultrapure water.

4.2.3 Sample preparation

Oil droplets. Nanodroplets were prepared in a similar fashion to the procedure de-scribed in Ref. [194]. For bare oil droplets, we mixed 2 vol. % hexadecane in slightly basic H_2O (adjusted with NaOH to pH=8.3) in a 4 ml glass vial and vortexed the liquid, followed by ultrasonication (35 kHz, 400 W, Bandelin) for 5 minutes. For hexanol stabilized droplets the procedure was almost the same: we mixed 2 vol. % hexadecane with 10 mM hexanol and ultrapure water in a 4 ml glass vial, stirred the liquid with an homogenizer for 5 minutes, follwed by ultrasonication for 5 minutes. The droplet size distribution was checked by dynamic light scattering (DLS) whereas the ζ-potential was derived from electrophoretic measurements (Zetasizer Nano ZS, Malvern) us-ing Smoluchowski's approximation. The bare droplets had a mean hydrodynamic diameter of ~170 nm with a polydispersity index (PDI) of ~0.2, whereas the hexanol stabilized droplets had a mean hydrodynamic diameter of ~150 nm also with a PDI of < 0.2. The ζ-potential was -34 ±7 mV peak value for bare oil dropelts and -38 ±8 mV for hexanol covered droplets. Values for size and ζ-potential are averages of 3 measurements. For SHS measurements, the emulsion was diluted with ultrapure water to 0.1 vol. % just before the measurement was started.

Liposomes. We prepared and characterized the liposomes according to the procedure given in section 2.2. The liposomes were found to have a mean diameter in the range of 94 - 110 nm with a polydispersity index (PDI) of less than 0.1. Liposome solutions were diluted with pure water just before the measurements. Samples containing NaCl were diluted with the respective salt solution prior to the SHS experiments and incu-bated for 30 min to reach equilibrium. The stability of these solutions was confirmed by DLS and ζ-potential measurements as well.

4.2.4 Angle-resolved (AR)-SHS measurements

For scattering patterns the acceptance angle was set to 3.4°. Patterns were obtained in steps of 5° from $\theta = -90°$ to $\theta = 90°$ with 0° being the forward direction of the fundamental beam. Data points were acquired using 20 x 1s or 1.5 s acquisition time with a PMT gate width of 10 ns. Single angle measurements were carried out at the angle of maximum intensity, $\theta = 50°$ with an acceptance angle of 11.4°. For single angle measurements acquisition time was 20x 1s, also with 10 ns gate width.

4.3 Results & Discussion

4.3.1 Physical contributions and origin of the signal for an AR-SHS experiment

The generated signal of aqueous dispersions in a label-free nonresonant AR-SHS experiment originates mainly from the water molecules. The interface disturbs the overall isotropic distribution of water molecules. This disturbance gives rise to scattered SH photons (1 in Fig. 4.1a). The quantity of scattered photons depends on the orientational average of the second-order hyperpolarizability tensor $\left(\boldsymbol{\beta}^{(2)}\right)$ elements of water. Computing these values over the entire interface of the scatterer results in values for the surface second-order susceptibility $\left(\chi_s^{(2)}\right)$ tensor elements of the interfacial water.[195,196] In addition to the perturbation in orientation because of an interface, an electrostatic field that originates from a surface charge distribution may generate a small amount of non-isotropically oriented water molecules that can also act as sources of SH photons (on the surface and in the double layer, 2, 3 in Fig. 4.1a). Lastly, isotropically oriented water molecules possess a third-order molecular hyperpolarizability tensor $\left(\boldsymbol{\beta}^{(3)}\right)$[92] that can also couple with the incoming optical fields and the electrostatic field to give rise to additional emitted SH photons (4 in Fig. 4.1a). This last contribution is only responsible for less than 1% of the emitted intensity.[197] These four contributions all depend linearly on the electrostatic field and contribute to an effective third-order susceptibility tensor, $\chi^{(3)'}$.[100] Considering these four effects, various dilute 'hydration shells' of very weakly oriented but correlated water molecules surrounding the particle contribute to the characteristic SHS pattern (Fig. 4.1b).[b] These layers contributing to the SH intensity consist of the interface and the entire DDL up to the distance at which the surface potential has decayed to zero. To illustrate this distance and its dependence on the ionic strength and particle radius R, we plot in Fig. 4.1c an exponentially decaying electrostatic potential emanating from a charged spherical nanoparticle with R=50 nm (using $\Phi(r) = \Phi_0 \frac{R}{r} e^{-\kappa(r-R)}$,[67]). Here, κ is the inverse of the Debye length, $\kappa^{-1} = \sqrt{(\epsilon_0 \epsilon_r k_B T)/(2000 e^2 z^2 N_{Av} c)}$, with $\epsilon_0, \epsilon_r, k_B, T, e, z, N_{Av}, c$

---

[b]Note that, since isotropically oriented water molecules do not contribute to the SH signal, tiny fluctuations in the water structure are sufficient to generate enough SH photons.

the vacuum and relative permittivity, Boltzmann constant, temperature, elementary charge, valency, Avogadro's number and ionic strength (in mol/L). We know from the analytical derivation of this phenomenon that the thickness of this weakly oriented hydration layer can have a significant impact and is highly dependent on the ionic strength of the solution. This explains why the emitted SH pattern is very sensitive to the structure of the interfacial water, the thickness of the DDL and the surface potential. These three parameters are represented by the second-order surface susceptibility ($\chi_s^{(2)}$ (at r=0, i.e. at surface of the droplet / liposome), the Debye length (κ^{-1}), and the surface potential (Φ_0), respectively. They determine the shape and magnitude of the SH intensity scattering patterns for which we just derived the analytical expressions in the previous chapter 3.
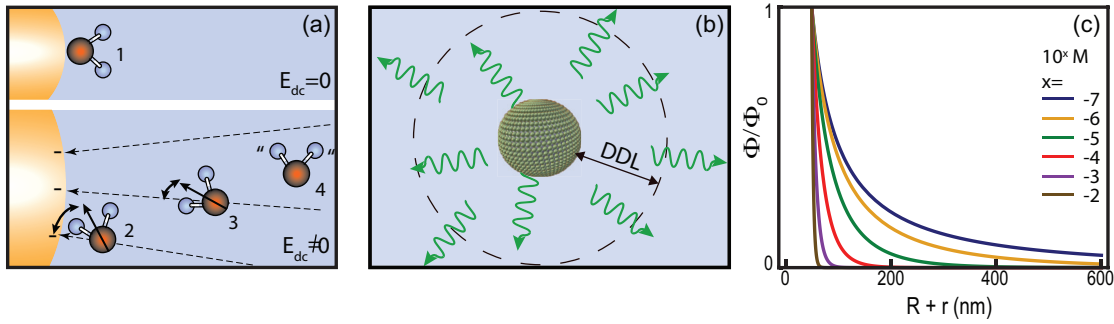
Figure 4.1: (a) Molecular sources for possible SH scattering:(1) the breaking of centrosymmetry by an interface ($\chi_s^{(2)}$) or (2) an electrostatic field that reorients the molecules at the surface or (3) in the bulk, and (4) the third-order response of isotropic molecules($\beta^{(3)}$).(b) Illustration of how SH photons are scattered from the interface and from oriented water molecules in the entire DDL.(c) Illustration of the decay of the surface potential into the solution as a function of the distance away from the center of the sphere (r+R), radius R= 50 nm.

4.3.2 AR-SHS theory for a collinear beam geometry

In the previous chapter, we used always the general form of the nonlinear light scattering equations (Eq. (3.13)), valid for both, sum-frequency and second harmonic generation. For SHS with a collinear beam geometry probing spherical scatterers in aqueous solutions and with the assumptions given in section 2.1.7 the non-zero susceptibility elements are related as follows

1. $\chi_{s,1}^{(2)} = \chi_{s,\perp\perp\perp}^{(2)} - \chi_{s,\|\|\perp}^{(2)} - \chi_{s,\|\perp\|}^{(2)} - \chi_{s,\perp\|\|}^{(2)}$

2. $\chi_{s,2}^{(2)} = \chi_{s,\|\|\perp}^{(2)}$

3. $\chi_{s,4}^{(2)} = \chi_{s,3}^{(2)} = \chi_{s,2}^{(2)}$

4. $\chi_4^{(3)'} = \chi_3^{(3)'} = \chi_2^{(3)'}$

Consequently, there remain only two independent scattered SH field components $E_{PPP}(2\omega)$, and $E_{PSS}(2\omega)$, which depend on the three parameters $\boldsymbol{\chi}_s^{(2)}$, the Debye length (κ^{-1}), and the surface potential Φ_0. We can describe the amplitude for these two components according to:

$$
\begin{aligned}
E_{ppp}(2\omega) &= \frac{ick_0^2}{2\pi|\hat{r}||\hat{I}|} \frac{e^{ik_0r_0}}{r_0} E(\omega)^2 \left[\cos\left(\frac{\theta}{2}\right)^3 \Gamma_1^{(2)} + \cos\left(\frac{\theta}{2}\right)\left(\Gamma_2^{(2)} + \Gamma_2^{(3)'}\right)(2\cos(\theta)+1) \right] \\
E_{pss}(2\omega) &= \frac{ick_0^2}{2\pi|\hat{r}||\hat{I}|} \frac{e^{ik_0r_0}}{r_0} E(\omega)^2 \cos\left(\frac{\theta}{2}\right)\left(\Gamma_2^{(2)} + \Gamma_2^{(3)'}\right)
\end{aligned}
$$

(4.1)

$\Gamma_1^{(2)}, \Gamma_2^{(2)}$ and $\Gamma_2^{(3)'}$ are non-zero elements of the effective particle second- and third-order susceptibility.[101,155,173] These quantities capture the combined symmetry of the scatterers and the incoming electromagnetic fields, the interfacial structure and the electrostatic field in the aqueous phase[173] (as discussed previously in chapter 3). The total effective particle susceptibility is a function of the surface second-order susceptibility $(\chi_s^{(2)})$ and the effective third-order susceptibility $(\chi^{(3)'})$ elements (with its three sources illustrated in Fig. 4.1a), the radius of the particle R, and the magnitude of the scattering wave vector $\left(q = |\mathbf{q}| = |(4\pi n_{H_2O})/(\lambda_{SH}) \sin(\theta/2)|\right)$. Considering a lossless nonlinear medium and iostropy in the interfacial plane, there remain only four independent elements of the effective particle susceptibility for spheres:

$$
\begin{aligned}
\Gamma_1^{(2)} &= \left(2F_1(qR) - 5F_2(qR)\right)\chi_{s,1}^{(2)''}, \\
\Gamma_2^{(2)} &= F_2(qR)\chi_{s,1}^{(2)''} + 2F_1(qR)\chi_{s,2}^{(2)''}, \\
\Gamma_1^{(3)'} &= 0, \\
\Gamma_2^{(3)'} &= 2\chi_2^{(3)''}\Phi_0\left(F_1(qR) + F_3(qR,\kappa R)\right),
\end{aligned}
$$

(4.2)

$\chi_{s,1}^{(2)''}$ and $\chi_2^{(3)''}$ are second and third-order susceptibilities that are corrected for changes in the refractive index between medium and particle following Ref. [119] so that we can consider a negligible dispersion (see section 2.1.7). Table 4.1 contains the analytical expressions for the corrected surface susceptibility $\left(\chi_{s,1}^{(2)''}, \chi_{s,2}^{(2)''}\right)$ and the DDL $\left(\chi_2^{(3)''}\right)$. $F_{1,2,3}$ are analytical goniometric scattering form factor functions for spheres that depend on R, q and in the case of F_3, also on κ. Although the detailed expressions were listed in the previous chapter already, for a compact summary, we restate the analytical expression for the form factor functions $F_{1,2,3}$ and the scattering vector ($\mathbf{q}$) in Table 4.1.

Table 4.1: Equalities and analytical expressions used for computing Eqs. (4.1) and (4.2) comprised of the susceptibility elements of the interface and diffuse layer, the form factor functions, and the scattering vector.

Equalities	$\chi_{s,1}^{(2)} = \chi_{s,\perp\perp\perp}^{(2)} - \chi_{s,\|\|\perp}^{(2)} - \chi_{s,\|\perp\|}^{(2)} - \chi_{s,\perp\|\|}^{(2)}$ $\chi_{s,2}^{(2)} = \chi_{s,\|\|\perp}^{(2)}$ ($\perp$: surface normal direction; $\|$: tangential direction) $\chi_{s,4}^{(2)} = \chi_{s,3}^{(2)} = \chi_{s,2}^{(2)}; \quad \chi_4^{(3)'} = \chi_3^{(3)'} = \chi_2^{(3)'}$
Susceptibility elements[99,155]	$\chi_{s,1}^{(2)''} = 27\eta \frac{\left(\chi_{s,1}^{(2)}\eta^2 + 3\chi_{s,2}^{(2)}(\eta^2-1)\right)}{(2+\eta)^3}; \eta = \left(\frac{n_p}{n_{H_2O}}\right)^2$ $\chi_{s,2}^{(2)''} = 27\eta \frac{\chi_{s,2}^{(2)}}{(2+\eta)^3}$ $\chi_2^{(3)''} = 27\eta \frac{\chi_2^{(3)'}}{(2+\eta)^3}; \chi_2^{(3)'} = \frac{N_b}{\epsilon_0}\left(\beta^{(3)} + \frac{\beta^{(2)}\mu_{dc}}{3k_bT}\right)$
Form factor functions and scattering vector	$F_1(qR) = 2\pi R^2 i\left(\frac{\sin(qR)}{(qR)^2} - \frac{\cos(qR)}{qR}\right)$ $F_2(qR) = 4\pi R^2 i\left(3\frac{\sin(qR)}{(qR)^4} - 3\frac{\cos(qR)}{(qR)^3} - \frac{\sin(qR)}{(qR)^2}\right)$ $F_3(\kappa R, qR) = 2\pi R^2 i\frac{qR\cos(qR)+\kappa R\sin(qR)}{(qR)^2+(\kappa R)^2}$ $\mathbf{q} \equiv \mathbf{k_0} - 2\mathbf{k_1}; q = \left|\frac{4\pi n_{H_2O}}{\lambda_{SH}}\sin\left(\frac{\theta}{2}\right)\right|$

4.3.3 Experimental verification of equations

In this section, we want to verify the previously derived equations experimentally. Considering the derivations for scattering in chapter 3 and the applicability to our experimental system via Eq. (4.1), we recorded scattering patterns from a dispersion of R=75 nm hexadecane droplets stabilized with hexanol in ultrapure water. These droplets have been previously characterized with sum-frequency scattering[32] so that we know the interfacial structure. Figure 4.2 displays the SH scattering patterns in the two independent polarization combinations. The ζ-potential of the droplets was -37 mV. The black lines in Fig. 4.2 are fits for both the PPP and PSS data obtained using Eqs. (3.12) and (3.13) replacing $\mathbf{\Gamma}^{(2)}$ with the combined $\mathbf{\Gamma}^{(2)}$ and $\mathbf{\Gamma}^{(3)'}$ expressions, in which $\mathbf{\Gamma}^{(3)'}$ is designated as in Eq. (3.19), with R=75 nm (as obtained from dynamic light scattering), κ^{-1}= 168 nm ($c = 3.32 \times 10^{-6}$ mol/L), and $\chi_{s,2}^{(2)}/(\chi_2^{(3)'}\Phi_0) = 3.8$. The fits (black lines) represent the data very well. The scattering patterns can be broken down into a surface- ($\chi_s^{(2)}$ only) and a diffuse EDL ($\chi^{(3)'}$only)- contribution. With this procedure we determine that 55 % of the total emitted field from this sample originates from the DDL. The grey line is the fit considering $\mathbf{\Gamma}^{(3)'}$ from Eq. (3.17), (without the DDL (F$_3$) contribution). This curve does not capture the typical asymmetric

shape of the scattering pattern and peaks at a larger scattering angle indicative of an underestimation of the effective size of the droplets and an equation lacking the right contributions. We thus find that adding the contribution from the soft shell of weakly oriented water molecules to the scattering formalism describes the SHS patterns at ionic strengths $< 10^{-3}$ M very accurately. If we had not incorporated this contribution, we would end up with the grey lines in Fig. 4.2.
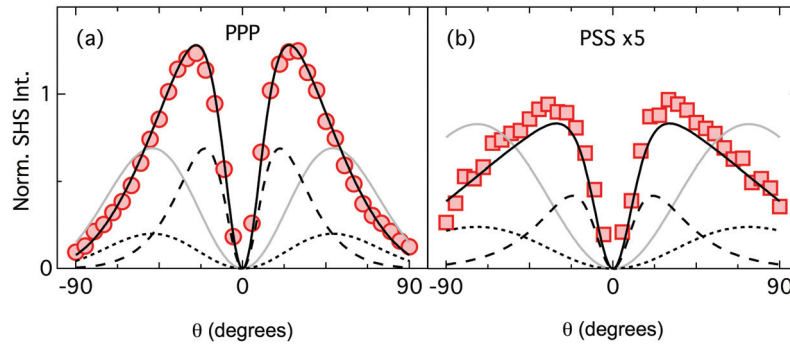
Figure 4.2: SHS intensity patterns of hexanol-covered hexadecane droplets in ultrapure water for the (a) PPP and (b) PSS polarization combinations. The best fit (black line) was achieved using Eq. (3.19) for $\mathbf{\Gamma}^{(3)'}$, i.e. using the contribution of $F_3(\kappa R, qR)$ to describe the behavior at low ionic strength. The gray line represents the best fit without the $F_3(\kappa R, qR)$ correction, i.e. using Eq. (3.17) for $\mathbf{\Gamma}^{(3)'}$. The intensities originating from a pure surface response, $\chi^{(3)'} = 0$, and pure bulk response, $\chi_s^{(2)} = 0$, are displayed as dotted and dashed lines, respectively.

Next, we quantify the impact of the F_3- contribution at a fixed angle for an SHS experiment as a function of salt concentration as simulated in Fig. 3.6. Figure 4.3 shows the scattering intensity for liposomes composed of DOPC and DOPS lipids in a 9:1 ratio at $\theta = 50°$ as a function of added electrolyte concentration normalized for comparability with the strongest SH response in pure water. We used three different monovalent symmetric electrolytes: LiCl, KCl, and NaCl. The SH intensity shows the same trend for all three salts. Above 10 µM added salt, the intensity drops until it saturates around 10^{-2} M. The drop of the SH signal can be explained by two interfering effects. First, the F_3-contribution scales inversely with higher salt concentration. Second, screening of the surface charges and the presence of additional ions may result in less intensity and support the intensity decay. For comparability, the solid lines shows the trend of the F3-contribution for the respective radii, scattering angle, and ionic strength. The salt concentration is the most crucial parameter and its magnitude affects the slope and onset of the decay of the F_3-curves. The error bar on the x-axis consider the slightly different final ionic strengths due to counterions from the lipids. Although these counterion concentration is rather low, it can have a big impact at low ionic strength. This also means that the left hand side in the plot ($< 10^{-5}$ M) has big error bars in x-direction. Nevertheless it still shows an almost constant

intensity trend. The inset shows the data plotted as a function of total ionic strength of the solution. Considering the uncertainty in the ionic strength, the SH intensity behavior represents the simulated trend as plotted in Fig. 3.6 for a detection angle of $\theta = 45°$ rather well.
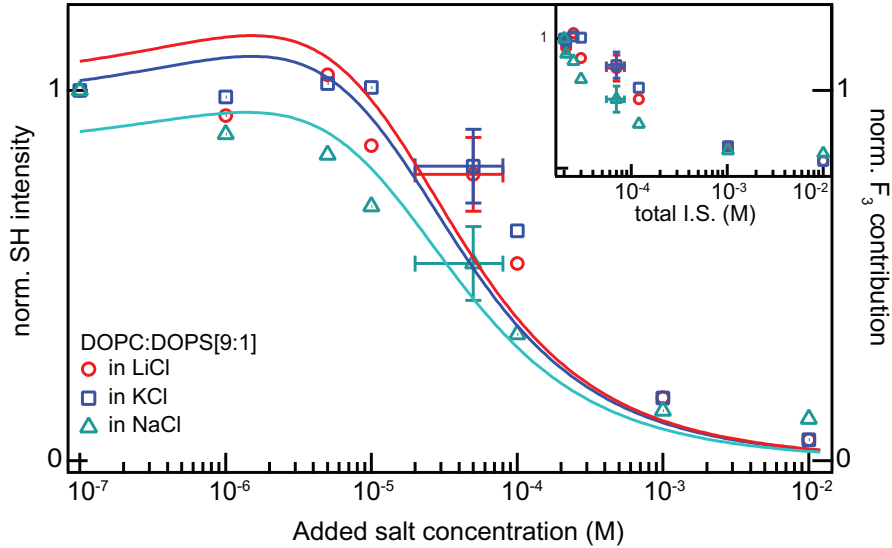
Figure 4.3: SH intensity trend at a fixed scattering angle $\theta = 50°$ as a function of added salt concentration for three monovalent salts: LiCl, KCl and NaCl. The computed trend for the F_3- contribution is laid on top. Inset: The same data plotted for overall ionic strength of the sample and not just added salt concentration.

To extract surface potential values from the data, we can use the derived expressions of chapter 3. However, we need to relate the measured data that is a relative quantity to absolute quantities for the parameters required in these expressions: $\boldsymbol{\beta}^{(2)}, \boldsymbol{\beta}^{(3)}$, number of contributing molecules, interfacial thickness and ionic strength, radius of the particle, temperature, and refractive indizes. Unfortunately, we cannot directly link detector counts using a certain polarization combination to a certain magnitude of the $\beta^{(2)}$ component. We therefore use a normalization scheme that employs water as a reference. This reference has the advantage that the $\boldsymbol{\beta}^{(2)}$ and $\boldsymbol{\beta}^{(3)}$ values for uncorrelated water are known so that we can use the calibrated SSS response of water. Using this approach we are able to compare data sets measured at different times and under different conditions.

4.3.4 Implementation: Normalization to the bulk water response

In order to obtain reliable and reproducible SHS values independent of the used setup and alignment, we normalized the data according to (2.1), which results in a pure surface SH intensity. Without multiple scattering effects, the intensity generated in the focal volume corresponds to the intensity of a single particle multiplied by the

number of particles in the volume. Following Eq. (4.1), the AR-SHS data in the two independent polarization combinations, normalized by the bulk water signal, are then

$$\frac{I_{PPP}(\theta)}{I_{SSS}(\theta)} = \frac{\left(E_P(\omega)^2 \left[\cos\left(\frac{\theta}{2}\right)^3 \Gamma_1^{(2)} + \cos\left(\frac{\theta}{2}\right)\left(\Gamma_2^{(2)} + \Gamma_2^{(3)'}\right)(2\cos(\theta) + 1)\right]\right)^2}{\langle\bar{\mu}^2\rangle N_b / N_p}$$

$$\frac{I_{PSS}(\theta)}{I_{SSS}(\theta)} = \frac{\left(E_S(\omega)^2 \left[\cos\left(\frac{\theta}{2}\right)\left(\Gamma_2^{(2)} + \Gamma_2^{(3)'}\right)\right]\right)^2}{\langle\bar{\mu}^2\rangle N_b / N_p}$$

(4.3)

with $\bar{\mu} = \bar{\beta}_{H_2O}^{(2)} E(\omega)^2$ being the averaged induced dipole moment of a water molecule. To compute the values for the scattered SH intensities, we use this dipole moment and the hyperpolarizability tensor elements of water that were computed with an ab-initio model in which the water molecule is represented as three point charges (using 1064 nm as wavelengths for the incoming light, Table 4, Model IIIa, in Ref. [198]). Although there are 3 ($\boldsymbol{\beta}^{(2)}$) or 6 ($\boldsymbol{\beta}^{(3)}$) nonzero tensor elements for a single water molecule, averaging over many water molecules in an isotropic liquid will produce a single valued response,[101,117] here indicated as $\bar{\beta}^{(2)}$ and $\bar{\beta}^{(3)}$. N_p is the density of particles, and N_b is the density of bulk water (3.34×10^{28} molecules/m^3). N_b/N_p represents the number of bulk water molecules per particle. The respective values for the dipole moment, the hyperpolarizabilities and calculated third-order susceptibility are given in Table 4.2. With the distribution of water being broad,[101,122,199] $\chi_1^{(2)}$ becomes negligible (section 2.1.7 assumption 4).[122] Using Eqs.(4.3) to describe data processed according to Eq. (2.1), we can obtain $\chi_{s,2}^{(2)}$ and Φ_0 independently.

Table 4.2: Constants used to compute water normalized SH intensities.

Constants[198]	$\mu_{dc} = 8.97 \cdot 10^{-30}$ Cm
	$\bar{\beta}^{(2)} = 3.09 \cdot 10^{-52}$ C^{3}m^{3}J^{-2}
	$\bar{\beta}^{3)} = 4.86 \cdot 10^{-62}$ C^{4}m^{4}J^{-3}
	$\chi_{s,1}^{(2)} \to 0$ (see Ref. [122])
	$\chi_2^{(3)'} = 10.3 \cdot 10^{-22}$ m^2/V^2 (calculated from $\bar{\beta}^{(3)}$)

4.3.5 Oil droplets and DOPC liposomes in aqueous solutions

Figures 4.4a and 4.4b show SHS scattering patterns obtained for a solution of hexadecane droplets (R=80 nm) in weakly basic solution (pH~ 8). Although it is also a droplet system, this bare droplet system is different from surfactant stabilized droplets
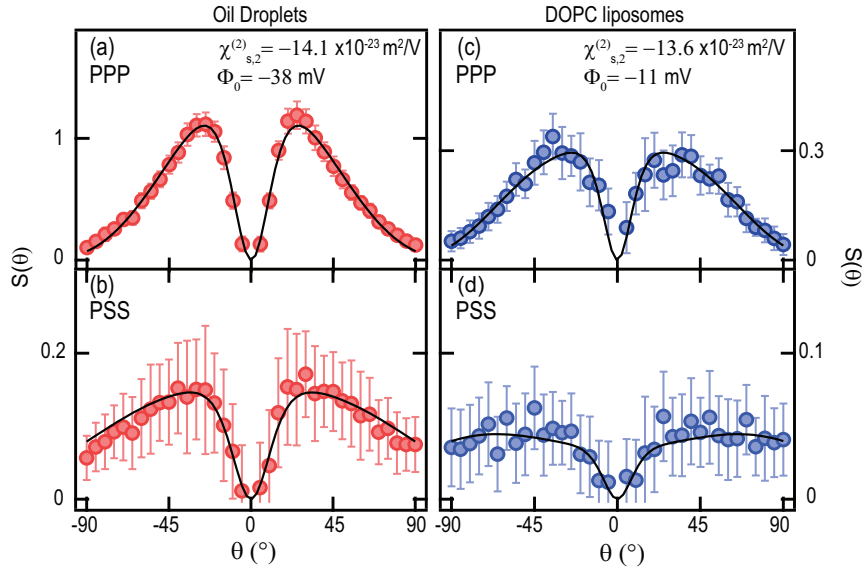
Figure 4.4: Scattering patterns of hexadecane droplets [red, panels (a) and (b)] and DOPC liposomes [blue, panels (c) and (d)] in water. The polarization combinations PPP (PSS) are shown on the top (bottom). Error bars represent the standard deviation of 20 measurements.

studied in Refs. [32, 155, 194] and in Fig. 4.2, because of a different interfacial structure. We chose this system because the magnitude and origin of the surface charges on neutral droplets or air bubbles continues to be a matter of debate.[162] It is still not understood what may be the magnitude and sign of the surface potential for such a system.[168] Hence, it is quite crucial to determine a reliable value of the droplet's surface potential in order to remove the uncertainty about both magnitude and sign of the potential. The error bars represent the standard deviation from 20 measurements. The scattering patterns are different for the PPP and PSS polarization combinations. The black lines are fits to Eq. (4.3) using the input parameters as stated in Table 4.3. As already discussed in the previous chapter, AR-SHS patterns of droplets at very low ionic strength present a very peculiar shape induced by the $F_3(qR, \kappa R)$ factor. Thanks to the normalization by the bulk water signal described by Eq. (2.1) and the use of Eqs. (4.3), it is now possible to fit the data obtained in the two polarization combinations under these low ionic strength conditions and independently determine $\chi_{s,2}^{(2)}$ and Φ_0. For the droplet system we find $\chi_{s,2}^{(2)} = -(1.41 \pm 0.20) \times 10^{-22}$ m^2/V and $\Phi_0 = -(38 \pm 15)$ mV. The given error in the potential takes the variations from the experimentally determined parameters (the radius, the number density, and $\chi_{s,2}^{(2)}$) into account. The corresponding value of the ζ-potential is ζ = -32 ±9 mV, which is similar in magnitude. Here, the error represents the standard deviation of the measured distribution. DOPC is a zwitterionic phospholipid. DOPC liposomes in pH neutral solutions are therefore expected to have a negligible surface potential. Figs. 4.4c and 4.4d display scattering patterns of DOPC liposomes (R=47 nm) in water. The fit to Eq. (4.3)

(black lines) results in $\chi^{(2)}_{s,2} = -(1.36 \pm 0.20) \times 10^{-22}$ m^2/V and $\Phi_0 = -(11 \pm 20)$ mV. The ζ-potential of DOPC liposomes is $\zeta = -(6 \pm 7)$ mV. Both values, indeed, indicate that the DOPC interface has negligible or a very small electrostatic surface potential.

Table 4.3: Input parameters for global fit analysis of scattering patterns from oil droplets and DOPC and DOPS liposomes.

	R [nm]	N_P [ml^{-1}]	Added NaCl [M]	Ionic Strength of solution [M]	Temp [°C]	$n_{particle}$ (1028 nm)	κ^{-1} [nm]
Oil droplets	80 ± 8	$(3.6 \pm 0.3) \times 10^{11}$	0	$(4 \pm 1) \times 10^{-6}$	24	1.435[200]	153
DOPC	47 ± 5	$(3.3 \pm 0.3) \times 10^{12}$	0	$(2.2 \pm 1) \times 10^{-6}$	24	1.4[201]	207
DOPS	57 ± 5	$(3.09 \pm 0.3) \times 10^{12}$	0	$\left(150^{+100}_{-75}\right) \times 10^{-6}$	24	1.4[201]	25
	55 ± 5	$(2.92 \pm 0.3) \times 10^{12}$	10×10^{-6}	$\left(130^{+100}_{-75}\right) \times 10^{-6}$	24		27
	55 ± 5	$(2.92 \pm 0.3) \times 10^{12}$	50×10^{-6}	$\left(190^{+100}_{-75}\right) \times 10^{-6}$	24		22
	55 ± 5	$(2.92 \pm 0.3) \times 10^{12}$	100×10^{-6}	$\left(210^{+100}_{-75}\right) \times 10^{-6}$	24		21
	54 ± 5	$(3.27 \pm 0.3) \times 10^{12}$	500×10^{-6}	$\left(500^{+300}_{-250}\right) \times 10^{-6}$	24		13
	50 ± 5	$(3.78 \pm 0.3) \times 10^{12}$	10×10^{-3}	$\left(10^{+0.3}_{-0.05}\right) \times 10^{-3}$	24		3

4.3.6 $\chi^{(2)}_s$

The values of $\chi^{(2)}_{s,2}$ for oil droplets $\left(-(1.41 \pm 0.20) \times 10^{-22}\text{m}^2/\text{V}\right)$ and DOPC liposomes $\left(-(1.36 \pm 0.20) \times 10^{-22}\text{m}^2/\text{V}\right)$ are comparable in magnitude and sign. $\chi^{(2)}_{s,2}$ is a measure of the orientation of the water molecules at the interface. Our observation thus supports the idea that an electrostatic field, such as that present in the Stern layer, is not strong enough to affect the shape of the orientational distribution function of water molecules.[122] These values are also in good agreement with the nonresonant value of $\chi^{(2)}_{s,2,\text{eff}} = -(1.30 \pm 0.40) \times 10^{-22}$ m^2/V obtained from sum-frequency generation experiments,[202] performed on the air/liquid interface. They are also within the range of $\chi^{(2)}_{s,2}$ values of -0.04×10^{-22} m^2/V and -2.26×10^{-22} m^2/V found from numerical simulations.[158,203]

4.3.7 DOPS liposomes in aqueous solutions vs. ionic strength

Figure 4.5a and 4.5b show SHS patterns from anionic DOPS liposomes obtained in the PPP and PSS polarization combinations with different ionic strength. The SHS intensity decreases when the ionic strength is increased and further addition of salt, up to 100 mM (not shown), does not induce further changes in the AR-SHS patterns. The decrease in intensity is expected because the additional salt screens effectively the surface charges and decreases the size of the DDL (Fig. 4.1c). The charge screening reduces the extent of the somewhat ordered water molecules contributing to the scattered SH light, and the decrease of the DLL reduces the effective radius of the

probed 'soft shell' (Fig. 4.1b); both effects diminish the scattered SH intensity. We fit the data with a single value of $\chi_{s,2}^{(2)} = -(1.40 \pm 0.20) \times 10^{-22}$ m^2/V, because the strength of the electrostatic field in this range is insufficient to alter the orientational distribution of water.[122,155] Using the input parameters as listed in Table 4.3 and a global fit, we obtain values for Φ_0 ranging from -149 ± 30 mV for 0.15 mM ionic strength down to -23 ± 30 mV at 10 mM (Fig. 4.5c). The error represents the propagated uncertainty considering different values for $\chi_2^{(2)}$, the standard deviation of the radius and correspondingly altered number densities. Note though, that altering other constants, in particular the dielectric constant, would also result in values within these error bars. The predicted trend of the surface potential is in agreement with expectations: The surface potential is found to decrease with the ionic strength. The ζ-potential varies between -52 mV < ζ < -34 mV for all solutions in agreement with earlier measurements.[204–206] The fact that overall $|\zeta| < |\Phi_0|$ is reasonable because the ζ-potential is measured at the slipping plane, which is located at some distance away from the interface, and it does not represent the surface potential.[135] Comparing the patterns from Fig. 4.4 with the DOPS patterns (Fig. 4.5), the shape of the DOPS AR-SHS patterns is quite different. This difference arises because DOPS liposomes contain Na$^+$ counterions that increase the ionic strength of the solution to > 100 μM, even if no extra salt is added. Therefore, the contribution of $F_3(qR, \kappa R)$ in Eq. (4.2) will be very small in contrast to the measurements of DOPC and bare oil droplets.
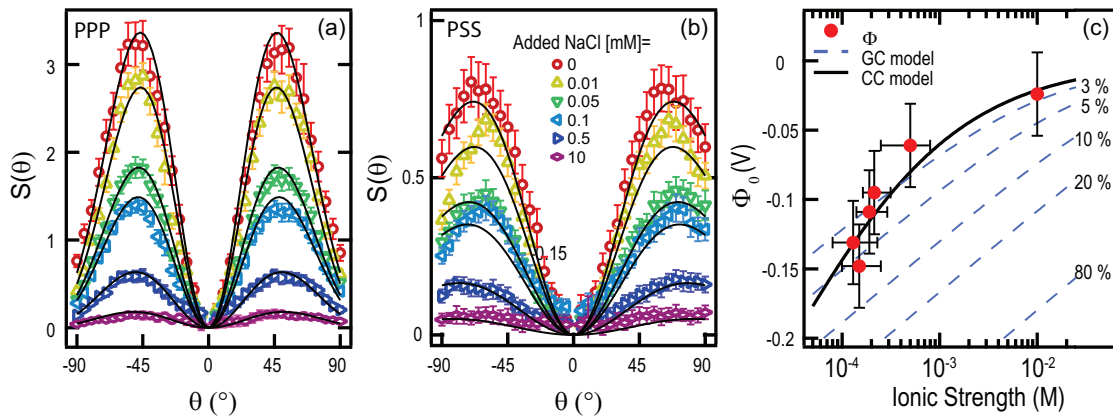
Figure 4.5: The SHS patterns from DOPS lipsomes in solution.(a) The PPP- and (b) PSS-polarization combination. Error bars represent the standard deviation of 20 measurements. (c) The extracted surface potential vs. ionic strength. Error bars represent the total uncertainty from propagating the standard deviations for $\chi_{s,2}^{(2)}$, the number density and the radius, which have the most impact on the fitting routine. The dashed blue lines represent surface potential values calculated with the GC model for spherical particles,[207] using different surface charge densities σ_0 (indicated as degree of ionization of the DOPS head groups in the outer leaflet). The solid black line represents a fit using the spherical CC model. Table 4.3 contains all experimental parameters to compute the plotted values.

4.3.8 Comparison between the SHS derived values and solutions to the Gouy-Chapman and constant capacitor model

Finally, we examine how our Φ_0 values for DOPS compare to the spherical GC or spherical CC models.[208] To do this, we compute solutions for the surface potential as a function of ionic strength for a given surface charge density, which relates to the degree of ionization (unscreened surface charges) of the lipids in the outer leaflet.[154] The dashed blue lines in Fig. 4.5c correspond to solutions to the spherical GC model (Eq. 7.11.11 in Ref. [67]), with a surface charge density that corresponds to 80 %, 20 %, 10 %, 8 %, 5 % and 3 % ionization of PS head groups in the outer leaflets of the membrane of DOPS liposomes, assuming a head group area of 0.653 nm^2.[55] A single GC curve cannot fully capture all the data. Within the assumption that the interfacial water can be treated as a bulk dielectric and that ions are point charges without hydration shells, this suggests that the charge density of the interface may change with ionic strength. Hence, the phospholipid dissociation decreases with increasing ionic strength. The solid black line represents a solution to the spherical CC model assuming a lipid head group ionization of ~2 % ($\sigma_0 = (-5 \pm 0.6) \times 10^{-3}$ Cm^{-2}) (Eq. 50 in Ref. [208]). Within this model a constant degree of lipid ionization describes the observed trend with a similar accuracy as the GC model except for the DOPS liposomes in pure water. Although we have no information about the validity of the assumptions in both models, a comparison to the data suggests that the degree of ionization of the liposomes is below 20 % of all available charges in the outer leaflet of the membrane. Riske *et al.* determined the ionization of anionic dimyristoylphosphatidylglycerol (DMPG) liposomes in pure water based on linear light scattering techniques and a modified GC model, which considers the association constants of ions.[209] They found an ionization of 12 %, which is comparable to what we report. In the next chapters, we will analyze the surface properties of liposomes in more detail focusing first, in chapter 5, on hydration of and lipid distributions and lipid interactions in membranes and then, in chapter 6, on the electrostatic properties of membranes.

4.4 Conclusions

In this chapter we demonstrated the possibility to obtain unique values for the surface potential of nanoscopic objects in aqueous solutions by employing nonresonant AR-SHS measurements that are calibrated by the incoherent response of bulk water. We successfully applied the method to aqueous dispersions of nanoscopic oil droplets (Φ_0=-38 mV), zwitterionic DOPC (Φ_0= -11 mV) and anionic DOPS liposomes at different ionic strengths (-148 mV < Φ_0 < -23 mV). With this proof of principle we enabled the analysis of potentials in charge neutral and low ionic strength dispersions. The obtained values are extremely useful for theoretical work, because the values are derived from analytical expressions without assuming a certain simplified model

for neither the distribution of ions in the electrical double layer, nor the hydration structure of ions and the orientation of water molecules. In addition, as this experimental table-top method is non-invasive and applicable to aqueous solutions with particles of various sizes, it will be of great value to characterize and understand the electrostatic properties and molecular structure of many biologically and chemically relevant interfaces.

5 Intermolecular headgroup interaction and hydration as driving force for lipid transmembrane asymmetry

Variations between the inner and outer leaflets of cell membranes are crucial for cell functioning and signaling, drug-membrane interactions, and the formation of lipid domains. Transmembrane asymmetry can in principle be comprised of an asymmetric charge distribution, differences in hydration, specific headgroup/ H-bonding interactions or a difference in the number of lipids per leaflet. Here, we characterize the transmembrane asymmetry of small unilamellar liposomes consisting of zwitterionic and charged lipids in aqueous solution using vibrational SFS and SHS, label-free methods, specifically sensitive to lipid and water asymmetries. For single component liposomes, transmembrane asymmetry is present for the charge distribution and lipid hydration, but the leaflets are not detectably asymmetric in terms of the number of lipids per leaflet, even though geometrical packing arguments would predict so. Such a lipid transmembrane asymmetry can, however, be induced in binary lipid mixtures under conditions that enable H-bonding interactions between phosphate and amine groups. In this case, the measured asymmetry consists of a different number of lipids in the outer and inner leaflet, a difference in transmembrane headgroup hydration, and a different headgroup orientation for the interacting phosphate groups.

5.1 Introduction

Cells require a compositional diversity between the inner and outer leaflets of cellular and organelle membranes in order to function properly. In nature, there are non-random and non-equal leaflet compositions in eukaryotic membranes.[4,210,211] Certain lipids, such as glycolipids, phosphatidylcholine (PC) and sphingomyelin, are predominantly in the outer leaflet, whereas others, such as phosphatidylserine (PS), remain almost completely in the inner leaflet of the plasma membrane.[212] Although the molecular level details are still ambiguous, it is clear that transmembrane asymmetry[213] is vital for a cellular functioning. PS transmembrane asymmetry was, for example, shown to regulate and maintain cell metabolism.[214,215] Different pathways, active and passive, are responsible for such a lipid transmembrane asymmetry.[4,212] Active pathways use regulating proteins and peptides to induce asymmetry,[211,216,217] whereas passive pathways comprise several effects: a non-homogeneous inter-leaflet charge distribution or hydration, asymmetry of specific interactions, and packing differences between leaflets. Although all these effects have been studied, the most attention has been given to transmembrane asymmetry as caused by a different available area of the inner and outer leaflet. This difference results in a different number of lipids in the inner and outer leaflet, and is related to local membrane stiffness and curvature.[125]

   The investigation of passively induced asymmetry[43,46,50,218–225] is in general challenging as it ideally requires free floating, unperturbed, membranes. Labels, substrates, or invasive tools can induce changes to the bilayer composition and should therefore ideally be avoided.[226] Furthermore such investigations require sensitivity to molecular structure and the ability to distinguish between the inner and outer leaflet of a bilayer. Vibrational sum frequency generation (SFG)[87,88,96,227] is a nonlinear spectroscopy that can be considered as a simultaneous IR and Raman measurement. SFG is forbidden in a centrosymmetric medium (under the dipole approximation[92]). It can therefore directly detect transmembrane asymmetry. Assuming identical orientational distributions, with respect to the surface plane, for lipids located in the inner and outer leaflet, SFG reports on the average number difference of lipids between these two leaflets. Conboy *et al.* demonstrated these features by measuring the lipid redistribution across a supported planar bilayer that was initially made asymmetric.[43,50,219]

   In this chapter, we study the hydration, charge and lipid transmembrane asymmetry in free-floating lipid membranes in form of unilamellar liposomes (diameter < 100 nm) using both sum frequency scattering (SFS) and SHS. Probing the C-H and P-O stretch region of the vibrational spectrum with vibrational SFS,[24,105,152] we quantify the transmembrane asymmetry of the fatty acid tails and headgroups of the lipids. With AR-SHS, we determine the transmembrane hydration asymmetry. The SHS signal relates not only to the surface potential[100,104,111,112,228] as shown in the pre-

vious chapter, but also to H-bond interactions involving water.[177] We find that charge and hydration asymmetry is present for liposomes made of DOPC, DPPC, DOPS, and DPPS, and mixtures of either DOPC with DPPS or DPPA. Figure 2.13 displays a sketch of the chemical structure of each lipid. For the same single component liposomes, we do not find lipid transmembrane asymmetry, even though calculations using a constant area per lipid indicate a detectable difference in lipid number between the inner and outer leaflet. Binary mixtures may display transmembrane asymmetry, which we can detect in the phosphate stretch region as a shifted vibrational resonance. This PO_2^- group is oriented more parallel to the surface normal, compared to the same group in a lipid monolayer. We observe also a SFS signal of the acyl chains, but only for one of the lipids. These observations will only occur if phosphoserine is part of the bilayer and the acyl chains of the two lipids are different in length. Based on these observations and the structure of the lipids, we suggest that H-bonding interactions induce such kind of lipid transmembrane asymmetry. The H-bonding happens between amine and phosphate groups and depends on packing differences created by differences in the fatty acid chain structures. Using this interpretation, we quantify the amount of asymmetry in the liposomes composed of a DOPC:DPPS mixture. We first describe transmembrane hydration and lipid asymmetry for single component liposomes and then move on to binary mixtures. Finally we quantify the measured transmembrane asymmetry in terms of percentage number differences and differences in the orientational distributions of phosphate groups as part of the headgroup.

5.2 Materials & Methods

5.2.1 Lipids

Lipids used in this study are: DOPC, DPPC, DOPS, DPPS, DPPA, DPPE, d_{62}-DPPS, and d_{66}-DOPC. The chemical structures of the used lipids are presented in Fig. 2.13 and the liposome characterization is given in Table 5.1. For SFS experiments probing the transmembrane asymmetry by analyzing the CH mode of the hydrocarbon tails, the fatty acids of one of the two lipids were deuterated to generate an artifical contrast. Vesicles were prepared according to the description in section 2. For lipids that have a higher transition temperature than the room temperature, all solutions were heated to be above the transition temperature for all processing steps.

5.2.2 SHS measurements and normalization

Scattering patterns were recorded in steps of 5° from $\theta = -90°$ to $\theta = 90°$ with 0° being the forward direction of the fundamental, and using an acceptance angle of 3.4°. Data points were acquired using 20 x 1.5s acquisition time with a PMT gate width of 10 ns. SH signals were evaluated according to (2.1) to account for incoherent Hyper-

Table 5.1: The results of dynamic light scattering and electrophoretic measurements with standard deviations from the mean of three measurements.

Sample	Hydrodynamic diameter [nm]	ζ-potential [mV]
DPPS	98.4 ±0.5	-45 ±-1
DOPC	94.0 ±0.3	-6 ±-1
DPPC	96.0 ±0.3	-4 ±-1
d_{66}-DOPC:DPPS	90.4 ±0.4	-42 ±-1
DOPC:d_{62}-DPPS	69.8 ±0.3	-43 ±-1
DOPC:DPPS	95.3 ±0.3	-43 ±-1

Rayleigh scattering and the measurement geometry. We additionally corrected the so obtained SH signals S(θ) for size differences and varying number densities (see Fig. 6.1). The size correction is made according to section 2.2.2, Eq. (2.8).

5.2.3 Vibrational sum-frequency scattering (SFS)

Vibrational sum frequency spectra were measured using the setup for sum frequency generation experiments described in Ref. [98, 179, 229]. An 800 nm regeneratively amplified Ti:sapphire system (Spitfire Pro, Spectra physics) seeded with an 80 MHz 800 nm oscillator (Integral 50, Femtolasers) was operated at a 1 kHz repetition rate to pump a commercial OPG/OPA/DPG system (HE-TOPAS-C, Light Conversion), which was used to generate IR pulses. The visible beam was split off directly from the amplifier, and spectrally shaped with a home-built pulse shaper. The angle between the 10 μJ visible (VIS) beam (800 nm, FWHM 15 cm^{-1}) and the 6 μJ IR beam (9700 nm or 3200 nm, FWHM 160 cm^{-1}) was 20° (as measured in air). The focused laser beams were overlapped in a sample cuvette with a path length of 200 μm. At a scattering angle of 55°, the scattered SF light was collimated using a plano-convex lens (f=15 mm, Thorlabs LA1540-B) and passed through two short wave pass filters (3rd Millenium, 3RD770SP). The SF light was spectrally dispersed with a monochromator (Acton, Spec-traPro 2300i) and detected with an intensified CCD camera (Princeton Instruments, PI-Max3) using a gate width of 10 ns. The acquisition time for a single spectrum was 10-20 min for PO stretch modes and 40 min for CH stretch modes for liposomes. A Glan-Taylor prism (Thorlabs, GT15-B), a half-wave plate (EKSMA, 460-4215) and a polarizing beam splitter cube (CVI, PBS-800-050) and two BaF$_2$ wire grid polarizers (Thorlabs, WP25H-B) were used to control the polarization state of the SFG, VIS and IR beams respectively. The SFG, and VIS beams were polarized in the vertical (S) direction, and the IR beam was polarized in the horizontal plane (P), leading to the

polarization combination SSP. The recorded intensity was baseline subtracted and normalized to the SFG spectrum of a gold mirror in the PPP polarization combination that was recorded before each measurement.

Measurements were done at 5 mg/ml lipid concentration.

5.2.4 SFS spectral fitting

The SFS signal (S) can be described by the following Lorentzian line shape expression[230]

$$S_{\mathrm{SFS}}(\theta, \omega) \propto \left| A_{\mathrm{NR}}(\theta) f(\omega) e^{i\phi_{\mathrm{NR}}} + \sum_i \frac{A_i(\theta)\gamma_i}{\omega - \omega_i + i\gamma_i} \right|^2, \tag{5.1}$$

where $A_{\mathrm{NR}}(\theta)$ is the amplitude and $f(\omega)$ is the spectral shape of a weakly dispersive ('non-resonant') background, ϕ_{NR} is the phase of the background signal relative to that of the resonant signal, $A_i(\theta)$ is the amplitude of the i-th vibrational mode with the resonance frequency ω_i and linewidth γ_i. The strength of the vibrational mode is proportional to A_i ($\omega = \omega_i$). The SFS spectra ($I_{\mathrm{SF}}/I_{\mathrm{IR}}$) were fitted using Eq. (5.1), employing IGOR Pro 6 (WaveMetrics) and using Levenberg-Marquardt iterations. The fitted parameters for the SFS spectra are shown in Table 5.2 and 5.3. The SFS intensity in the s-PO$_2^-$ stretch region in the SPS polarization combination was too low to reliably fit for all the samples. The SFS spectra that do not show any detectable features are fitted with a third order polynomial.

Note that, for the SFS data, we first plot the measured spectrum ($I_{\mathrm{SF}}/I_{\mathrm{IR}}$). Then we use the procedure outlined in 5.2.5 to compute the average asymmetry per liposome in lipid number density using the fitted amplitudes of the symmetric (s-) P-O stretch and the symmetric (s-) CH$_3$ stretch mode as input. For both the SHS and SFS experiments, we correct for polydispersity by replacing the radius R in Eq. (2.8) with an effective radius (R$_{\mathrm{eff}}$). The procedure to calculate R$_{\mathrm{eff}}$ is described in 2.2.3.

5.2.5 Calculation of the orientational distribution of phosphate groups

The orientational analysis to calculate ratio of SFS amplitudes in the SSP and PPP polarization combinations of s-PO$_2^-$ vibration is adapted from our procedure published earlier[32,101] based on Rayleigh-Gans-Debye approximation in combination with nonlinear light scattering theory. We use a tilt angle ϕ of PO$_2^-$ group to the surface normal and a twist angle ψ of the PO$_2^-$ group about its molecular axis with respect to the surface normal. This results in the following relation[231] between surface second-order

polarizability $\chi^{(2)}$ and molecular hyperpolarizabilities $\beta^{(2)}$

$$\chi^{(2)}_{xxz} = \chi^{(2)}_{yyz} = \frac{1}{2} N \left(\beta^{(2)}_{aac} \cos^2 \psi + \beta^{(2)}_{bbc} \sin^2 \psi + \beta^{(2)}_{ccc} \right) \cos \phi +$$

$$\frac{1}{2} N \left(\beta^{(2)}_{aac} \sin^2 \psi + \beta^{(2)}_{bbc} \cos^2 \psi - \beta^{(2)}_{ccc} \right) \cos^3 \phi$$

$$\chi^{(2)}_{zzz} = N \left(\beta^{(2)}_{aac} \sin^2 \psi + \beta^{(2)}_{bbc} \cos^2 \psi \right) \cos \phi - N \left(\beta^{(2)}_{aac} \sin^2 \psi + \beta^{(2)}_{bbc} \cos^2 \psi - \beta^{(2)}_{ccc} \right) \cos^3 \phi$$

$$(5.2)$$

with N being the surface density of PO_2^- groups. We assume that the interface is azimuthally isotropic. The values of the second order hyperopolarizability were taken from Ref. [231].

5.2.6 Calculation of the degree of asymmetry based on geometrical arguments

The number of lipids per leaflet can be calculated assuming that the liposomes have a spherical shape. We assume that each lipid headgroup occupies a constant area, a, which is the same at the inner and outer leaflets.[125] Then we get for the respective number difference (ΔN) between the outer leaflet and inner leaflet

$$\Delta N = \frac{4\pi \left(R^2 - (R-d)^2 \right)}{a}.$$

ΔN can be expressed as a percentage of the total lipid number density per liposome (N_{tot}), which is given by $N_{tot} = \left[4\pi \left(R^2 + (R-d)^2 \right) \right] / a$. Here, R is the outer radius of the liposome and d is the membrane thickness, for which we assume d ~ 5 nm in common agreement with literature results.[41,232]

5.2.7 Calculation of the degree of asymmetry from the SFS data

For a monodisperse solution the number densities ($N_{d,oil}$) of nanodroplets can be calculated by dividing the volume concentration of oil (V_{oil}) by the volume of one droplet with radius R_d

$$N_{d,oil} = \frac{V_{oil}}{\frac{4}{3}\pi R_d^3}. \tag{5.3}$$

For liposomes we have a spherical bilayer rather than a sphere with radius R_{lip} and thickness d and lipid volume concentration V_{lip}, so that the number density is different

$$N_{\text{d,lip}} = \frac{V_{\text{lip}}}{\frac{4}{3}\pi R_{\text{lip}}^3 - \left(R_{\text{lip}} - d\right)^3}. \tag{5.4}$$

To extract the degree of asymmetry for a certain vibrational mode, we fit the obtained spectra according to Eq. (5.1) and use the obtained amplitude $A_i(\theta)$ in the expression for α (Eq. (2.8))

$$\alpha_{\text{lip,i}}\left(\theta, R_{\text{eff,lip}}\right) = \frac{|A_i(\theta)|^2}{N_{\text{lip}} R_{\text{eff,lip}}^6} \tag{5.5}$$

This value is now independent of liposomes size, has been corrected for polydispersity, and can be compared to other samples. For droplets we obtain the same expression.

5.3 Results & Discussion

5.3.1 Single component liposomes

Starting with lipid hydration, Fig. 5.1a shows SHS patterns of single component liposomes made from DOPC, DPPC, and DPPS. The data is scaled to correct for the difference in number density and size of the scatterers (see section 2.2.2). The SH signal is non-zero, which indicates that for these ∼ 100 nm diameter liposomes the hydration environment of the inner leaflet is different from the outer leaflet. Also, charged DPPS liposomes generate ∼ 21× more intensity per liposome than the zwitterionic, neutral, liposomes. This difference arises because the electrostatic field of the headgroup charge affects the adjacent water molecules, which induces changes in the orientational distribution of the interfacial water molecules and hence increases the SHS intensity. This effect is absent for zwitterionic lipids. Thus, we observe a sizeable asymmetry in the distribution of water molecules that is particularly sensitive to charge. Differently oriented hydrating water molecules in the inner and outer leaflets agree with the finding from X-ray, neutron and dynamic light scattering that the electron density is asymmetrically distributed across the leaflets of anionic vesicles.[233] They also agree with the commonly employed assumption that the inner leaflet is considered charge neutral.[104]

Does such transmembrane hydration asymmetry require transmembrane lipid asymmetry as well? According to calculations assuming a spherical geometry and constant lipid headgroup areas[125] a number difference of 8 % should be present between the inner and outer leaflet of these liposomes (see 5.2.6). We can estimate the number difference of lipids per leaflet from SFS spectra, since SFS is sensitive to asymmetric orientations. In particular, assuming a homogeneous distribution of lipid
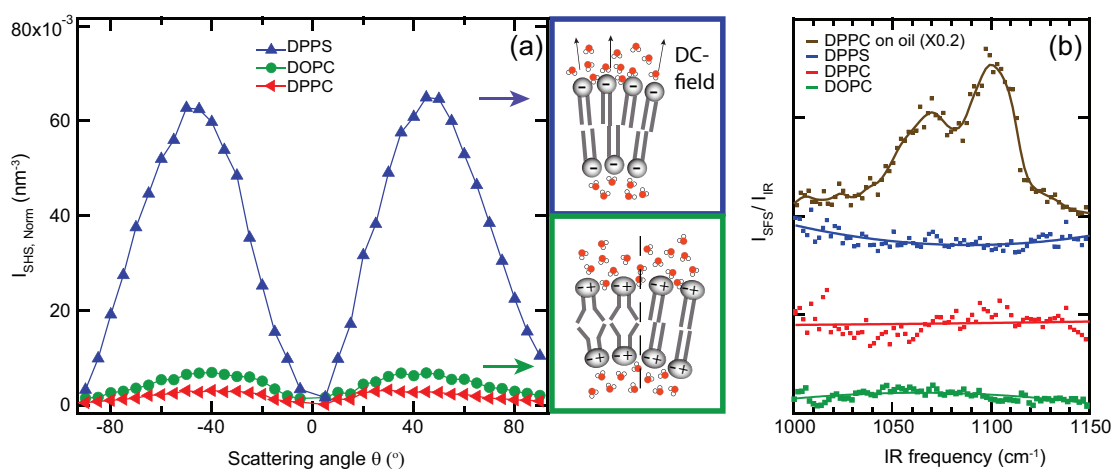
Figure 5.1: (a): SHS patterns measured with all beams polarized parallel to the scattering plane (PPP) of DPPS (blue), DOPC (green), and DPPC (red) liposomes in pure H_2O (extruded through a 100 nm pore). The scattering pattern originates from the overall transmembrane asymmetry in the orientational distribution of water molecules around the lipids (as illustrated in the cartoons). The data is scaled to correct for differences in size distribution and number density of the scatterers (as described in section 2.2.2. (b): SFS spectra of the same liposomes in D_2O in the P-O stretch region together with an SFS spectrum of hexadecane oil droplets covered with a DPPC monolayer (top trace). The spectra were collected with the IR (VIS, SF) beam polarized parallel (perpendicular) to the scattering plane (SSP). The SFS data are offset vertically for clarity.

molecules we can probe e.g. a lipid monolayer on an oil droplet. The detected SFS amplitude is proportional to the averaged projection of the molecular tilt angle to the interfacial normal, multiplied by the number of lipids in the probed area. For purposes of brevity we refer to this as the 'projected surface density'. For a liposome that has two oppositely oriented leaflets, the SFS amplitude reports on the transmembrane difference in the projected surface density. Therefore, to quantify transmembrane lipid asymmetry, we measured with SFS the headgroup intensity in the P-O stretch region of liposomes and relate it to the intensity of a DPPC monolayer on 100 nm hexadecane droplets in water. The molecular area per DPPC molecule is known to be 0.48 nm^2.[194] Knowing the area per lipid of the nanodroplet system, the size distribution of the droplets, and having a reasonable estimate of the average tilt angle of the P-N headgroup, we can compute the amplitude per lipid molecule, which can be used to derive a detection limit in terms of transmembrane lipid asymmetry. Assuming that the cross sections of the vibrational modes and average chain orientation are comparable, our previously derived detection limit,[234] can be converted to a lower limit for the detectable transmembrane number difference of ~ 2%.

Figure 5.1b shows SFS spectra of the same liposomes as in Fig. 5.1a in the P-O stretch region: Within the signal to noise ratio of our instrument we did not observe transmembrane lipid asymmetry. For the C-H modes the same result was obtained (not shown). Thus, the lipid number difference for these single component liposomes is under our detection limit, meaning that the projected surface density difference is below 2 %. Comparing this to the 8 % in transmembrane lipid asymmetry[125] that can be found from a computation considering constant headgroup areas independent of the leaflet, it appears that a different lipid hydration does not require transmembrane lipid asymmetry in terms of a different number of lipids in the inner and outer leaflet. Instead, other factors such as specific lipid-lipid intermolecular interactions may create the hydration asymmetry.[59] Such interactions would change the local (aqueous) environment of the lipids, which we can probe via the vibrational resonances of phospholipid headgroups in binary lipid mixtures.

The phosphate stretch mode is sensitive to the local environment. The s-PO_2^- stretch mode has been shown to be very sensitive to changes in intermolecular and H-bonding interactions as well as the local aqueous environment. The s-PO_2^- stretch mode can shift because of counterion interactions.[55,235] Dehydration of a DPPC monolayer on a planar air/water interface results in a ~10 cm^{-1} spectral shift of the s-PO_2^- mode to higher frequencies.[55] In order to verify that the s-PO_2^- stretch vibration is indeed a sensitive probe for changes in the local environment / lipid-lipid interactions, we have measured vibrational SFS spectra of hexadecane droplets covered with a dense monolayer of DPPC (analyzed in detail in Ref. [194]) and of DPPE (1,2-dipalmitoyl-*sn*-glycero-3-phosphoethanolamine). The DPPE headgroup is different from DPPC in that it lacks the CH_3 groups around the N atom in the headgroup (see Fig. 2.13). We expect that the amine and the phosphate group of DPPE interact through intermolecular interactions,[125] which also becomes obvious in an increase of the gel phase transition temperature from 314 K for DPPC to 336 K for DPPE. Figure 5.2a displays the SFS spectra for DPPC and DPPE covered hexadecane droplets in water. The DPPC monolayer spectrum contains two peaks, one at ~1070 cm^{-1}, assigned to the s-(C=O)-O-C stretch mode, and one at ~1100 cm^{-1} assigned to the s-PO_2^- stretch mode of DPPC in a hydrated monolayer.[194,236–238] The DPPE monolayer spectrum is different: it shows a single peak at ~1080 cm^{-1}. Based on the demonstrated sensitivity of the s-PO_2^- stretch mode on the local environment at the air/water interface, this peak likely originates from a population of H-bonded PE groups[12] resulting in red shifted s-PO_2^- stretch modes. Another advantage of the s-PO_2^- region is that the s-PO_2^- resonance is easily observable because there are no other modes. With this feature, we can obtain the orientational distribution of the headgroups. We use this mode as a probe to study transmembrane lipid asymmetry in liposomes composed of two different lipids. We start using binary mixtures of PS

lipids and another lipid with a different acyl chain length following studies of giant unilamellar vesicles with similar compositions.[231,239] These mixtures displayed phase separation behavior as a function of acyl chain conformation, and thus may exhibit a certain amount of transmembrane asymmetry.
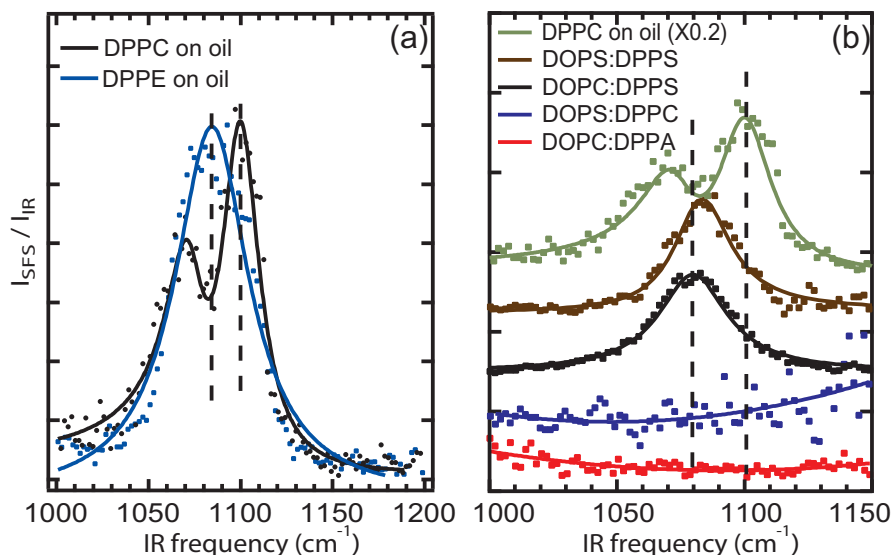
Figure 5.2: a: SFS spectra in the phosphate region of DPPC (black) and DPPE (blue) monolayers on oil nanodroplets at maximum lipid coverage measured using the SSP polarization combination. The dashed lines show the positions of the PO_2^- symmetric stretch modes in DPPC and DPPE. b: SFS (SSP) spectra taken in the P-O stretch region of ~100 nm diameter liposomes in pure D_2O composed of 1:1 mixtures of DOPS:DPPS (brown), DOPC:DPPS (black), DOPS:DPPC (blue) and DOPC:DPPA (red) and the P-O spectrum of the liquid condensed like DPPC monolayer (with known headgroup area) on oil droplets (green).

5.3.2 Liposomes from binary mixtures

Figure 5.2b shows SFS spectra of liposomes in the P-O stretch region composed of a 1:1 mixture of DOPC:DPPS, DOPS:DPPC, DOPS:DPPS and DOPC:DPPA. For comparison, we also plotted the P-O signal from the DPPC monolayer (green curve). The DOPC:DPPS liposomes generate a non-zero SF spectrum. Compared to the spectrum of the PC headgroups in a DPPC monolayer, there is a single peak at ~1080 cm^{-1}. Based on the comparison between DPPC and DPPE monolayers in Fig. 5.2a, the 1080 cm^{-1} mode is likely assigned to a population of H-bonded s-PO_2^- stretch modes. Liposomes composed of a 1:1 DPPC:DOPS mixture possess the same headgroup chemistry, but they will likely have a different packing. From Fig. 5.2b we see that these liposomes do not generate any detectable SFS intensity. Thus, in these mixtures all the lipid headgroups are distributed symmetrically across both leaflets (within the detection limit). We observe such a symmetric distribution also for other mixtures: DOPS:DOPC,

DPPS:DPPC mixtures (Fig. 5.3). Removing the amine group, but keeping the negative charge as in a DOPC:DPPA mixture also results in an absence of transmembrane asymmetry.
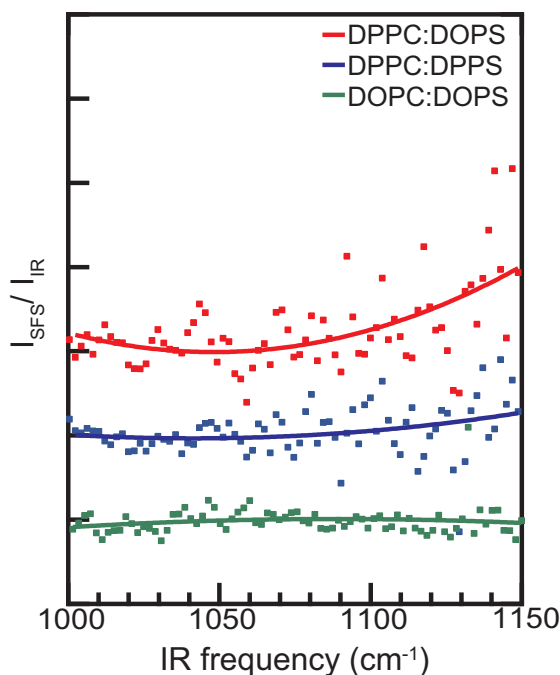
Figure 5.3: SFS spectra of mixtures of PC and PS lipids with different combinations of fatty acid tails: DPPC:DOPS (red), DPPC:DPPS (blue) and DOPC:DOPS (green).

The phosphate groups in the PA and PS headgroups are likely equally well hydrated. Hence, based on the observed differences in intensity, it appears that a charged lipid with a free amine group is crucial for the observed transmembrane asymmetry. We investigate this apparent PS specificity further by measuring single lipid DOPS liposomes and DOPS:DPPS liposomes. The former displays a comparable hydration asymmetry as DPPS, with no apparent transmembrane asymmetry (data not shown in Fig. 5.1). A 1:1 DOPS:DPPS mixture, however, which possesses the same headgroup chemistry and the same difference in fatty acid tail chemistry as the DOPC:DPPS liposomes displays transmembrane asymmetry (Fig. 5.2b). For this binary lipid mixture we observe the s-PO_2^- stretch mode at 1085 cm^{-1}, thus with a comparable frequency and intensity as for DOPC:DPPS liposomes. The measured PO_2^- modes represent the population of asymmetrically distributed phosphate groups between the leaflets. In the following paragraph, we formulate a hypothesis to rationalize where this PO_2^- signal originates from and how intermolecular interactions participate in this scenario.

5.3.3 Can lipid-lipid interactions drive transmembrane asymmetry?

As Fig. 5.2b shows, charged PS headgroups are crucial ingredients to establish trans-membrane asymmetry in the studied systems. PS headgroups possess oppositely charged phosphate, carboxylate and amine groups, which can each participate in H-bonding interactions with a neighboring lipid and with water.[59,220,240]we know that NH_4^+ ions as well as NH_3^+ groups interact with PO_4^- groups of neighboring molecules[26,28,240] (in the fashion illustrated in Fig. 5.4). However, as Fig. 5.1 shows, there is no transmembrane lipid asymmetry for pure DPPS liposomes indicating that an additional criterion needs to be satisfied. A difference in the fatty acid chain length and thus a specific packing appears to be necessary, as is also corroborated by the aforementioned studies on giant unilamellar vesicles.[231,239] Together with the result from the s-PO_2^- stretch mode - a red shift similar to the DPPE monolayers in which headgroup-headgroup H-bonding occurs - it seems likely that packing differences and intermolecular interactions are crucial here.
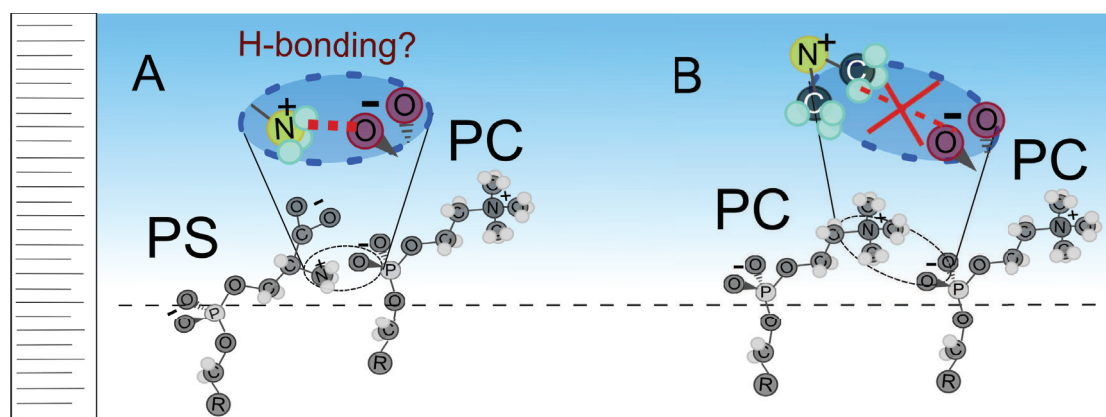
Figure 5.4: The H-bonding interaction between phospholipid headgroups is determined by the lipid structure and by the headgroup- and fatty acid tail chemistry. a: For a PS – PC pair the $H_2N\ldots O$-PO H-bond may be present depending on the distance between lipid headgroups (which can be changed by selecting proper combination of fatty acid tails). b: In contrast, for a PC – PC pair the headgroup chemistry is different and there is no possible intermolecular H-bonding.

Figure 5.4A and 5.4B illustrate one way that would explain the observed data: PS-PC headroups may interact through H_2N-H$\cdots$O-PO H-bonding, which would shift the vibrational frequency of the interacting phosphate groups (on the PC lipids) to a lower frequency. In doing so, they become SFS active. This interaction could, however, only occur if the probability of intermolecular interactions was increased (compared to the pure DPPS or DOPS liposomes). By changing the lipid tails from DO (18 C

atoms, one unsaturated bond) to the ~1 Å shorter DP tails[a] (16 C atoms, saturated) the distance between the H_2N-H and the O-PO groups is reduced facilitating more favorable intermolecular interactions[220] in a mixture of DOPC with DPPS, or DOPS with DPPS. Although this explanation agrees with the presented data, it will have to be investigated in more details e.g. by employing molecular dynamics simulations. Using this explanation and the C-H mode signal as a probe for lipid transmembrane asymmetry, and the phosphate stretch mode signal as a probe for (DOPC) lipids that are interacting with DPPS lipids, we quantify lipid transmembrane asymmetry and headgroup orientation differences between the leaflets in the DOPC:DPPS liposomes.

5.3.4 Quantification of transmembrane asymmetry

To determine the percentage of lipids that are asymmetrically distributed across the membrane, we use selective deuteration and measure SFS spectra in the C-H stretch mode region by targeting the lipid fatty acid tails. C-D modes vibrate at different frequencies so that we can determine the amount of hydrogenated lipids and thus the transmembrane asymmetry.

Figure 5.5a shows SFS spectra of liposomes in the C-H stretch region composed of a 1:1 mixture of d_{66}-DOPC:DPPS, and DOPC:d_{62}-DPPS. The top trace represents the C-H mode signal from the DPPC monolayer on oil droplets for comparison. There are the following peaks in the C-H mode region[24,26,241,242]: the s-CH_2 stretch mode (~2852 cm^{-1}, d$^+$), the s-CH_3 stretch mode (~2876 cm^{-1}, r$^+$), the antisymmetric (as-) CH_3 stretch mode (~2965 cm^{-1}, r$^-$), the s-CH_2-Fermi resonance (~2919 cm^{-1}, d^{+FR}), the s-CH_3-Fermi resonance (~2935 cm^{-1}, r^{+FR}) and the as-CH_2 stretch mode (~2905 cm^{-1}, d$^-$). The s-CH_3 stretch mode is dominant for the monolayer on droplets, which means that the alkyl chains are nearly all-trans in their conformation.[194] The liposomes with PS and PC mixtures display only a detectable SF response in the case of the d_{66}-DOPC:DPPS mixture, which indicates that only the DPPS molecules are immobile and asymmetrically distributed across the bilayer, and not the DOPC molecules (assuming that the deuteration procedure does not change any lipid properties, which is generally expected to be the case[242]). This is reasonable considering that DOPC molecules are in the liquid phase and thus are moving around due to thermal motion, wheras the DPPS molecules are in the gel-phase. The SF spectrum of the DPPS molecules shows a prominent peak at 2870 cm^{-1}, which corresponds to the s-CH_3 stretch mode, whereas barely a peak is visible at 2850 cm^{-1}, indicating an all-trans conformation of the tails (identical to that of DPPC). We thus assume that the DP acyl tail conformations are equal in both systems. Table 5.2 lists the extracted values for

---

[a]Although the mode at 1080 cm^{-1} could in principle be assigned to both modes, the s-(C=O)-O-C stretch mode is not involved in any lipid specific interaction, which means it is an unlikely candidate for the assignment.

the s-CH$_3$ stretch mode as shown in Fig. 5.5a.
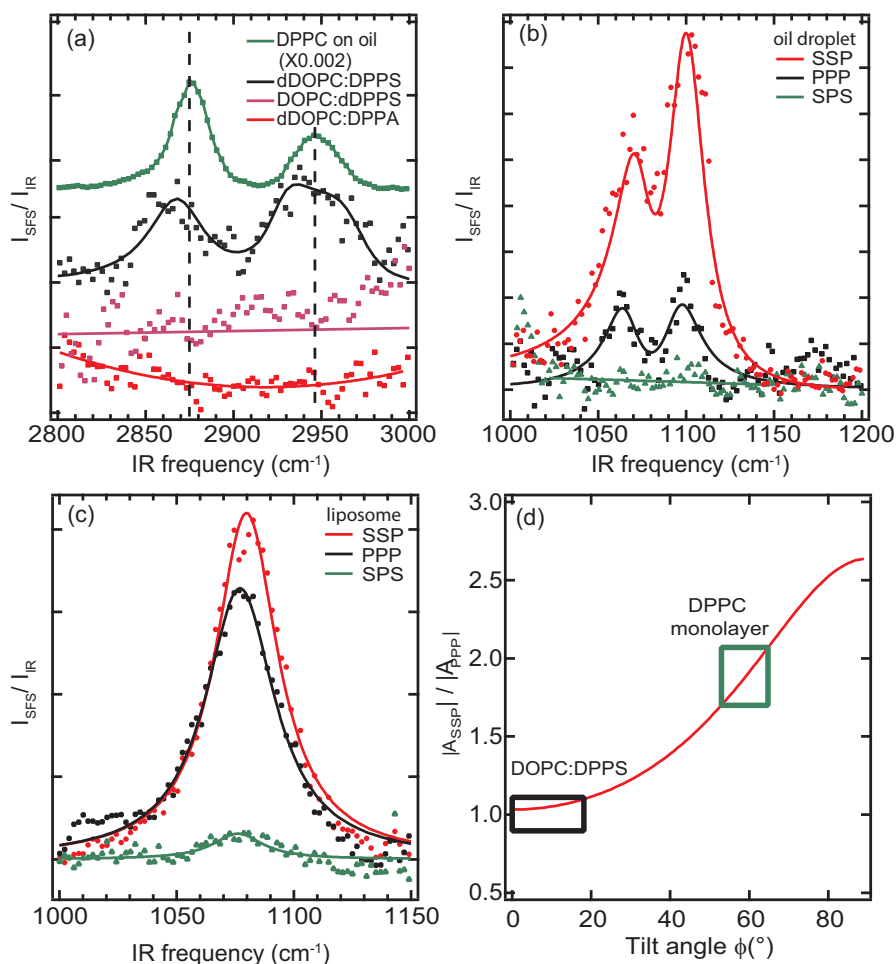
Figure 5.5: a: SFS (SSP) spectra taken in the C-H stretch region of ~100 nm diameter liposomes in pure water composed of 1:1 mixtures of d$_{66}$-DOPC:DPPS (black), DOPC:d$_{62}$-DPPS (purple) and d$_{66}$-DOPC:DPPA (red) and the spectrum of the DPPC monolayer on oil droplets (green). The solid lines represent fits to the data. The SFS data are offset vertically for clarity. b: SFS spectra of a DPPC monolayer on oil droplets, recorded in the SSP (red), PPP (black) and SPS (green) polarization combinations. c: SFS spectra of DOPC:DPPS liposomes in the SSP (red), PPP (black) and SPS (green) polarization combinations. d: dependence of the amplitude ratio of the SSP and PPP polarization combinations of the s-PO$_2^-$ stretch mode on the tilt angle. The boxes indicate the measured ratios obtained from the spectra of the oil droplets and DOPC:DPPS liposomes in panels (b) and (c) indicating the uncertainties from the amplitude fits of different samples.

Considering these values, we compare the obtained SFS intensity (α) of the s-CH$_3$ stretch mode for the d$_{66}$-DOPC:DPPS liposomes to that of the DPPC mono-layer. We find a transmembrane asymmetry in terms of the surface number density

ratio $\left(n_{\mathrm{lip,DPPS}}/n_{\mathrm{d}}\right)$ of

$$\sqrt{\frac{\alpha_{\mathrm{lip}}}{\alpha_{\mathrm{d}}}}(C-H) = \frac{n_{\mathrm{lip,DPPS}}}{n_{\mathrm{d}}} \tag{5.6}$$

in which α is scaled in order to be independent of the size of the droplet/liposome (see Eqs. (5.3)-(5.5)). We use Eq. (5.6) to determine the transmembrane asymmetry for DPPS: $n_{\mathrm{lip,DPPS}}/n_{\mathrm{d}} = 0.16$ (i.e. ~58 % of the DPPS molecules is located on the outer leaflet and ~42 % of the DPPS molecules is located on the inner leaflet, assuming similar sizes for DPPS and DPPC).

Table 5.2: Fitted frequency, amplitude and linewidth for the SFS spectrum of d_{66}-DOPC:DPPS liposomes in the CH region.

mode	ω_i[cm^{-1}]	Υ_i [cm^{-1}]	A_i
r^+	2868	20	0.15
d_{FR}^+	2926	16	0.11
r^-	2968	20	0.14
d^-	2906	20	0.02

From the polarization dependent spectra shown in Fig. 5.5b and Fig. 5.5c, we can estimate the orientational distribution $<\cos\phi_{\mathrm{d}}>$ ($<\cos\phi_{\mathrm{lip}}>$) of the asymmetrically distributed phosphate headgroups on the DPPC covered droplets and DOPC:DPPS liposomes. The angle ϕ represents the tilt angle of the symmetry axis of the s-PO$_2^-$ mode with the surface normal of the liposome or droplet. To determine $<\cos\phi_d>$, the orientational analysis for polarization resolved SFS[101,194] is extended to include a relationship between the second-order susceptibility and hyperpolarizability elements that uses a tilt (ϕ) and a twist (ψ) angle for the phosphate group. We follow here the procedure as introduced by the Allen lab.[231] Figure 5.5d displays the computed amplitude polarization ratio as a function of tilt angle for the s-PO$_2^-$ stretch mode for the case $\psi = 0$.[231] The fit parameters for the amplitude are given in Table 5.3. The rectangular areas in Fig. 5.5d indicate the experimentally measured scattering amplitude ratios from Fig. 5.5b and Fig. 5.5c considering the uncertainties of the amplitude fits for different samples. The phosphate groups of the DPPC molecules situated on oil droplets have an average tilt angle of $\phi = 60 \pm 10°$ with respect to the droplet surface normal. This value is in good agreement with the tilt angle found for DPPC molecules at the air/water interface.[231] For the liposomes, we find a tilt angle of $\phi = 10 \pm 10°$. Note that we assumed a narrow Gaussian distribution regarding the tilt angle and a uniform distribution of lipids for the analysis. The latter is expected[243]

because we have not detected any SFS signal in the PSP, PPS and SPP polarization combinations. Using a Gaussian distribution may not be completely justifiable because the number of participating lipids (several thousand) are not sufficient to make a statistical distribution.

Table 5.3: Fitted frequency, amplitude and linewidth for the SFS spectra in the phosphate region for the symmetric stretch (ss) mode for PO_2^- and C-O-P vibration.

Sample		DOPC:DPPS		DPPC on oil		DPPE on oil	DOPS:DPPS
Polarization		SSP	PPP	SSP	PPP	SSP	SSP
ss PO_2^-	A_i	1.13	1	1.85	1	1	1
	$\omega_i [\text{cm}^{-1}]$	1079	1079	1099	1096	1085	1083
	$\Upsilon_i [\text{cm}^{-1}]$	17	17	10	13	20	13
ss C-O-P	A_i			1.31	0.93		
	$\omega_i [\text{cm}^{-1}]$			1072	1066		
	$\Upsilon_i [\text{cm}^{-1}]$			20	12		

To estimate the percentage of DOPC molecules that interact with DPPS, we compare the s-PO_2^- mode amplitude of the DOPC:DPPS mixtures and the DPPC monolayer. We use the following expression

$$\sqrt{\frac{\alpha_{\text{lip}}}{\alpha_{\text{d}}}}(\text{P}-\text{O}) = \frac{n_{\text{lip,DOPC}} < \cos(\phi_{\text{lip}}) >}{n_{\text{d}} < \cos(\phi_{\text{d}}) >}. \tag{5.7}$$

The ratio $\sqrt{\frac{\alpha_{\text{lip}}}{\alpha_{\text{d}}}}(\text{P}-\text{O})$ represents the amplitude ratio of the s-PO_2^- mode of the lipids in the liposomes and the droplet monolayers (corrected for the difference in droplet/liposome number density and size distribution). This number reports only on the head groups that exhibit intermolecular interactions, and thus likely on DOPC molecules. The ratio $n_{\text{lip,DOPC}}/n_{\text{d}}$ represents the number density ratio of the interacting DOPC lipids in the liposomes compared to the DPPC number density on the droplets. $< \cos\phi >$ represents the orientational distribution as discussed in the previous paragraph. From Fig. 5.5a we have $\sqrt{\alpha_{\text{lip}}/\alpha_{\text{d}}}(\text{P}-\text{O}) = 0.9 \pm 0.3$. The factor $< \cos\phi_{\text{lip}} > / < \cos\phi_d >= 2$. From Eq. (5.7) we get $n_{\text{lip,DOPC}}/n_{\text{d}} = 0.45$. This means effectively that all the DOPC molecules in the outer leaflet are interacting with DPPS molecules. In this analysis we implicitly assumed that the inner leaflet is charge neutral.[104] This means that the Na$^+$ counterions are in close proximity to the PS headgroups (but likely not ion paired so that no frequency shifts are detectable[244]), it will result in a much lower probability for intermolecular H-bonding in the inner

leaflet between PS and PC headgroups.

Thus, from the analysis of the spectra in Fig. 5.2 and Fig. 5.5 (and relying on the interpretation in Fig. 5.4) we find that there is a lipid number difference of ~16 % of DPPS between the inner and outer leaflets. There is no detectable difference in the number of DOPC lipids between the outer and inner leaflets. The shifted s-PO$_2^-$ SFS response from the liposomes indicates that some of the DOPC molecules interact with DPPS through intermolecular H-bonding. Assuming charge neutrality in the interior, and a consequential lack of intermolecular H-bonds, we find that nearly all of the DOPC in the outer leaflet interacts with DPPS.

5.4 Conclusions

We find that charge and hydration transmembrane asymmetry is present in liposomes in aqueous solution, whereas for the same single component liposomes lipid transmembrane asymmetry is not detectable. Asymmetry in the number of lipids per leaflet can be induced by H-bond interactions between PS and PC/PS headgroups that depend on and can be influenced by varying the lipid structure. DOPC:DPPS liposomes exhibit a 16 % DPPS asymmetry but no detectable DOPC asymmetry. The P-O vibrational stretch mode intensity becomes clearly observable, indicating transmembrane asymmetry. This is related to a different orientational distribution of PC phosphate groups that participate in H-bond interactions with the PS amine groups. In particular, we find that the average orientational angle with respect to the surface normal of the phosphate group becomes close to 10° which is substantially different from the 60° that is found in a saturated monolayer.

The presence of lipid transmembrane asymmetry and probable underlying mechanism offer insights into the complexity of lipid membrane chemistry. If specific/chemical interactions lead to association of molecules in a 100 nm liposome, then it is likely that similar mechanisms can play a role in the formation and stabilization of lipid domains. Lipid rafts are considered to be dynamic structures > 40 nm in size that form and dissolve on ms timescales.[245] As such our work provides insights into how these domains might form. Future work that is geared at further understanding the link between the transmembrane asymmetry studied here and lipid raft structures might involve nonlinear scattering experiments performed in all polarization combinations, which is sensitive to structural heterogeneities.[243] These measurements should be performed on liposomes with a diameter of ~10 μm, to enable the formation of multiple domains and to obtain good signal to noise ratios. Given the importance of membrane properties and liposomes in basic biophysical research and biotechnology, our combination of SF and SH scattering techniques demonstrates a high potential to elucidate transmembrane asymmetry in lipid membranes. Particularly, these methods can be used to investigate lipid asymmetry induced by drug-membrane

or biomacromolecule-membrane interactions along with domain formation in lipid mixtures.

6 Characterization of the interface of binary mixed DOPC:DOPS liposomes in water: Charge condensation and curvature effects

Solutions of liposomes composed of binary mixtures of anionic dioleoylphosphatidylserine (DOPS) and zwitterionic dioleoylphosphatidylcholine (DOPC) are investigated with label-free angle-resolved (AR) second harmonic scattering (SHS) and electrokinetic mobility measurements. The membrane surface potential is extracted from the AR-SHS response. As a function of DOPS content, that is varied from 0 to 100 %, the surface potential changes from -10 to -145 mV and levels off already at ~10 % DOPS content. The ζ-potential shows the same trend but with a drastically lower saturation value (-44 mV). This difference is explained by the formation of a condensed layer of Na^+ counterions around the outer leaflet of the liposome as predicted by charge condensation theories for polyelectrolyte systems. A very similar behavior is observed for DOPC:cardiolipin membranes and NH_4^+ counterion.

6.1 Introduction

Lipid bilayer membranes are the primary building blocks of organisms. These membranes exhibit a diverse composition in order to separate functional compartments and to control signalling processes. In plasma membranes the lipid composition between the two leaflets is highly asymmetric and changes dynamically to trigger environmental responses. For instance, cells that undergo apoptosis concentrate anionic phosphatidylserine (PS) in the outer leaflet of the plasma membrane to signal phagocytes to approach and digest them, whereas in healthy cells PS lipids are only present in the inner leaflet.[246]

In order to understand membrane structure, hydration, and the changes therein it is crucial to characterize the interfacial properties of lipid membranes and their aqueous environment. Non-resonant second harmonic scattering[120,152] (SHS) is an optical process used to probe the net orientational order of water molecules along the surface normal of a particle,[106,118,175,178] droplet,[32,178,179] or liposome.[104,192] We recently demonstrated that polarization- and angle-resolved (AR) SHS represents a method to obtain a unique value for the surface potential of a particle in aqueous solution.[247] As we have seen earlier in this thesis, we can describe scattering patterns by exact analytical expressions[155] that rely on the surface potential and one non-vanishing surface susceptibility tensor element. Therefore, two independent scattering patterns are sufficient to retrieve unique values for both parameters. Applying AR-SHS in combination with sum frequency scattering (SFS) to probe the transmembrane asymmetry in single component anionic DOPS and zwitterionic DOPC liposomes, which in pH neutral conditions are either charged (DOPS) or neutral (DOPC). We found that the molecular trans-membrane asymmetry originates from a disparity in the amount of hydrating water molecules that surrounds the phospholipid headgroups (see chapter 5). We did not find transmembrane asymmetry in the form of a different number of lipid molecules in the inner and outer leaflets.

In this chapter, we quantify the surface properties of liposomes in water that are composed of a binary mixture of phosphocholine and phosphoserine, which are the two main constituents of the eukaryotic plasma membrane.[4] We apply AR-SHS and electrokinetic mobility measurements to dilute solutions of liposomes composed of different binary mixtures of DOPS and DOPC, spanning the full range of possible mixtures. The membrane surface potential is extracted from the AR-SHS response. Upon increasing the amount of DOPS in the membrane, the surface potential changes from -10 ±20 mV to -145 ±30 mV and levels off at ~10 % DOPS. The ζ-potential shows the same trend but with a drastically lower saturation value (-44 mV). This observation is explained by the formation of a condensed layer of Na$^+$ counterions around the outer leaflet of the liposome and agrees with predictions of charge condensation theory for polyelectrolyte systems. Size dependent SHS measurements show that the

relative (size normalized, single liposome response) increases for smaller liposomes indicating that the difference in the amount of headgroup hydrating water between the inner and outer leaflet increases for smaller liposomes.

6.2 Materials & Methods

6.2.1 Chemicals

Sulfuric acid (95-97 %, ISO, Merck), ammonium hydroxide (30 %, Sigma-Aldrich), hydrogen peroxide (30 %, Reactolab SA), chloroform (Emsure, ACS, ISO, Merck) and sodium chloride (NaCl, >99 %, Sigma-Aldrich), phosphorus standard solution (0.6 M, Sigma-Aldrich), L-ascorbic acid (ACS, ≥ 99 %, Sigma-Aldrich), ammonium molybdate (VI, ACS, 81-83 %, Sigma-Aldrich), and hexadecane (>99.8 %, Fluka) were used as received. 1,2-dioleoyl-*sn*-glycero-3-phosphocholine (DOPC) and 1,2-dioleoyl-*sn*-glycero-3-phospho-L-serine (sodium salt) (DOPS), were purchased in powder form (>99 %) from Avanti Polar Lipids (Alabama, USA) and stored at -20 °C until further use.

6.2.2 Cleaning procedures

Glassware was cleaned with a 1:3 H_2O_2:H_2SO_4 solution and rinsed with ultrapure water (Milli Q, Millipore, Inc., electrical resistance of 18.2 MΩ cm). The glassware for the phosphate assay required a two-step cleaning procedure: First a cleaning with a 3:1:1 H_2O:H_2SO_4:H_2O_2 solution at 100 °C was done, which was followed by a cleaning with a 3:1:1 H_2O:NH_4OH_4:H_2O_2 solution at 80 °C, each for 10 minutes. After and in between the cleaning steps the glassware was thoroughly rinsed with ultrapure water.

6.2.3 Liposomes

The liposomes were found to have a mean diameter in the range of 94 - 110 nm with a polydispersity index (PDI) of less than 0.1.

6.2.4 SHS

SHS patterns were recorded with an angle of acceptance of 3.4° in steps of 5°, whereas single angle measurements were recored with an angle of acceptance of 11.4°.

6.3 Results & Discussion

6.3.1 DOPC:DOPS membranes

Figure 6.1a and 6.1b show the measured SH scattered intensity from liposomes as a function of scattering angle θ for the two polarization combinations (PPP and PSS) for three different DOPC:DOPS ratios. Figure 6.1c shows the maximum scattered intensity (at $\theta = 50°$) as a function of DOPS concentration in the liposome. The SH intensity, which is directly linked to the orientational order of interfacial water molecules,[155] in-

creases with an increasing amount of DOPS molecules in the membrane, but saturates at ~10 % (*w/w*) DOPS content.
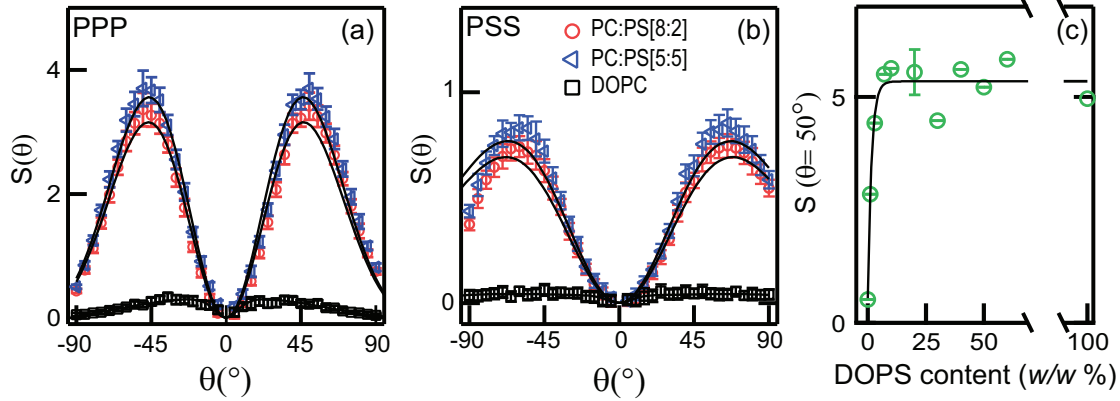
Figure 6.1: (a) SH scattering patterns in the PPP polarization combination. (b) SH scattering patterns in the PSS polarization combination. The lines represent fits made to the nonlinear Rayleigh-Gans-Debye theory from which the surface potential values were extracted using the parameters of Table 6.1 (c) Maximum SH intensity as a function of DOPS weight percentage in the liposomes (in the PPP polarization combination). The solid line is a guide for the eye.

To understand the saturation behavior in more detail we analyzed the data in Fig. 6.1a and 6.1b determining the surface potential as listed in detail in chapter 4 and quantifying the degree of ionization afterwards. The solid lines in Fig. 6.1a and 6.1b represent fits to the nonlinear light scattering equations (Eqs. (4.3)) that were made using for the surface susceptibility element $\chi_{s,2}^{(2)} = 1.36(\pm 0.2) \times 10^{-22}$ m^2/V and surface potential values that range from $\Phi_0 = -10 \pm 20$ mV (pure DOPC) to $\Phi_0 = -145 \pm 30$ mV (pure DOPS). The obtained values for Φ_0 are plotted in Fig. 6.2a. From previous measurements (see chapter 4) we knew that the value does not significantly differ between pure DOPC and DOPS liposomes and therefore we kept it constant.

The maximum magnitude for Φ_0 is reached at ~10 % *w/w* of DOPS in the liposomes. The values for Φ_0 can be compared to measured ζ-potential values (Fig. 6.2b) that were extracted from electrokinetic mobility measurements of the same samples. The ζ-potential follows the same trend as the surface potential: The magnitude of the ζ-potential increases with increasing DOPS concentration and levels off at ~10 % DOPS. At higher concentrations the ζ- potential remains constant at -44 ± 7 mV, independent of the DOPS concentration. The saturated values of Φ_0 and ζ differ significantly, by ~100 mV. We analyze this difference to obtain insight into the molecular level structure of the interfacial layer. To estimate the behavior of the electrostatic potential and the amount of free charges on the DOPS headgroups, we need to assume a model for the structure of the interfacial region. Assuming an arbitrary sized smooth sphere with a certain surface charge density σ_0 that is embedded in a continuous medium with a 1:1 electrolyte concentration *c*, we can compute both

Table 6.1: Input parameters and fit values for scattering patterns from mixed DOPC:DOPS liposomes.

Parameters	DOPC	PC:PS [9:1]	PC:PS [8:2]	PC:PS [7:3]	PC:PS [6:4]	PC:PS [5:5]	DOPS
Hydrodynamic radius [nm]	47	56	56.9	57.5	58.4	57.6	59
Headgroup area [nm^2]	0.725[a]	0.71	0.71	0.7	0.696	0.689	0.65[a]
Number density (N$_p$) $\times 10^{-12}$ [#/ml]	3.3	3.59	3.43	3.23	2.92	3.21	2.87
R.I.$_{particle}$ (514 nm) [b]	1.4	1.4	1.4	1.4	1.4	1.4	1.4
R.I.$_{solution}$ (514 nm)	1.33	1.33	1.33	1.33	1.33	1.33	1.33
Temperature [°C]	24	24	24	24	24	24	24
Ionic Strength [mM]	0.0022	0.092	0.138	0.148	0.141	0.121	0.246

[a] Taken from [55].
[b] Adapted from [201].

the surface charge density σ_0 and the decay of the electrostatic potential into the solution $\Phi(r)$ for a given value of Φ_0. Using Ohshima's exact solution for the potential distribution around a sphere with arbitrary potential, we have[127]

$$\Phi(r) = \frac{2k_B T}{ze} \ln \left[\frac{1 + \tanh\left(\frac{ze\Phi_0}{4k_B T}\left(\frac{R}{r}\right)e^{-\kappa(r-R)}\right)}{1 - \tanh\left(\frac{ze\Phi_0}{4k_B T}\left(\frac{R}{r}\right)e^{-\kappa(r-R)}\right)} \right] \tag{6.1}$$

and

$$\sigma_d = \frac{2\epsilon_0 \epsilon_r \kappa k_B T}{e} \sinh\left(\frac{ze\Phi_0}{2k_B T}\right) \times$$
$$\sqrt{1 + \frac{1}{\kappa R} \frac{2}{\cosh\left(\frac{ze\Phi_0}{4k_B T}\right)^2} + \frac{1}{(\kappa R)^2} \frac{8\ln\left[\cosh\left(\frac{ze\Phi_0}{4k_B T}\right)\right]}{\sinh\left(\frac{ze\Phi_0}{4k_B T}\right)^2}}. \tag{6.2}$$

Figure 6.2c shows the computed potential decay using Eq. (6.1) (dashed blue curve). The dashed black line indicates the ζ-potential. As we have seen in the previous chapters, the ζ-potential is the potential that is measured at the boundary between stagnant and free flowing liquid positioned at a distance d away from the surface.[66,135] This plane is thought to be positioned not more than ~3 water diameters (< ~1 nm) away from the interface of an atomically smooth surface.[248] In our samples there

will be some variations in the positions of the lipids as they are in the liquid phase, exhibit thermal motion, and the liposome surface is not atomically smooth. This could lead to variations on the order of ~1 nm, but certainly not more.[249] Applying Eq. (6.1) to the found values of Φ_0 and determining where the $|\zeta|$-potential crosses the $\Phi(r)$-curve results in a slipping plane distance of d= 20 nm. This is physically
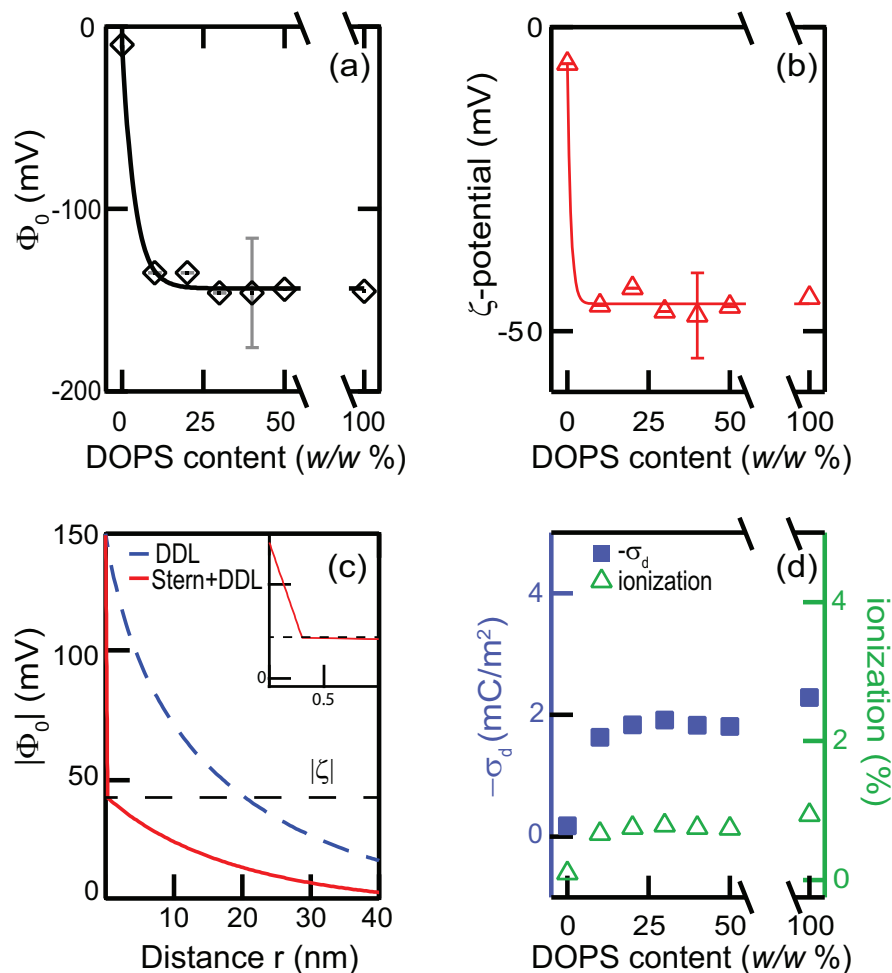
Figure 6.2: (a) Extracted surface potential values from the data in Fig. 6.1a and 6.1b with an indication of propagated uncertainties of the input parameters ($\chi_2^{(2)}$, ionic strength, radius, number density, and dielectric constant).(b) Measured ζ-potential values for the same samples used in panel (a). The error bars represents the standard deviation after 75 measurements. Solid lines are guides to the eye.(c) Computed values for the electrostatic potential as a function of distance (r, r=0, r=R) along the surface normal for a diffuse electric double layer only (labeled DDL, dashed blue curve) and a Stern layer with a diffuse double layer (solid red curve). The inset shows a zoom-in for 0<r<1 nm.(d) The computed surface charge density σ_d at the shear plane (solid blue squares) and the overall degree of ionization(open green triangles) of the liposomes as a function of DOPS content.

unrealistic: It does not seem energetically meaningful to have a layer of 60 stagnant water molecules. According to the available knowledge that the slipping plane is at a distance d < 2 nm the potential difference $|\Phi_0 - \zeta|$ should occur over a distance d < 2 nm here, which requires a significant electrostatic field strength of $> 4.9 \times 10^7$ V/m. In case d=0.3 nm (which corresponds to one layer of water molecules and is the lower limit o the slipping plane distance[67,250]) the field strength becomes 3×10^8 V/m. If an electrostatic field with such a high strength emerges from the surface, it will result in a high concentration of counterions. This hints towards a low degree of completely ionized surface headgroups and the presence of a kind of Stern-like layer or charge condensation at DOPS concentrations exceeding 10 %, even though the ionic strength of the solution is low. With that expectation in mind, the potential distribution from the shear plane into the solution should be modified by replacing Φ_0 with ζ and the very proximity to the membrane can be represented by a constant capacitor model.[66,208] The resulting estimated distance dependent potential is plotted in Fig. 6.2c. Using the ζ for Φ_0, the charge density σ_d on the shear plane is then determined by Eq. (6.2). Values for σ_d (solid blue squares, left axis) and the corresponding degree of ionization on the liposomes outer leaflet (σ_d/σ_0, open green triangles, right axis) are plotted in Fig. 6.2d. For this calculation we used a σ_0 calculated with effective headgroup areas[55] ranging between 0.653 nm^2 and 0.713 nm^2 for DOPS and DOPC:DOPS[9:1] liposomes(6.1). The degree of ionization as calculated on the shear plane is almost constant around 1 % indicating that almost all charges are screened within the first few hydration shells. This means that in 100 % DOPS liposomes only 1 in 100 DOPS molecules have no counterions associated with them and for liposomes with 10 % DOPS this amounts to ~1 in 10 lipids. This level of counterion condensation would require a total effective interfacial Na$^+$ concentration in the order of 1 - 3 M (assuming the lipid headgroup area and thickness of the condensed layer as mentioned above).

The observed large difference between the surface and the ζ-potential as well as the independence of both potentials on the surface charge density are clear indicators of some form of charge condensation at the outer leaflet of the liposomes. Charge condensation[251] is more commonly observed in polyelectrolyte solutions (Ref. [252] and references therein) and some colloidal systems.[253,254] This condensation occurs in solutions of low ionic strength as a consequence of free energy minimization originating from electrostatic enthalpic interactions favouring association and entropic interactions favouring dissociation.[255] We can calculate the critical surface charge density $(\sigma_{0,\mathrm{crit}})$ above which charge condensation occurs for spherical particles with sizes that are comparable to the Debye length ($1/\kappa, \kappa R \sim 1$) according to[255]

$$\sigma_{0,\mathrm{crit}} = \frac{e\,(1 + \kappa R)\ln(\kappa l_b)}{2\pi R z l_b} \tag{6.3}$$

in which κ is again the Debye screening parameter ($\kappa = \sqrt{\frac{2000 e^2 z^2 N_A c}{\epsilon_0 \epsilon_r k_B T}}$, c the respective concentration (in mol/l), R the radius of the liposome, l_b the Bjerrum length in water (0.71 nm) and z the valency (1). For the liposome solutions, we obtain $-7.9 < \sigma_{0,\text{crit}} < -6.7$ mC/m^2. A theoretical maximum surface charge density of 100 % (10 %) DOPS liposomes is $\sigma_0 = -245$ mC/m^2 (-22.5 mC/m^2) considering 1 charge per headgroup and the same headgroup areas as before (see Table 6.1). These values for the surface charge density are much larger than the computed critical value above which charge condensation occurs. Based on Eq. (6.3) we can infer that condensation would start around 3 % of DOPS in the liposome, which is in reasonable agreement with our data considering our error bars.
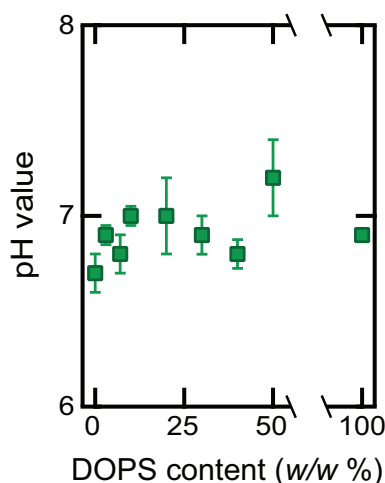
Figure 6.3: Variation in the bulk pH of DOPC:DOPS liposome solutions as a function of DOPS content. The pH was derived from three consecutive potentiometric measurements. Error bars indicate the standard deviation of three measurements.

One question one might ask is if the ions that are responsible for the charge condensation consist of Na$^+$ ions or H$^+$ ions from the autoprotolysis reaction of water. If H$^+$ is responsible for the condensation of charge, given the amount of charge condensation (99 %) and the number of liposomes in the solution ($\sim 2.87 \times 10^{12}$ cm^{-3}) for the liposomes with 100 % DOPS, we may expect a change of the bulk pH value to pH = 10.4. A potentiometric measurement of the pH as a function of DOPS concentration did not show any changes (see Fig. 6.3). As such the condensed layer most likely consists of Na$^+$ ions. This finding is also in agreement with computer simulations, which, when modelling bilayer interfaces, obtain a high density in counterions around the bilayer headgroups.[59,235,236]

6.3.2 DOPC:cardiolipin mixtures

To investigate whether the observed effect is a DOPS specific phenomenon, we altered the membrane composition using different ratios of DOPC:cardiolipin. Cardiolipin is also anionic, but much more bulky compared to DOPS being composed of 4 fatty acid chains and 2 phosphate groups (see Fig. 2.13). Cardiolipin carries an NH_4^+ counterion instead of Na^+. The ratio between the charged moieties and fatty acid chains is the same for both lipids and hence the achievable surface charge density is approximately equivalent. Figure 6.4 shows the SH intensity measured at the angle of maximum intensity $\theta = 50°$ in the PPP polarization combination as a function of cardiolipin content. The overall trend in the SHS intensity resembles the one shown in Fig. 6.1c. The SH signal and the zeta potential saturate both at 9:1 % (*w/w*) ratio, indicating that the observed saturation purely originates from electrostatic influences and not from specific interactions (as was the case in chapter 5).
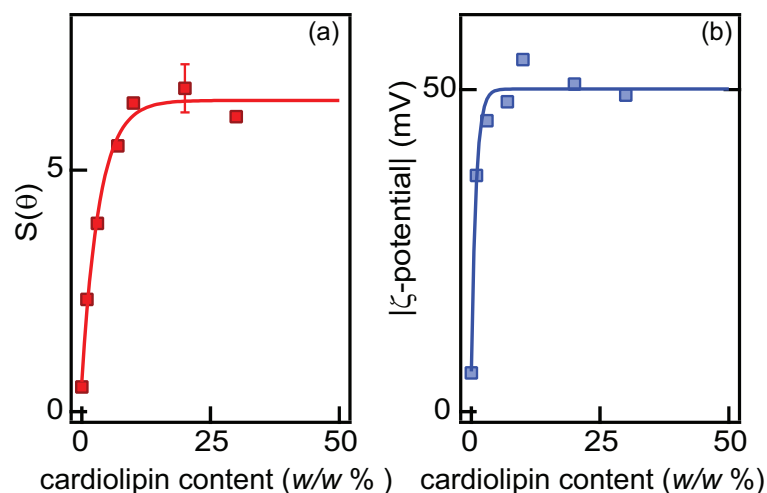
Figure 6.4: (a) SHS intensity at $\theta = 50°$ of DOPC:cardiolipin liposomes as a function of cardiolipin content in the PPP polarization combination. Solid lines are guides to the eye. (b) Absolute ζ-potential of the same liposomes.

6.4 Conclusions

We characterized DOPC:DOPS liposomes with AR-SHS as a function of lipid composition and size. The polarization state resolved AR-SHS response is an indicator for the amount of orientationally ordered water, which is used to extract the membrane surface potential. As the DOPS membrane content is varied from 0 to 100 % the surface potential changes from -10 to -145 mV at a few percent of DOPS in the membrane after which it remains constant. The ζ-potential shows the same trend but has a drastically lower saturation value (-44 mV). The big potential difference and the absence of sensitivity of both potentials on the amount of charged lipids in the mem-

brane is explained by the formation of a condensed layer of Na^+ counterions around the liposome. This explanation agrees well with predictions of charge condensation theory for polyelectrolyte systems. Size dependent SHS measurements show that the relative, size normalized, single liposome response increases for smaller liposomes indicating that the difference in the amount of headgroup hydrating water between the inner and outer leaflet increases for smaller liposomes.

The presented experimental findings demonstrate that the Gouy-Chapman model, despite its wide use,[58,256–258] is not suitable without modification for the description of the diffuse double layer around lipid membranes, even under conditions of low ionic strength. Specifically, the relatively strong association of counterions with interfacial charged groups, independent of the lipid, needs to be considered. In addition, from a purely theoretical angle there is still an ongoing discussion about ion behaviour at charged interfaces at high concentrations, for which different scenarios from simulations exist,[168] but also at low concentrations, for which very little data exists. The present data will help to select the correct way to describe theoretically the composition and physical chemistry of membranes in terms of ion distribution.

7 Summary & Outlook

7.1 Summary

In this thesis, we used second harmonic scattering to characterize lipid membranes and their aqueous environment by accessing the interfacial structure experimentally. In the first part of this thesis we generalized the nonlinear optical theory to describe interfaces in aqueous solutions independent of the ionic strength. Subsequently, we verified the correctness of the derived theory experimentally. In the second part, we used this generalized theory to characterize different lipid membranes. We determined the surface potential of various lipid membranes in different aqueous solutions by analyzing the water orientation. We compared this approach with well-established models and analyzed the electrostatic interactions in membranes by quantifying the effective surface charge density and headgroup hydration. This thesis represents one of the first systematic label-free studies of free floating lipid membranes.

In particular, in chapter 3 we generalized the existing nonlinear optical theory to be able to describe the second-order optical response originating from planar and curved interfaces correctly. Although the nonlinear optical theory for scattering in aqueous solutions for high ionic strength existed already, it is now possible to describe the SH and SF signal over the full range of theoretical available ionic strengths from 10^{-7} to 10^{1}. The nonlinear optical techniques SFG and SHG are known to be surface sensitive. At low ionic strength the probed interfacial region can be up to 1 µm deep. The detected signal can be affected by interfering photons generated at water molecules within this depth. This observation helps to clarify differences in the existing literature that used various equations despite different measurement geometries or unsuitable experimental conditions. The described effect has a significant impact on the interpretation of ion-surface interactions measured with SF or SH measurements and is applicable to planar as well as spherical interfaces.

Using the generalized theory and the hyperpolarizability of the main liquid (water) as reference, it is now possible to determine unique surface potential values from scattering patterns of aqueous colloidal suspensions. This determination does

not require assumptions about the surface structure beyond azimuthal isotropy nor does it require the use off a mean-field model for the interfacial chemistry (chapter 4). We determined the surface potential of bare hexadecane droplets in water (pH= 8) and zwitterionic DOPC liposomes, as well as anionic DOPS liposomes in different ionic strength. In agreement with their respective surface charges, hexadecane droplets and DOPC liposomes have barely a surface potential, whereas the anionic DOPS membranes revealed surface potentials between ~ -150 mV (100 µM ionic strength) and -23 mV at 10 mM ionic strength. We also found that the non-zero element of the second order susceptibility $\chi^{(2)}_{(2)}$ is almost constant leading to the conclusion that a similar orientational distribution of interfacial water molecules must exist on these different surfaces. This method is applicable to small sample volumes, dilute particle concentrations, particle sizes $>$ 25 nm, and not restricted to the chemical nature of the dispersion – as long as there is no bulk response from the particle. Summarizing, it represents a distinct, portable, optical, label-free probe of surface potentials without using models for the interfacial chemistry.

In chapter 5, we focused on intermolecular interactions within the membrane and how these may affect the membrane structure as well as the hydration. There is a hydration asymmetry between the inner and outer leaflet, but for most lipid mixtures there is no lipid transmembrane asymmetry observable indicating a very dynamic molecular lipid layer. However, gel-phase DPPS lipid molecules did not mix homogeneously with zwitterionic liquid-phase DOPC molecules forming bilayers, but distribute asymmetrically over the leaflets. H-bonds between the headgroups of these two types of lipids seems to be supported by geometrical factors, such as the length of the hydrocarbon chain and the lipid packing density. These findings show that combined SHS and SFS experiments can also contribute to fundamental discussions about the structure of the membrane. In particular, ongoing debates about the occurrence of lipid rafts and domain formation could be solved with the appropriate experiments using SHS and SFS.

In chapter 6 we determined the counterion association to anionic lipid membranes experimentally. We showed that almost independent of the lipid concentration, anionic liposomes have a very low surface charge (1 %) and a high counterion association even in pure water. Typical interfacial models that depend on the ionic strength of the solution, such as the Gouy-Chapman model, may not correctly describe the interfacial chemistry. It is absolutely necessary to consider binding constants and the presence of the respective ions, even at very low ionic strength. The ion behavior is in agreement with predictions of condensation theory in polyelectrolyte systems. The presented findings are helpful for ongoing theoretical discussions about ion-surface association behavior at high and low ionic strength.

7.2 Outlook

In this thesis, we demonstrated the possibilities of polarization and angle-resolved nonresonant SHS to characterize the inter- and intramolecular interactions and hydration structures of lipid membrane interfaces.

We advanced the theoretical description of nonlinear light scattering experiments to describe scattering patterns in any ionic strength solutions and to quantify the surface potentials of dispersed particles. The here presented method can be adapted to consider a wide range of molecular species enabling one to extract surface potentials, label-free and interface model-free, from any type of dispersion. Our polarimetric AR-SHS method is thus applicable to dispersions in different media such as ionic liquids and non-aqueous particle solutions. The sole requirement would be the knowledge of the molecular hyperpolarizability elements of the solvent. As such, the presented algorithm is very valuable for interfacial electrostatic interactions of colloids in non-aqueous media. Another requirement is that the method is nonresonant, but this can, in theory, be overcome by extending the model. We therefore expect that the method can be employed to several systems such as metal oxide particles, e.g. silica or polymer beads. These particles are of great importance in modern applications due to their high surface to volume ratio, surface modification possibilities and structural diversity, which affect the interaction with the environment. These kind of particles can be found in sensing and separation applications, gas storage, catalysis, ceramic production and as cancer treatment. Especially for characterizing the surface properties of such solid nanoparticles, an interesting approach would be a comparison study together with X-ray photoelectron spectroscopy (XPS). Using SHS, the surface potential is determined probing the water orientation at the interface, whereas studies using XPS claim to extract surface potentials directly from probing the change in binding energies in the material. Hence, one could obtain complementary information from the material and the interfacial environment using both methods together in a variety of solvents.

In terms of membrane biophysics/chemistry, this work represents a first systematic characterization of lipid membranes and intermolecular interactions on a molecular level in label-free conditions with the nonlinear optical technique SHS. Characterizing the hydration structure and the ionization around lipid membranes will help to shed light on the molecular interactions in membrane related processes, e.g. protein-membrane interactions label-free and in real time. As demonstrated in this thesis, SHS is exclusively sensitive to the hydration structure so that, for instance, the hydration of the protein in the aqueous solution alone could be characterized and how this hydration affects the respective membrane kinetics. The choice of the protein here is not limited but exclusively dependent on the molecular information one wants to obtain. Very likely possibilities include phospholipase kinetics altering

free-floating membranes, aggregation of amyloids on lipid bilayers, or kinetics in lipid related signaling. The phosphorylation of the lipid phosphoinositide by the phosphoinositide 3-kinase could be a very likely and interesting target for the here presented techniques as well. Phosphoinositide is known to participate in several signaling pathways; a combined approach similar to chapter 5 could therefore be an interesting approach to determine the different phosphate orientations of the inositide in combination with its hydration properties. This represents only a small degree of possible approaches. The work of this thesis demonstrates that biotechnological studies but also very fundamental questions could be equally well addressed with these nonlinear optical techniques.

8 Appendix

8.1 $\beta^{(2)}$ to $\chi^{(2)}$ transformation

We follow here the description of De Beer *et al.*,[100,101,122] considering the simplifications listed in Ref. [89]. As stated shortly in chapter 1, 3, and 4,the second harmonic response originates from the induced molecular dipoles due to an illumination with an optical field. The second-order polarizability of a molecule is captured in the molecular hyperpolarizability $\boldsymbol{\beta}^{(2)}$. The various non-vanishing tensor elements of $\boldsymbol{\beta}^{(2)}$ depend on the molecular symmetry of each molecule. In analogy to (3.1), the molecular second-order polarization p_i of a molecule is

$$\mathbf{p}_i = \beta^{(2)} : \mathbf{EE} \tag{8.1}$$

To express the polarization macroscopically, that is relative to an interface as done in chapter 3, one needs to transform the molecular hyperpolarizability to the surface susceptibility considering the orientational distribution of all interfacial molecules so that

$$\chi_{ijk}^{(2)} = N_s \langle T_{ia} T_{jb} T_{kc} \rangle \beta_{abc}^{(2)}. \tag{8.2}$$

The subscripts *i,j,k* and a,b,c represent the directions in the respective coordinate system, either the surface coordinate frame or the molecular coordinate frame. N_s represents the number density of the interfacial molecules. *T* is the transformation matrix. The transformation is typically a rotation around the molecular axis, a tilt by an angle with respect to the surface normal, and another rotation around the surface normal. The transformation requires certain assumptions to yield an unambigious solution. With the assumption of rotational isotropy at the interface and nonchiral molecules, only the tilt angle ϕ determines the $\boldsymbol{\chi}^{(2)}$ components. This results in only 4 independent $\chi^{(2)}$ elements for spherical scatterers for which the transformation can

be written as

$$
\begin{pmatrix} \chi_1^{(2)} \\ \chi_2^{(2)} \\ \chi_3^{(2)} \\ \chi_4^{(2)} \end{pmatrix} = \frac{N_s \langle \cos\phi \rangle}{2} \begin{pmatrix} (5D-3) & 0 & 0 & 0 \\ (1-D) & 2 & 0 & 0 \\ (1-D) & 0 & 2 & 0 \\ (1-D) & 0 & 0 & 2 \end{pmatrix} \begin{pmatrix} \beta_1^{(2)} \\ \beta_2^{(2)} \\ \beta_3^{(2)} \\ \beta_4^{(2)} \end{pmatrix} \tag{8.3}
$$

and

$$
D = \frac{\langle \cos^3\phi \rangle}{\langle \cos\phi \rangle}.
$$

Here, the χ^2 elements are defined as already given in section 3.2.3; $\beta_1^{(2)} = \beta_{ccc}^{(2)} - \beta_2^{(2)} - \beta_3^{(2)} - \beta_4^{(2)}$, and $\beta_2^{(2)} = \left(\beta_{aac}^{(2)} + \beta_{bbc}^{(2)}\right)/2$, $\beta_3^{(2)} = \left(\beta_{aca}^{(2)} + \beta_{bcb}^{(2)}\right)/2$ and $\beta_2^{(2)} = \left(\beta_{caa}^{(2)} + \beta_{cbb}^{(2)}\right)/2$, for a right-handed coordinate system. $\langle \cos\phi \rangle$ represents the cosine of the tilt angle averaged over space.

9 List of Publications

This thesis is based on the following publications:

Chapter 2

N. Gomopoulos, C. Lütgebaucks, Q. Sun, C. Macias-Romero, and S. Roke, "Label-free second harmonic and hyper Rayleigh scattering with high efficiency", *Opt. Express*, vol. 21 (1), p. 815, 2013

Chapter 3

G. Gonella, C. Lütgebaucks, A. G. F. de Beer, and S. Roke, "Second Harmonic and Sum Frequency Generation from Aqueous Interfaces is Modulated by Interference", *J. Phys. Chem. C*, vol. 120, 9165–9173, 2016

Chapter 4

C. Lütgebaucks, G. Gonella, and S. Roke, "Optical label-free and model-free probe of the surface potential of nanoscale and microscopic objects in aqueous solution", *Phys. Rev. B*, vol. 94, pp. 195410–195410, 2016

Chapter 5

N. Smolentsev, C. Lütgebaucks, H. I. Okur, A. De Beer, and S. Roke, "Intramolecular headgroup interaction and hydration as driving forces for membrane asymmetry", *J. Am. Chem. Soc.* Vol. 138 (12), pp. 4053–4060, 2016

Chapter 6

C. Lütgebaucks, C. Macias-Romero, and S. Roke, "Characterization of the interface of binary mixed DOPC:DOPS liposomes in water: The impact of charge condensation", *J. Chem. Phys.* Vol. 146, pp. 044701–044701, 2017

Additional publications by the same author:

Y. X. Chen, K. C. Jena, C. Lütgebaucks, H. I. Okur, and S. Roke, "Three Dimensional Nano "Langmuir Trough" for Lipid Studies", *Nano Letters*, vol. 15 (8), pp. 5558–5563, 2015

Bibliography

[1]   B. Alberts et al., *Molecular Biology of the Cell*, Garland Science, 2002.

[2]   S. J. Singer and G. L. Nicolson, "The Fluid Mosaic Model of the Structure of Cell Membranes", *Science*, vol. 175 (4023), pp. 720–731, 1972.

[3]   P. V. Escribá et al., "Membranes: a meeting point for lipids, proteins and therapies", *J. Cell. Mol. Med.* Vol. 12 (3), pp. 829–875, 2008.

[4]   G. van Meer, D. R. Voelker, and G. W. Feigenson, "Membrane lipids: where they are and how they behave", *Nat. Rev. Mol. Cell Biol.* Vol. 9 (2), pp. 112–124, 2008.

[5]   S. M. Butterfield and H. A Lashuel, "Amyloidogenic protein-membrane interactions: mechanistic insight from model systems.", *Angewandte Chemie (International ed. in English)*, vol. 49 (33), pp. 5628–54, 2010.

[6]   S. Petit-Zeman, "Membranes and the diseases within", *Nature*, pp. 1–3, 2004.

[7]   R. N. Weijers, "Lipid composition of cell membranes and its relevance in type 2 diabetes mellitus", *Curr. Diabetes Rev.* Vol. 8 (5), pp. 390–400, 2012.

[8]   F. X. Contreras et al., "Specificity of Intramembrane Protein-Lipid Interactions", *Cold Spring Harbor Perspect. Biol.* Vol. 3 (6) 2011.

[9]   R. G. W. Anderson and K. Jacobson, "A Role for Lipid Shells in Targeting Proteins to Caveolae, Rafts, and Other Lipid Domains", *Science*, vol. 296 (5574), pp. 1821–1825, 2002.

[10]   M. Ruiz, *No Title*, URL: https : / / commons . wikimedia . org / wiki / File : Cell _ membrane _ detailed _ diagram _ en . svg # /media / File : Cell_membrane_detailed_diagram_en.svg.

[11]   P. L. Yeagle, "Lipid Regulation of Cell-Membrane Structure and Function", *Faseb Journal*, vol. 3 (7), pp. 1833–1842, 1989.

[12]   J. F. Nagle and S. Tristram-Nagle, "Structure of lipid bilayers", *Biochim. Biophys. Acta - Biomembranes*, vol. 1469 (3), pp. 159–195, 2000.

[13]   P. L. Yeagle, "Non-covalent binding of membrane lipids to membrane proteins", *Biochim. Biophys. Acta*, vol. 1838 (6), pp. 1548–1559, 2014.

[14]   J. Seelig, "Thermodynamics of lipid-peptide interactions", *Biochi. Biophys. Acta*, vol. 1666 (1-2), pp. 40–50, 2004.

[15]   K. M. Eyster, "The membrane and lipids as integral participants in signal transduction: lipid signal transduction for the non-lipid biochemist", *Adv. Physiol. Educ.* Vol. 31 (1), pp. 5–16, 2007.

[16]   C. Koshy and C. Ziegler, "Structural insights into functional lipid-protein interactions in secondary transporters", *Biochim. Biophys. Acta Gen.* Vol. 1850 (3), pp. 476–487, 2015.

[17]   J. H. Borrell, Ò. Doménech, and K. M. W. Keough, *Membrane protein - lipid interactions: physics and chemistry in the bilayer*, Springer International Publishing, 2016.

[18]   T. R. Khan et al., "Lipid redistribution in phosphatidylserine-containing vesicles adsorbing on titania", *Biointerphases*, vol. 3 (2), FA90–FA95, 2008.

[19]   A. A. Gurtovenko and I. Vattulainen, "Molecular Mechanism for Lipid Flip-Flops", *J. Phys. Chem. B*, vol. 111 (48), pp. 13554–13559, 2007.

[20]   K. H. Jacobson et al., "Lipopolysaccharide Density and Structure Govern the Extent and Distance of Nanoparticle Interaction with Actual and Model Bacterial Outer Membranes", *Environ. Sci. Technol.* Vol. 49 (17), pp. 10642–10650, 2015.

[21]   R. Lipowsky and E. Sackmann, *Structure and dynamics of membranes*, Handbook of biological physics, Amsterdam ; New York: Elsevier Science, 1995.

[22]   P. Guyot-Sionnest, J. H. Hunt, and Y. R. Shen, "Sum-frequency vibrational spectroscopy of a Langmuir film: Study of molecular orientation of a two-dimensional system", *Phys. Rev. Lett.* Vol. 59 (14), pp. 1597–1600, 1987.

[23]   M. C. Gurau et al., "Thermodynamics of Phase Transitions in Langmuir Monolayers Observed by Vibrational Sum Frequency Spectroscopy", *J. Am. Chem. Soc.* Vol. 125 (37), pp. 11166–11167, 2003.

[24]   S. Roke et al., "Vibrational Sum Frequency Scattering from a Submicron Suspension", *Phys. Rev. Lett.* Vol. 91 (25), p. 258302, 2003.

[25]   E. H. G. Backus et al., "Laser-Heating-Induced Displacement of Surfactants on the Water Surface", *J. Phys. Chem. B*, vol. 116 (9), pp. 2703–2712, 2012.

[26]   J. D. F. Liljeblad et al., "Phospholipid Monolayers Probed by Vibrational Sum Frequency Spectroscopy: Instability of Unsaturated Phospholipids", *Biophys. J.* Vol. 98 (10), pp. L50–L52, 2010.

[27]   M. Bonn et al., "A Molecular View of Cholesterol-Induced Condensation in a Lipid Monolayer", *J. Phys. Chem. B*, vol. 108 (50), pp. 19083–19085, 2004.

[28] X. Chen et al., "Interfacial Water Structure Associated with Phospholipid Membranes Studied by Phase-Sensitive Vibrational Sum Frequency Generation Spectroscopy", *J. Am. Chem. Soc.* Vol. 132, pp. 11336–11342, 2010.

[29] G. Ma and H. C. Allen, "DPPC Langmuir Monolayer at the Air-Water Interface: Probing the Tail and Head Groups by Vibrational Sum Frequency Generation Spectroscopy", *Langmuir*, vol. 22 (12), pp. 5341–5349, 2006.

[30] M. Savva, B. Sivakumar, and B. Selvi, "The conventional Langmuir trough technique as a convenient means to determine the solubility of sparingly soluble surface-active molecules: Case study Cholesterol", *Colloids Surf., A*, vol. 325 (1-2), pp. 1–6, 2008.

[31] J. F. D. Liljeblad et al., "Supported Phospholipid Monolayers. The Molecular Structure Investigated by Vibrational Sum Frequency Spectroscopy", *J. Phys. Chem. C*, vol. 115 (21), pp. 10617–10629, 2011.

[32] Y. X. Chen, K. C. Jena, and S. Roke, "From Hydrophobic to Hydrophilic: The Structure and Density of the Hexadecane Droplet/Alkanol/Water Interface", *J. Phys. Chem. C*, vol. 119 (31), pp. 17725–17734, 2015.

[33] A. R. Thiam, R. V. Farese Jr., and T. C. Walther, "The biophysics and cell biology of lipid droplets", *Nature Rev. Mol. Cell Biol.* Vol. 14 (12), pp. 775–786, 2013.

[34] M. Khan, N. Dosoky, and J. Williams, "Engineering Lipid Bilayer Membranes for Protein Studies", *Int. J. Mol. Sci.* Vol. 14 (11), pp. 21561–21597, 2013.

[35] R. S. Ries et al., "Black Lipid Membranes: Visualizing the Structure, Dynamics, and Substrate Dependence of Membranes", *J. Phys. Chem. B*, vol. 108 (41), pp. 16040–16049, 2004.

[36] K. Weiß and J. Enderlein, "Lipid Diffusion within Black Lipid Membranes Measured with Dual-Focus Fluorescence Correlation Spectroscopy", *ChemPhysChem*, vol. 13 (4), pp. 990–1000, 2012.

[37] E. Gallucci, S. Micelli, and G. Monticelli, "Pore formation in lipid bilayer membranes made of phosphatidylinositol and oxidized cholesterol followed by means of alternating current", *Biophys. J.* Vol. 71 (2), pp. 824–831, 1996.

[38] R. C. Van Lehn et al., "Effect of Particle Diameter and Surface Composition on the Spontaneous Fusion of Monolayer-Protected Gold Nanoparticles with Lipid Bilayers", *Nano Lett.* Vol. 13 (9), pp. 4060–4067, 2013.

[39] M. Mingeot-Leclercq et al., "Atomic force microscopy of supported lipid bilayers", *Nature Prot.* Vol. 3 (10), pp. 1654–1659, 2008.

[40]   T. K. Lind et al., "Formation and Characterization of Supported Lipid Bilayers Composed of Hydrogenated and Deuterated Escherichia coli Lipids", *Plos One*, vol. 10 (12), p. 0144671, 2015.

[41]   G. Gramse et al., "Nanoscale measurement of the dielectric constant of supported lipid bilayers in aqueous solutions with electrostatic force microscopy", *Biophys. J.* Vol. 104, pp. 1257–1262, 2013.

[42]   J. Liu and J. C. Conboy, "1,2-Diacyl-Phosphatidylcholine Flip-Flop Measured Directly By Sum-Frequency Vibrational Spectroscopy.", *Biophys. J.* Vol. 89 (4), pp. 2522–2532, 2005.

[43]   J. Liu and J. C Conboy, "Direct measurement of the transbilayer movement of phospholipids by sum-frequency vibrational spectroscopy.", *J. Am. Chem. Soc.* Vol. 126 (27), pp. 8376–8367, 2004.

[44]   T. C. Anglin and J. C. Conboy, "Kinetics and thermodynamics of flip-flop in binary phospholipid membranes measured by sum-frequency vibrational spectroscopy", *Biochem.* Vol. 48 (43), pp. 10220–10234, 2009.

[45]   C. P. Brown et al., "Imaging and modeling collagen architecture from the nano to micro scale", *Biomed. Opt. Express*, vol. 5 (1), pp. 233–243, 2013.

[46]   M. Nakano et al., "Determination of interbilayer and transbilayer lipid transfers by time-resolved small-angle neutron scattering", *Phys. Rev. Lett.* Vol. 98 (23) 2007.

[47]   M. Nakano et al., "Flip-Flop of Phospholipids in Vesicles: Kinetic Analysis with Time-Resolved Small-Angle Neutron Scattering", *J. Phys. Chem. B*, vol. 113 (19), pp. 6745–6748, 2009.

[48]   J. M. Troiano et al., "Direct Probes of 4 nm Diameter Gold Nanoparticles Interacting with Supported Lipid Bilayers", *J. Phys. Chem. C*, vol. 119 (1), pp. 534–546, 2015.

[49]   R. P. Richter, N. Maury, and A. R. Brisson, "On the Effect of the Solid Support on the Interleaflet Distribution of Lipids in Supported Lipid Bilayers", *Langmuir*, vol. 21 (1), pp. 299–304, 2005.

[50]   K. L. Brown and J. C. Conboy, "Electrostatic induction of lipid asymmetry.", *J. Am. Chem. Soc.* Vol. 133 (23), pp. 8794–7, 2011.

[51]   H. Wu et al., "Phase transition behaviors of the supported DPPC bilayer investigated by sum frequency generation (SFG) vibrational spectroscopy and atomic force microscopy (AFM)", *Phys. Chem. Chem. Phys.* Vol. 18 (3), pp. 1411–1421, 2016.

[52] T. M. Allen and P. R. Cullis, "Liposomal drug delivery systems: From concept to clinical applications", *Adv. Drug Deliv. Rev.* Vol. 65 (1), pp. 36–48, 2013.

[53] L. Sercombe et al., "Advances and Challenges of Liposome Assisted Drug Delivery", *Front. Pharmacol.* Vol. 6 286 2015.

[54] L. Perera, U. Essmann, and M. L. Berkowitz, "Role of Water in the Hydration Force Acting between Lipid Bilayers", *Langmuir*, vol. 12 (11), pp. 2625–2629, 1996.

[55] H. I. Petrache et al., "Structure and fluctuations of charged phosphatidylserine bilayers in the absence of salt.", *Biophys. J.* Vol. 86 (3), pp. 1574–86, 2004.

[56] G. Cevc, "Membrane electrostatics", *Biochim. Biophys. Acta) - Rev. Biomem.* Vol. 1031 (3), pp. 311–382, 1990.

[57] V. B. Arakelian, D. Walther, and E. Donath, "Electric potential distributions around discrete charges in a dielectric membrane-electrolyte solution system", *Colloid Polym. Sci.* Vol. 271 (3), pp. 268–276, 1993.

[58] S. McLaughlin, "The electrostatic properties of membranes.", *Annu. Rev. Biophys Biophys. Chem.* Vol. 18, pp. 113–36, 1989.

[59] S. A. Pandit, D. Bostick, and M. L. Berkowitz, "Mixed Bilayer Containing Dipalmitoylphosphatidylcholine and Dipalmitoylphosphatidylserine: Lipid Complexation, Ion Binding, and Electrostatics", *Biophys. J.* Vol. 85 (5), pp. 3120–3131, 2003.

[60] H. P. Schwan et al., "Electrical Properties of Phospholipid Vesicles", *Biophys. J.* Vol. 10 (11), pp. 1102–1119, 1970.

[61] G. Qi et al., "Quantifying Surface Charge Density by Using an Electric Force Microscope with a Referential Structure", *J. Phys. Chem. C,* vol. 113 (1), pp. 204–207, 2009.

[62] Y. Yang et al., "Probing the Lipid Membrane Dipole Potential by Atomic Force Microscopy", *Biophys. J.* Vol. 95 (11), pp. 5193–5199, 2008.

[63] L. H. Klausen, T. Fuhs, and M. Dong, "Mapping surface charge density of lipid bilayers by quantitative surface conductivity microscopy", *Nature Comm.* Vol. 7, p. 12447, 2016.

[64] A. Tiraferri and M. Elimelech, "Direct quantification of negatively charged functional groups on membrane surfaces", *J. Membr. Sci.* Vol. 389, pp. 499–508, 2012.

[65] S.O. Hagge et al., "Inner field compensation as a tool for the characterization asymmetric mebranes and peptide-membrane interactions", *Biophys. J.* Vol. 86 (2), pp. 913–922, 2004.

Bibliography

[66] J. Lyklema, *Fundamentals of Interface and Colloid Science: Liquid-fluid interfaces*, Academic Press, 2000.

[67] R. J. Hunter, *Foundations of Colloid Science*, Sydney: Oxford University Press, 2002.

[68] M. F. Poyton and P. S. Cremer, "Electrophoretic measurements of lipid charges in supported bilayers", *Anal. Chem.* Vol. 85 (22), pp. 10803–11, 2013.

[69] A. Franken, "Generation of Optical Harmonics", *Phys. Rev. Lett.* Vol. 7 (1), pp. 118–120, 1961.

[70] J. N. Gannaway and C.J.R. Sheppard, "Second-harmonic imaging in the scanning optical microscope", *Opt. Quant. Electron.* Vol. 10 (19 78), pp. 435–439, 1978.

[71] I. Freund and M. Deutsch, "Second-harmonic microscopy of biological tissue.", *Opt. Lett.* Vol. 11 (2), pp. 94–96, 1986.

[72] O. Nadiarnykh et al., "Alterations of the extracellular matrix in ovarian cancer studied by Second Harmonic Generation imaging microscopy.", *BMC Cancer*, vol. 10, p. 94, 2010.

[73] M. W. Conklin et al., "Aligned collagen is a prognostic signature for survival in human breast carcinoma.", *Am. J. Path.* Vol. 178 (3), pp. 1221–1232, 2011.

[74] M. Han, G. Giese, and J. Bille, "Second harmonic generation imaging of collagen fibrils in cornea and sclera.", *Opt. Express*, vol. 13 (15), pp. 5791–5797, 2005.

[75] N. D. Kirkpatrick, M. A Brewer, and U. Utzinger, "Endogenous optical biomarkers of ovarian cancer evaluated with multiphoton microscopy.", *Cancer Epidemiol. Biomarkers Prev.* Vol. 16 (10), pp. 2048–57, 2007.

[76] S. Teng et al., "Multiphoton Autofluorescence and Second-Harmonic Generation Imaging of the Ex Vivo Porcine Eye", *Invest. Opthalmol. Vis. Sci.* Vol. 47 (3), p. 1216, 2006.

[77] P. Guyot-Sionnest, W. Chen, and Y. R. Shen, "General considerations on optical second-harmonic generation from surfaces and interfaces", *Phys. Rev. B*, vol. 33 (12), pp. 8254–8263, 1986.

[78] H. Held et al., "Bulk contribution from isotropic media in surface sum-frequency generation", *Phys. Rev. B*, vol. 66 (20), pp. 205110–205110.

[79] A. G. F. de Beer and S. Roke, "Sum frequency generation scattering from the interface of an isotropic particle: Geometrical and chiral effects", *Phys. Rev. B*, vol. 75, p. 245438, 2007.

[80] C. A. Coulson, A. Maccoll, and L. E. Sutton, "The polarizability of molecules in strong electric fields", *J. Chem. Soc. Farady Trans.* Vol. 48, pp. 106–113, 1952.

[81] S. J. Cyvin, J. E. Rauch, and J. C. Decius, "Theory of Hyper-Raman Effects (Nonlinear Inelastic Light Scattering): Selection Rules and Depolarization Ratios for the Second-Order Polarizability", *J. Chem. Phys.* Vol. 43 (11), pp. 4083–4095, 1965.

[82] N. Bloembergen and P. S. Pershan, "Light Waves at the Boundary of Nonlinear Media", *Phys. Rev.* Vol. 128 (2), pp. 606–622, 1962.

[83] W. J. Smit et al., "Freezing effects of oil-in-water emulsions studied by sumfrequency scattering spectroscopy", *J. Chem. Phys.* Vol. 145 (4), p. 044706, 2016.

[84] A. M. Jubb, W. Hua, and H. C. Allen, "Environmental Chemistry at Vapor/Water Interfaces: Insights from Vibrational Sum Frequency Generation Spectroscopy", *Annu. Rev. Phys. Chem.* Vol. 63, pp. 107–130, 2012.

[85] Y. R. Shen, "Surface properties probed by second-harmonic and sum-frequency generation", *Nature*, vol. 337, pp. 519–525, 1989.

[86] K. B. Eisenthal, "Liquid Interfaces Probed by Second-Harmonic and SumFrequency Spectroscopy", *Chem. Rev.* Vol. 96 (4), pp. 1343–1360, 1996.

[87] A. L. Harris et al., "Monolayer Vibrational Spectroscopy by Infrared-Visible Sum Generation at Metal and Semiconductor Surfaces", *Chem. Phys. Lett.* Vol. 141 (4), pp. 350–356, 1987.

[88] J. H. Hunt, P. Guyot-Sionnest, and Y. R. Shen, "Observation of C-H Stretch Vibrations of Monolayers of Molecules Optical Sum-Frequency Generation", *Chem. Phys. Lett.* Vol. 133 (3), pp. 189–192, 1987.

[89] H. Wang et al., "Quantitative Sum-Frequency Generation Vibrational Spectroscopy of Molecular Surfaces and Interfaces: Lineshape, Polarization, and Orientation", *Annu. Rev. Phys. Chem.* Vol. 66 (1), pp. 189–216, 2015.

[90] G. L. Richmond, "Molecular bonding and interactions at aqueous surfaces as probed by vibrational sum frequency spectroscopy", *Chem. Rev.* Vol. 102, pp. 2693–2724, 2002.

[91] B. Doughty et al., "Binding of the anti-cancer drug daunomycin to DNA probed by second harmonic generation", *J. Phys Chem. B*, vol. 117 (49), pp. 15285–9, 2013.

[92] R. W. Boyd and B. R. Masters, *Nonlinear optics*, 3rd ed., 2, Academic Press, 2008, p. 640.

Bibliography

[93] X. Zhao, S. Ong, and K. B. Eisenthal, "Polarization of water molecules at a charged interface. Second harmonic studies of charged monolayers at the air/water interface", *Chem. Phys. Lett.* Vol. 202 (6), pp. 513–520, 1993.

[94] X. Zhao et al., "New method for determination of surface pK , using second harmonic generation", *Chem. Phys. Lett.* Vol. 2 (2), pp. 203–207, 1993.

[95] S. Ong, X. Zhao, and K. B. Eisenthal, "Polarization of water molecules at a charged interface: second harmonic studies of the silica/water interface", *Chem. Phys. Lett.* Vol. 191 (3-4), pp. 327–335, 1992.

[96] C. M. Johnson and S. Baldelli, "Vibrational Sum Frequency Spectroscopy Studies of the Influence of Solutes and Phospholipids at Vapor/Water Interfaces Relevant to Biological and Environmental Systems", *Chem. Rev.* Vol. 114 (17), pp. 8416–8446, 2014.

[97] H. Wang et al., "Second harmonic generation from the surface of centrosymmetric particles in bulk solution", *Chem. Phys. Lett.* Vol. 259.

[98] H. B. de Aguiar et al., "Comparison of scattering and reflection SFG: a question of phase-matching", *Phys. Chem. Chem. Phys.* Vol. 14, pp. 6826–6832, 2012.

[99] J. I. Dadap, J. Shan, and T. F. Heinz, "Theory of optical second-harmonic generation from a sphere of centrosymmetric material: small-particle limit", *J. Opt. Soc.Am. B*, vol. 21 (7), p. 1328, 2004.

[100] A. G. F. de Beer, R. K. Campen, and S. Roke, "Separating surface structure and surface charge with second-harmonic and sum-frequency scattering", *Phys. Rev. B*, vol. 82 (23), p. 235431, 2010.

[101] A. G. F. de Beer and S. Roke, "Obtaining molecular orientation from second harmonic and sum frequency scattering experiments in water: angular distribution and polarization dependence", *J. Chem. Phys.* Vol. 132 (23), p. 234702, 2010.

[102] A. de Beer and S. Roke, "Nonlinear Mie theory for second-harmonic and sum-frequency scattering", *Phys. Rev. B*, vol. 79 (15), p. 155420, 2009.

[103] E. C. Y. Yan, Y. Liu, and K. B. Eisenthal, "New Method for Determination of Surface Potential of Microscopic Particles by Second Harmonic Generation", *J. Phys. Chem. B*, vol. 5647 (98), pp. 6331–6336, 1998.

[104] Y. Liu et al., "Surface Potential of Charged Liposomes Determined by Second Harmonic Generation", *Langmuir*, (3), pp. 2063–2066, 2001.

[105] M. L. Strader et al., "Label-free spectroscopic detection of vesicles in water using vibrational sum frequency scattering", *Soft Matter*, vol. 7 (10), p. 4959, 2011.

[106] B. Schürer et al., "Probing colloidal interfaces by angle-resolved second harmonic light scattering", *Phys. Rev. B*, vol. 823 (24), pp. 1–4, 2010.

[107] J. H. Kim and M. W. Kim, "In-situ observation of the inside-to-outside molecular transport of a liposome.", *J. Phys. Chem. B*, vol. 112 (49), pp. 15673–7, 2008.

[108] A. Srivastava and K. B. Eisenthal, "Kinetics of molecular transport across a liposome bilayer", *Chem. Phys. Lett.* Vol. 292 (0009), pp. 345–351, 1998.

[109] E. C. Y. Yan and K. B. Eisenthal, "Effect of Cholesterol on Molecular Transport of Organic Cations across Liposome Bilayers Probed by Second Harmonic Generation", *Biophys. J.* Vol. 79, pp. 898–903, 2000.

[110] X. Shang et al., "Effects of Counterions on Molecular Transport Across Liposome Bilayer: Probed by Second Harmonic Generation", *J. Phys. Chem. B*, vol. 105 (51), pp. 12816–12822, 2001.

[111] J. Liu et al., "Second harmonic studies of ions crossing liposome membranes in real time", *J. Phys. Chem. B*, vol. 112 (48), pp. 15263–15266, 2008.

[112] Y. Rao et al., "Label-free probe of HIV-1 TAT peptide binding to mimetic membranes", *Proc. Natl. Ac. Sci. USA*, vol. 111 (35), pp. 12684–12688, 2014.

[113] N. Gomopoulos et al., "Label-free second harmonic and hyper Rayleigh scattering with high efficiency", *Opt. Express*, vol. 21 (1), p. 815, 2013.

[114] C. E. Webb and J. D. C. Jones, *Handbook of laser technology and applications*, Bristol ; Philadelphia : Institute of Physics, 2004, pp. 1–2725.

[115] Hamamatsu Photonics, *Photomultiplier tubes - Basics and Applications*, 2007.

[116] K. Clays and A. Persoons, "Hyper-Rayleigh Scattering in Solution", *Rev. Sci. Instrum.* Vol. 63 (6), pp. 3285–3289, 1992.

[117] R. Bersohn, Y. Pao, and H.L. Frisch, "Double-Quantum Light Scattering by Molecules", *J. Chem. Phys.* Vol. 45 (9), p. 3184, 1966.

[118] B. Schürer and W. Peukert, "In Situ Surface Characterization of Polydisperse Colloidal Particles by Second Harmonic Generation", *Part. Sci. Technol.* Vol. 28 (5), pp. 458–471, 2010.

[119] J. I. Dadap et al., "Second-Harmonic Rayleigh Scattering from a Sphere of Centrosymmetric Material", *Phys. Rev. Lett.* Vol. 83 (20), pp. 4045–4048, 1999.

[120] L. Schneider, H.J. Schmid, and W. Peukert, "Influence of particle size and concentration on the second-harmonic signal generated at colloidal surfaces", *Appl. Phys. B*, vol. 87 (2), pp. 333–339, 2007.

Bibliography

[121] M. Bonn, Y. Nagata, and E. H. G. Backus, "Molecular Structure and Dynamics of Water at the Water-Air Interface Studied with Surface-Specific Vibrational Spectroscopy", *Angew. Chem. Int. Ed.* Vol. 54 (19), pp. 5560–5576, 2015.

[122] A. G. F. de Beer and S. Roke, "What interactions can distort the orientational distribution of interfacial water molecules as probed by second harmonic and sum frequency generation?", *J. Chem. Phys.* Vol. 145 (4), p. 44705, 2016.

[123] Richard P. Feynman, "The Feynman Lectures on Physics; Vol. I", *Am. J. Phys.* Vol. 33 (9), p. 750, 1965.

[124] A. Einstein, "Über die von der molekularkinetischen Theorie der Wärme geforderte Bewegung von in ruhenden Flüssigkeiten suspendierten Teilchen", *Ann. Phys.* Vol. 322 (8), pp. 549–560, 1905.

[125] J. N. Israelachvili, *Intermolecular and surface forces*, Academic Press; New York, 1991.

[126] Mijones1984, *No Title*, URL: https://commons.wikimedia.org/wiki/File: Diagram_of_zeta_potential_and_slipping_planeV2.svg#/media/File: Diagram_of_zeta_potential_and_slipping_planeV2.svg.

[127] H. Ohshima, *Theory of Colloid and Interfacial Phenomena*, Academic Press, 2006.

[128] M. J. Hope et al., "Production of large unilamellar vesicles by a rapid extrusion procedure. Characterization of size distribution, trapped volume and ability to maintain a membrane potential", *Biochim. Biophys. Acta - Biomembr.* Vol. 812 (1), pp. 55–65, 1985.

[129] R. C. MacDonald et al., "Small-volume extrusion apparatus for preparation of large, unilamellar vesicles.", *Biochim. Biophys. Acta*, vol. 1061 (2), pp. 297–303, 1991.

[130] P. S. Chen, T. Y. Toribara, and H. Warner, "Citation Classics - Microdetermination of Phosphorus", *Anal. Chem.* (28), pp. 1756–1758, 1956.

[131] AvantiPolarLipids, *No Title*, URL: http://avantilipids.com/tech-support/ analytical-procedures/determination-of-total-phosphorus/.

[132] Y. J. Zhang and P. S. Cremer, "Interactions between macromolecules and ions: the Hofmeister series", *Curr. Opin. Chem. Biol.* Vol. 10 (6), pp. 658–663, 2006.

[133] Y. Marcus, "Effect of Ions on the Structure of Water: Structure Making and Breaking", *Chem. Rev.* Vol. 109 (3), pp. 1346–1370, 2009.

[134] D. J. Tobias et al., "Simulation and Theory of Ions at Atmospherically Relevant Aqueous Liquid-Air Interfaces", *Annu. Rev. Phys. Chem.* Vol. 64, pp. 339–359, 2013.

[135] R. J. Hunter, *Zeta Potential in Colloid Science*, Sydney: Academic Press, 1981.

[136] Y. Melnichenko, *Small-angle scattering from confined and interfacial fluids*, 1st ed., Springer International Publishing, 2016, p. 314.

[137] P. Jungwirth, B. J. Finlayson-Pitts, and D. J. Tobias, "Introduction: Structure and chemistry at aqueous interfaces", *Chem. Rev.* Vol. 106 (4), pp. 1137–1139, 2006.

[138] M. Salmeron and R. Schlogl, "Ambient pressure photoelectron spectroscopy: A new tool for surface science and nanotechnology", *Surf. Sci. Rep.* Vol. 63 (4), pp. 169–199, 2008.

[139] K. B. Eisenthal, "Second harmonic spectroscopy of aqueous nano- and microparticle interfaces.", *Chem. Rev.* Vol. 106 (4), pp. 1462–77, 2006.

[140] P. Jungwirth and B. Winter, "Ions at aqueous interfaces: From water surface to hydrated proteins", *Annu. Rev. Phys. Chem.* Vol. 59, pp. 343–366, 2008.

[141] F. M. Geiger, "Second harmonic generation, sum frequency generation, and chi(3): dissecting environmental interfaces with a nonlinear optical Swiss Army knife.", *Annu. Rev. Phys. Chem.* Vol. 60, pp. 61–83, 2009.

[142] B. Abel, "Hydrated Interfacial Ions and Electrons", *Annu. Rev. Phys. Chem.* Vol. 64, pp. 533–552, 2013.

[143] A. Eftekhari-Bafrooei and E. Borguet, "Effect of Electric Fields on the Ultrafast Vibrational Relaxation of Water at a Charged Solid-Liquid Interface as Probed by Vibrational Sum Frequency Generation", *J. Phys. Chem. Lett.* Vol. 2 (12), pp. 1353–1358, 2011.

[144] C. S. Tian and Y. R. Shen, "Structure and charging of hydrophobic material/water interfaces studied by phase-sensitive sum-frequency vibrational spectroscopy", *Proc. Nat. Acad. Sci.* Vol. 106 (36), pp. 15148–15153, 2009.

[145] A. P. Willard and D. Chandler, "Instantaneous Liquid Interfaces", *J. Phys. Chem. B*, vol. 114 (5), pp. 1954–1958, 2010.

[146] K. C. Jena, P. A. Covert, and D. K. Hore, "The Effect of Salt on the Water Structure at a Charged Solid Surface: Differentiating Second- and Third-order Nonlinear Contributions", *J. Phys. Chem. Lett.* Vol. 2 (9), pp. 1056–1061, 2011.

[147] D. E. Gragson, B. M. McCarty, and G. L. Richmond, "Ordering of Interfacial Water Molecules at the Charged Air/Water Interface Observed by Vibrational Sum Frequency Generation", *J. Am. Chem. Soc.* Vol. 119, pp. 6144–6152, 1997.

[148] Y. R. Shen and V. Ostroverkhov, "Sum-frequency vibrational spectroscopy on water interfaces: Polar orientation of water molecules at interfaces", *Chem. Rev.* Vol. 106 (4), pp. 1140–1154, 2006.

Bibliography

[149] L. Piatkowski et al., "Extreme surface propensity of halide ions in water", *Nat. Commun.* Vol. 5 2014.

[150] C. Sauerbeck, B. Braunschweig, and W. Peukert, "Surface Charging and Interfacial Water Structure of Amphoteric Colloidal Particles", *J. Phys. Chem. C*, vol. 118 (19), pp. 10033–10042, 2014.

[151] A. G. Lambert, P. B. Davies, and D. J. Neivandt, "Implementing the theory of sum frequency generation vibrational spectroscopy: a tutorial review", *Appl. Spectr. Rev.* Vol. 40, pp. 103–144, 2005.

[152] S. Roke and G. Gonella, "Nonlinear light scattering and spectroscopy of particles and droplets in liquids", *Annu. Rev. Phys. Chem.* Vol. 63 (January), pp. 353–378, 2012.

[153] A. Eftekhari-Bafrooei and E. Borguet, "Effect of Surface Charge on the Vibrational Dynamics of Interfacial Water", *J. Am. Chem. Soc.* Vol. 131 (34), pp. 12034–12035, 2009.

[154] D. J. Griffiths, *Introduction to Electrodynamics*, 3rd, Upper Saddle River, N.J.: Prentice Hall, 1999, p. 576.

[155] G. Gonella et al., "Second Harmonic and Sum Frequency Generation from Aqueous Interfaces is Modulated by Interference", *J. Phys. Chem. C*, vol. 120, 9165–9173, 2016.

[156] Y. R. Shen, *The principles of nonlinear optics*, Wiley clas, Hoboken, N.J.: Wiley-Interscience, 2003, p. 563.

[157] V. P. Sokhan and D. J. Tildesley, "Molecular dynamics simulation of the nonlinear optical susceptibility at the phenol/water/air interface", *Faraday Discuss.* Vol. 104, pp. 193–208, 1996.

[158] V. P. Sokhan and D. J. Tildesley, "The free surface of water: molecular orientation, surface potential and nonlinear susceptibility", *Mol. Phys.* Vol. 92 (4), pp. 625–640, 1997.

[159] M. C. Goh et al., "Absolute Orientation of Water-Molecules at the Neat Water-Surface", *J. Phys. Chem.* Vol. 92 (18), pp. 5074–5075, 1988.

[160] T. Ishiyama and A. Morita, "Molecular dynamics study of gas-liquid aqueous sodium halide interfaces. II. Analysis of vibrational sum frequency generation spectra", *J. Phys. Chem. C*, vol. 111 (2), pp. 738–748, 2007.

[161] C. S. Tian et al., "Interfacial structures of acidic and basic aqueous solutions", *J. Am. Chem. Soc.* Vol. 130 (39), pp. 13033–13039, 2008.

[162] J. Samson et al., "Sum frequency spectroscopy of the hydrophobic nanodroplet/water interface: Absence of hydroxyl ion and dangling OH bond signatures", *Chem. Phys. Lett.* Vol. 615, pp. 124–131, 2014.

[163] C. S. Tian et al., "Surface Propensities of Atmospherically Relevant Ions in Salt Solutions Revealed by Phase-Sensitive Sum Frequency Vibrational Spectroscopy", *J. Phys. Chem. Lett.* Vol. 2 (15), pp. 1946–1949, 2011.

[164] L. Zhang et al., "Structures and charging of alpha-alumina (0001)/water interfaces studied by sum-frequency vibrational spectroscopy", *J. Am. Chem. Soc.* Vol. 130 (24), pp. 7686–7694, 2008.

[165] J. L. Achtyl et al., "Free Energy Relationships in the Electrical Double Layer over Single-Layer Graphene", *J. Am. Chem. Soc.* Vol. 135 (3), pp. 979–981, 2013.

[166] S. Strazdaite, J. Versluis, and H. J. Bakker, "Water orientation at hydrophobic interfaces", *J. Chem. Phys.* Vol. 143 (8) 2015.

[167] S. Ye, S. Nihonyanagi, and K. Uosaki, "Sum frequency generation (SFG) study of the pH-dependent water structure on a fused quartz surface modified by an octadecyltrichlorosilane (OTS) monolayer", *Phys. Chem. Chem. Phys.* Vol. 3 (16), pp. 3463–3469, 2001.

[168] N. Agmon et al., "Protons and Hydroxide Ions in Aqueous Systems", *Chem. Rev.* Vol. 116 (13), pp. 7642–7672, 2016.

[169] A.G.F de Beer et al., "Research note: $\chi^{(2)}, \chi^{(3)}$ and the effect of E_{DC}", *Lab internal report* 2009.

[170] S. J. Byrnes, P. L. Geissler, and Y. R. Shen, "Ambiguities in surface nonlinear spectroscopy calculations", *Chem. Phys. Lett.* Vol. 516 (4-6), pp. 115–124, 2011.

[171] Y. C. Wen et al., "Unveiling Microscopic Structures of Charged Water Interfaces by Surface-Specific Vibrational Spectroscopy", *Phys. Rev. Lett.* Vol. 116 (1) 2016.

[172] P. E. Ohno et al., "Phase-referenced nonlinear spectroscopy of the alpha-quartz/water interface", *Nat. Commun.* Vol. 7 2016.

[173] S. Roke, M. Bonn, and A. V. Petukhov, "Nonlinear optical scattering: The concept of effective susceptibility", *Phys. Rev. B*, vol. 70 (11), p. 115106, 2004.

[174] R. K. Campen et al., "Linking Surface Potential and Deprotonation in Nanoporous Silica : Second Harmonic Generation and Acid / Base Titration", *J. Phys. Chem. C*, pp. 18465–18473, 2010.

[175] R. R. Kumal, T. E. Karam, and L. H. Haber, "Determination of the Surface Charge Density of Colloidal Gold Nanoparticles Using Second Harmonic Generation", *J. Phys. Chem. C*, pp. 16200–16207, 2015.

Bibliography

[176] P. B. Petersen and R. J. Saykally, "Adsorption of ions to the surface of dilute electroyte solutions: The Jones-Ray effect revisited", *J. Am. Chem. Soc.* Vol. 127 (44), pp. 15446–15452, 2005.

[177] R. Scheu et al., "Charge Asymmetry at Aqueous Hydrophobic Interfaces and Hydration Shells", *Angew. Chem., Int. Ed.* Vol. 53 (36), pp. 9560–9563, 2014.

[178] R. Scheu et al., "Specific Ion Effects in Amphiphile Hydration and Interface Stabilization", *J. Am. Chem. Soc.* Vol. 136 (5), pp. 2040–2047, 2014.

[179] R. Scheu et al., "Stern Layer Formation Induced by Hydrophobic Interactions: A Molecular Level Study", *J. Am. Chem. Soc.* Vol. 135 (51), pp. 19330–19335, 2013.

[180] V. Liljestrom, .J Seitsonen, and M. A. Kostiainen, "Electrostatic Self-Assembly of Soft Matter Nanoparticle Cocrystals with Tunable Lattice Parameters", *ACS Nano*, vol. 9 (11), pp. 11278–11285, 2015.

[181] X. Y. Sun, D. H. Bamford, and M. M. Poranen, "Electrostatic Interactions Drive the Self-Assembly and the Transcription Activity of the Pseudomonas Phage phi 6 Procapsid", *J. Virol.* Vol. 88 (12), pp. 7112–7116, 2014.

[182] H. F. Lodish, *Molecular Cell Biology*, New York, 2000.

[183] R. L. McCreery, "Effects of electronic coupling and electrostatic potential on charge transport in carbon-based molecular electronic junctions", *Beilstein J. Nanotechnol.* Vol. 7, pp. 32–46, 2016.

[184] Y. Zhang and P. S. Cremer, "Chemistry of Hofmeister Anions and Osmolytes", *Annu. Rev. Phys. Chem.* Vol. 61 (1), pp. 63–83, 2010.

[185] M. D. Baer et al., "Electrochemical Surface Potential Due to Classical Point Charge Models Drives Anion Adsorption to the Air-Water Interface", *J. Phys. Chem. Lett.* Vol. 3 (11), pp. 1565–1570, 2012.

[186] C. D. Taylor et al., "First principles reaction modeling of the electrochemical interface: Consideration and calculation of a tunable surface potential from atomic and electronic structure", *Phys. Rev. B*, vol. 73 (16) 2006.

[187] C. T. Konek et al., "Interfacial acidities, charge densities, potentials, and energies of carboxylic acid-functionalized silica/water interfaces determined by second harmonic generation", *J. Am. Chem. Soc.* Vol. 126 (38), pp. 11754–11755, 2004.

[188] R. Shah et al., *Lipid Nanoparticles: Production, Characterization and Stability*, Springer International Publishing, 2015.

[189]   M. A. Brown et al., "Determination of Surface Potential and Electrical Double-Layer Structure at the Aqueous Electrolyte-Nanoparticle Interface", *Phys. Rev. X,* vol. 6 (1), pp. 11001–11007, 2016.

[190]   G. Gonella and H. L. Dai, "Second Harmonic Light Scattering from the Surface of Colloidal Objects: Theory and Applications", *Langmuir,* vol. 30 (10), pp. 2588–2599, 2014.

[191]   B. Schürer et al., "Second Harmonic Light Scattering from Spherical Polyelectrolyte Brushes", *J. Phys. Chem. C,* vol. 115, pp. 18302–18309, 2011.

[192]   N. Smolentsev et al., "Intramolecular headgroup interaction and hydration as driving forces for membrane asymmetry", *J. Am. Chem. Soc.* Vol. 138 (12), pp. 4053–4060, 2016.

[193]   J. N. Malin and F. M. Geiger, "Uranyl Adsorption and Speciation at the Fused Silica/Water Interface Studied by Resonantly Enhanced Second Harmonic Generation and the $\chi(3)$ Method", *J. Phys. Chem. A,* vol. 114 (4), pp. 1797–1805, 2010.

[194]   Y. X. Chen et al., "Three Dimensional Nano "Langmuir Trough" for Lipid Studies", *Nano Letters,* vol. 15 (8), pp. 5558–5563, 2015.

[195]   X. Zhuang et al., "Mapping molecular orientation and conformation at interfaces by surface nonlinear optics", *Phys. Rev. B.* Vol. 59, p. 12632, 1999.

[196]   H. F. Wang et al., "Quantitative spectral and orientational analysis in surface sum frequency generation vibrational spectroscopy (SFG-VS)", *Int. Rev. Phys. Chem.* Vol. 24, pp. 191–256, 2005.

[197]   Y. Chen et al., "Electrolytes induce long-range orientational order and free energy changes in the H-bond network of bulk water", *Sci. Adv.* Vol. 2 (4), e1501891–e1501891, 2016.

[198]   A. V. Gubskaya and P. G. Kusalik, "The multipole polarizabilities and hyperpolarizabilities of the water molecule in liquid state: an ab initio study", *Mol Phys,* vol. 99 (13), pp. 1107–1120, 2001.

[199]   G. J. Simpson and K. L. Rowlen, "An SHG magic angle: Dependence of second harmonic generation orientation measurements on the width of the orientation distribution", *J. Am. Chem. Soc.* Vol. 121 (11), pp. 2635–2636, 1999.

[200]   Ch. Wohlfarth, *Refractive index of hexadecane,* 2008.

[201]   C. Gardiner et al., "Measurement of refractive index by nanoparticle tracking analysis reveals heterogeneity in extracellular vesicles", *J. Extracell. Vesicles,* vol. 3, p. 25361, 2014.

Bibliography

[202] S. Yamaguchi et al., "Electric quadrupole contribution to the nonresonant background of sum frequency generation at air/liquid interfaces", *J. Chem. Phys.* Vol. 134 (18), p. 184705, 2011.

[203] K. Shiratori et al., "Computational analysis of the quadrupole contribution in the second-harmonic generation spectroscopy for the water/vapor interface", *J. Chem. Phys.* Vol. 138 (6), p. 64704, 2013.

[204] F. C. Tsui, S. A. Sundberg, and W. L. Hubbell, "Distribution of Charge on Photoreceptor Disk Membranes and Implications for Charged Lipid Asymmetry", *Biophys. J.* Vol. 57 (1), pp. 85–97, 1990.

[205] D. J. Crommelin, "Influence of lipid composition and ionic strength on the physical stability of liposomes", *J. Pharm. Sci.* Vol. 73 (11), pp. 1559–1563, 1984.

[206] A. Christiansson et al., "Involvement of Surface-Potential in Regulation of Polar Membrane-Lipids in Acholeplasma-Laidlawii", *Journal of Biological Chemistry*, vol. 260 (7), pp. 3984–3990, 1985.

[207] S. H. Behrens and D. G. Grier, "The charge of glass and silica surfaces", *J. Chem. Phys.* Vol. 115 (14), p. 6716, 2001.

[208] P. C. Hiemenz and R. Rajagopalan, *Principles of Colloid and Surface Chemistry*, 3rd, New York: Marcel Dekker, 1997, p. 650.

[209] K. A. Riske et al., "Temperature and ionic strength dependent light scattering of DMPG dispersions", *Chem. Phys. Lipids*, vol. 89 (1), pp. 31–44, 1997.

[210] W. H. Binder, V. Barragan, and F. M. Menger, "Domains and Rafts in Lipid Membranes", *Angew. Chem., Int. Ed.* Vol. 42 (47), pp. 5802–5827, 2003.

[211] P. A. Leventis and S. Grinstein, "The Distribution and Function of Phosphatidylserine in Cellular Membranes", *Annu. Rev. Biophys.* Vol. 39 (1), pp. 407–427, 2010.

[212] G. van Meer and A. I. P. M. de Kroon, "Lipid map of the mammalian cell", *J. Cell Sci.* Vol. 124 (1), pp. 5–8, 2011.

[213] P. L. Yeagle, W. C. Hutton, and R. B. Martin, "Transmembrane asymmetry of vesicle lipids", *J. Biol. Chem.* Vol. 251 (7), pp. 2110–2112, 1976.

[214] V. A. Fadok and P. M. Henson, "Apoptosis: Getting rid of the bodies", *Curr. Biol.* Vol. 8 (19), R693–R695, 1998.

[215] X. Cong et al., "Unquenchable Surface Potential Dramatically Enhances Cu^{2+} Binding to Phosphatidylserine Lipids", *J. Am. Chem. Soc.* Vol. 137 (24), pp. 7785–7792, 2015.

[216] M. Frechin et al., "Expression of Nuclear and Mitochondrial Genes Encoding ATP Synthase Is Synchronized by Disassembly of a Multisynthetase Complex", *Mol. Cell*, vol. 56 (6), pp. 763–776, 2014.

[217] M. Frechin et al., "Cell-intrinsic adaptation of lipid composition to local crowding drives social behaviour", *Nature*, vol. 523 (7558), pp. 88–91, 2015.

[218] S. W. I. Siu et al., "Biomolecular simulations of membranes: Physical properties from different force fields", *J. Chem. Phys.* Vol. 128 (12) 2008.

[219] Timothy C Anglin and John C Conboy, "Lateral pressure dependence of the phospholipid transmembrane diffusion rate in planar-supported lipid bilayers.", *Biophysical journal*, vol. 95 (1), pp. 186–93, 2008.

[220] M. Berkowitz and S. Pandit, "Molecular dynamics simulation of DPPC : DPPS bilayers in electrolyte solutions.", *Biophys. J.* Vol. 84 (2), 46a–46a, 2003.

[221] S. Mondal and C. Mukhopadhyay, "Molecular level investigation of organization in ternary lipid bilayer: A computational approach", *Langmuir*, vol. 24 (18), pp. 10298–10305, 2008.

[222] R. Vacha et al., "Effects of Alkali Cations and Halide Anions on the DOPC Lipid Membrane", *J. Phys. Chem. A*, vol. 113 (26), pp. 7235–7243, 2009.

[223] V. Kiessling, C. Wan, and L. K. Tamm, "Domain coupling in asymmetric lipid bilayers", *Biochim. Biophys. Acta, Biomembr.* Vol. 1788 (1), pp. 64–71, 2009.

[224] S. L. Veatch et al., "Liquid domains in vesicles investigated by NMR and fluorescence microscopy", *Biophys. J.* Vol. 86 (5), pp. 2910–2922, 2004.

[225] E. Serebryany, G. A. Zhu, and E. C. Y. Yan, "Artificial membrane-like environments for in vitro studies of purified G-protein coupled receptors", *Biochim. Biophys. Acta, Biomembr.* Vol. 1818 (2), pp. 225–233, 2012.

[226] R. P. Richter, R. Berat, and A. A. Brisson, "Formation of solid-supported lipid bilayers: An integrated view", *Langmuir*, vol. 22 (8), pp. 3497–3505, 2006.

[227] E. C. Y. Yan, Z. Wang, and L. Fu, "Proteins at Interfaces Probed by Chiral Vibrational Sum Frequency Generation Spectroscopy", *J. Phys. Chem. B*, vol. 119 (7), pp. 2769–2785, 2015.

[228] E. C. Y. Yan, Y. Liu, and K. B. Eisenthal, "In Situ Studies of Molecular Transfer between Microparticles by Second-Harmonic Generation", *J. Phys. Chem. B*, vol. 105 (36), pp. 8531–8537, 2001.

[229] H. B. de Aguiar, J. S. Samson, and S. Roke, "Probing nanoscopic droplet interfaces in aqueous solution with vibrational sum-frequency scattering: A study of the effects of path length, droplet density and pulse energy", *Chem. Phys. Lett.* Vol. 512 (1-3), pp. 76–80, 2011.

Bibliography

[230] H. B. de Aguiar et al., "Surface structure of sodium dodecyl sulfate surfactant and oil at the oil-in-water droplet liquid/liquid interface: a manifestation of a nonequilibrium surface state", *J. Phys. Chem. B*, vol. 115 (12), pp. 2970–2978, 2011.

[231] N. Casillas-Ituarte et al., "Na^+ and Ca^{2+} Effect on the Hydration and Orientation of the Phosphate Group of DPPC at Air-Water and Air-Hydrated Silica Interfaces", *J. Phys. Chem. B*, vol. 114 (29), pp. 9485–9495, 2010.

[232] S. J. Attwood, Y. Choi, and Z. Leonenko, "Preparation of DOPC and DPPC Supported Planar Lipid Bilayers for Atomic Force Microscopy and Atomic Force Spectroscopy.", *Int. J. Mol. Sci.* Vol. 14 (2), pp. 3514–3539, 2013.

[233] V. N. P. Anghel et al., "Scattering from laterally heterogeneous vesicles. II. The form factor", *J. Appl. Crystallogr.* Vol. 40 (3), pp. 513–525, 2007.

[234] K. C. Jena, R. Scheu, and S. Roke, "Surface Impurities Are Not Responsible For the Charge on the Oil/Water Interface: A Comment", *Angew. Chem., Int. Ed.* Vol. 51 (52), pp. 12938–12940, 2012.

[235] S. A. Pandit and M. L. Berkowitz, "Molecular dynamics simulation of dipalmitoylphosphatidylserine bilayer with Na^+ counterions", *Biophys. J.* Vol. 82 (4), pp. 1818–1827, 2002.

[236] P. Mukhopadhyay, L. Monticelli, and D. P. Tieleman, "Molecular Dynamics Simulation of a Palmitoyl-Oleoyl Phosphatidylserine Bilayer with Na^+ Counterions and NaCl", *Biophys. J.* Vol. 86 (3), pp. 1601–1609, 2004.

[237] N. Shimokawa et al., "Phase separation of a mixture of charged and neutral lipids on a giant vesicle induced by small cations", *Chem. Phys. Lett.* Vol. 496 (1-3), pp. 59–63, 2010.

[238] A. Bandekar and S. Sofou, "Floret-Shaped Solid Domains on Giant Fluid Lipid Vesicles Induced by pH", *Langmuir*, vol. 28 (9), pp. 4113–4122, 2012.

[239] H. L. Casal et al., "Infrared and 31P-NMR studies of the effect of Li^+ and Ca^{2+} on phosphatidylserines", *Biochim. Biophys. Acta - Lipids and Lipid Metabolism*, vol. 919 (3), pp. 275–286, 1987.

[240] X. Chen and H. C. Allen, "Interactions of Dimethylsulfoxide with a Dipalmitoylphosphatidylcholine Monolayer Studied by Vibrational Sum Frequency Generation", *J. Phys. Chem. A*, vol. 113 (45), pp. 12655–12662, 2009.

[241] R. A. Walker, J. C. Conboy, and G. L. Richmond, "Molecular Structure and Ordering of Phospholipids at a Liquid-Liquid Interface", *Langmuir*, vol. 13 (12), pp. 3070–3073, 1997.

[242]   N. Tokutake et al., "Quantifying the Effects of Deuterium Substitution on Phospholipid Mixing in Bilayer Membranes. A Nearest-Neighbor Recognition Investigation", *J. Am. Chem. Soc.* Vol. 125 (51), pp. 15764–15766, 2003.

[243]   A. G. F. de Beer, S. Roke, and J. I. Dadap, "Theory of optical second-harmonic and sum-frequency scattering from arbitrarily shaped particles", *J. Opt. Soc. Am. B*, vol. 28 (6), p. 1374, 2011.

[244]   N. F. A. van der Vegt et al., "Water-Mediated Ion Pairing: Occurrence and Relevance", *Chem. Rev.* Vol. 116 (13), pp. 7626–7641, 2016.

[245]   A. Honigmann et al., "STED microscopy detects and quantifies liquid phase separation in lipid membranes using a new far-red emitting fluorescent phosphoglycerolipid analogue", *Faraday Discuss.* Vol. 161, pp. 77–89, 2013.

[246]   M. H. Abraham et al., "Thermodynamics of Solute Transfer from Water to Hexadecane", *J. Chem. Soc.,Perkin Trans. 2*, (2), pp. 291–300, 1990.

[247]   C. Lütgebaucks, G. Gonella, and S. Roke, "Optical label-free and model-free probe of the surface potential of nanoscale and microscopic objects in aqueous solution", *Phys. Rev. B*, vol. 94, pp. 195410–195410, 2016.

[248]   A. V. Delgado, *Interfacial electrokinetics and electrophoresis*, Surfactant science series, New York: Marcel Dekker, Inc., 2002, xii, 991 p.

[249]   S. Y. Bhide and M. L. Berkowitz, "Structure and dynamics of water at the interface with phospholipid bilayers", *J. Chem. Phys.* Vol. 123 (22), p. 224702, 2005.

[250]   J. T. Davies and E. K. Rideal, *Interfacial Phenomena*, San Diego, 1963.

[251]   G. S. Manning, "Limiting Laws and Counterion Condensation in Polyelectrolyte Solutions I. Colligative Properties", *J. Chem. Phys.* Vol. 51 (3), p. 924, 1969.

[252]   G. S. Manning, "Counterion condensation theory of attraction between like charges in the absence of multivalent counterions", *Eur. Phys. J. E*, vol. 34 (12) 2011.

[253]   U. Böhme and U. Scheler, "Counterion condensation and effective charge of poly(styrenesulfonate)", *Advances in Colloid and Interface Science*, vol. 158 (1-2), pp. 63–67, 2010.

[254]   D. A. J. Gillespie et al., "Counterion condensation on spheres in the salt-free limit", *Soft Matter*, vol. 10 (4), pp. 566–577, 2014.

[255]   G. S. Manning, "Counterion Condensation on Charged Spheres, Cylinders, and Planes", *J. Phys. Chem. B*, vol. 111 (29), pp. 8554–8559, 2007.

Bibliography

[256]   M. R. Moncelli, L. Becucci, and R. Guidelli, "The intrinsic pKa values for phosphatidylcholine, phosphatidylethanolamine, and phosphatidylserine in monolayers deposited on mercury electrodes.", *Biophys. J.* Vol. 66 (6), pp. 1969–80, 1994.

[257]   D. H. Mengistu, E. E. Kooijman, and S. E. May, "Ionization Properties of Mixed Lipid Membranes: A Gouy-Chapman Model of the Electrostatic-Hydrogen Bond Switch", *Biophys. J.* Vol. 100 (3), 365a, 2011.

[258]   M. Yi, H. Nymeyer, and H. Zhou, "Test of the Gouy-Chapman Theory for a Charged Lipid Membrane against Explicit-Solvent Molecular Dynamics Simulations", *Phys. Rev. Lett.* Vol. 101 (3), p. 038103, 2008.

[259]   C. Lütgebaucks, C. Macias-Romero, and S. Roke, "Characterization of the interface of binary mixed DOPC:DOPS liposomes in water: The impact of charge condensation", *J. Chem. Phys.* Vol. 146, pp. 044701–044701, 2017.

CURRICULUM VITAE

Cornelis Lütgebaucks

Address	Chemin du Mont- Tendre 18, 1007 Lausanne
Mail	c.luetgebaucks@gmail.com
Date and place of birth	21.06.1985 in Hamm, Germany
Nationality	German
Marital status	Single

Education

2012 – 2017
PhD at École polytechnique fédérale de Lausanne (**EPFL**),
- Doctoral school for Bioengineering and Biotechnology
- Laboratory for fundamental Biophotonics

2009 – 2011
Master of Science at **TU Dresden**
- Faculty: Natural Science
- Specialization: Molecular Bioengineering

2005 – 2008
Bachelor of Science in **University of Applied Science Münster**
- Faculty: Physics and Engineering
- Specialization: Biomedical Engineering

2004
A-levels Gymnasium Hammonense in Hamm

Professional experience

2012 – 2017
EPFL (Assistant-Doctorant, 5 years in the laboratory for fundamental Biophotonics led by Prof. Sylvie Roke)

2011
Johns Hopkins University Baltimore, USA (Master thesis, 6 month in the laboratory of Prof. Sharon Gerecht)

2009 and 2010
Paul Scherer Institute (PSI), Villigen and **Institute Laue-Langevin (ILL), Grenoble** (research visit on neutron reflectometry, each 4-5 days)

2008 – 2009
CICBiomagune Donostia- San Sebastian, Spain (research position, 10 months in the laboratory of Dr. Ilya Reviakine)

2008
ETH Zürich, Switzerland (Bachelor thesis, 6 months in the laboratory of Prof. Janos Vörös)

Projects and key skills

PhD thesis
Title: Lipid membrane characterization with second harmonic scattering: surface potentials, ionization, membrane asymmetry and hydration
- Development of a novel table-top method using second harmonic scattering to extract the surface potential of membranes from solution without assuming an interfacial model

Master thesis
Title: Creation of dual functionalized surfaces for interrogating cancer and vascular cell interactions in-vitro

	- Development of a protocol to optimally create the functionalized surface
	- Analyze the cell growth and cell-cell interaction
	- Despite time issues and financial constraints, this task was successfully fulfilled and published
Research position at CICbiomagune	Quantitative analyses of the deformation of liposomes during immobilization on a titania surface
	- Analyzing various lipid compositions in vesicles as a function of their adsorption behavior on titania
	- Full time research scientist
	- Participation in neutron scattering experiments that require 24 hour observation
Bachelor thesis	Title: Research in polymeric nanogel labels for microarray applications
	- Development of a protocol to create stable self-assembled nanoparticles that can be used as fluorophore container

Technical skills

Optics	Femtosecond laser spectroscopy, second harmonic generation, confocal laser scanning microscopy, fluorescence microscopy
Biophysics	Quartz- crystal- microbalance with dissipation, atomic force microscopy, ellipsometry, dynamic light scattering, laser Doppler anemometry,
Microfabrication	Soft lithography, optical lithography, clean room experience (clean room class 1000)
Biology	Polymerase chain reaction, gel electrophoresis, thin layer chromatography
Tissue Culture	Mammalian cell culture, cell separation
IT	Basics in coding languages C and C++, Python,
Software	Mathematica, Matlab, Origin lab, IgorPro, autoCAD2000, SolidWorks, Adobe Illustrator, LabVIEW, MS office

Languages

English	Fluent (C2)
French	limited working proficiency (B1)
German	native speaker
Spanish	Basic understanding and limited talk ability (A1)
Other languages	Latin (Latin proficiency) and ancient Greek

Honours and Awards

Scholarships	Scholarship "Promos" 2011 of TU Dresden for studying abroad

Extracurricular activities

Interests	classical literature, music (playing violin and trumpet)
Volunteering	2015 – 2017 National treasurer of the LEO District Suisse
	2012 – 2014 Committee member of the hiring days at EPFL
	2006 – 2008: member of the board of a student orchestra
	1998 – 2004: member of school council, speaker of the school

Lausanne, January 2017